TUNABLE GEOMETRIC FANO RESONANCES IN A METAL/INSULATOR STACK

by

HERBERT GROTEWOHL

A DISSERTATION

Presented to the Department of Physics
and the Graduate School of the University of Oregon
in partial fulfillment of the requirements
for the degree of
Doctor of Philosophy

September 2016

DISSERTATION APPROVAL PAGE

Student: Herbert Grotewohl

Title: Tunable Geometric Fano Resonances in a Metal/Insulator Stack

This dissertation has been accepted and approved in partial fulfillment of the requirements for the Doctor of Philosophy degree in the Department of Physics by:

Ben McMorran	Chair
Miriam Deutsch	Advisor
Jens Noeckel	Core Member
Shannon Boettcher	Institutional Representative

and

Scott L. Pratt	Dean of the Graduate School

Original approval signatures are on file with the University of Oregon Graduate School.

Degree awarded September 2016

DISSERTATION ABSTRACT

Herbert Grotewohl

Doctor of Philosophy

Department of Physics

September 2016

Title: Tunable Geometric Fano Resonances in a Metal/Insulator Stack

We present a theoretical analysis of surface-plasmon-mediated mode-coupling in a planar thin film metal/insulator stack. The spatial overlap of a surface plasmon polariton (SPP) and a waveguide mode results in a Fano interference analog. Tuning of the material parameters effects the modes and output fields of the system. Lastly, the intensity and phase sensitivity of the system are compared to a standard surface plasmon resonance (SPR).

We begin with background information on Fano interference, an interference effect between two indistinguishable pathways. Originally described for autoionization, we discuss the analogs in other systems. We discuss the features of Fano interference in the mode diagrams, and the Fano resonance observed in the output field. The idea of a geometric Fano resonance (GFR) occurring in the angular domain is presented.

Background information on surface plasmon polaritons is covered next. The dielectric properties of metals and how they relate to surface plasmons is first reviewed. The theoretical background of SPPs on an infinite planar surface is covered.

The modes of a two planar interface metal/insulator stack are reviewed and the leaky properties of the waveguide are shown in the reflectance. We solve for modes of a three interface metal/insulator stack and shows an avoided crossing in the modes

indicative of Fano interference. We observe the asymmetric Fano resonance in the angular domain in the reflectance.

The tunability of the material parameters tunes the GFR of the system. The GFR tuning is explored and different Fano lineshapes are observed. We also observe a reversal of the asymmetry Fano lineshape, attributed to the relate phase interactions of the non-interacting modes. The phase of the GFR is calculated and discussed for the variations of the parameters.

The reflected field is explored as the insulator permittivities are varied. As the waveguide permittivity is varied, we show there is little response from the system. As the exterior permittivity is varied, the reflectance exhibits the geometric Fano resonance and the tunability of the lineshape is explored. Finally, we calculate the sensitivities of our metal/insulator stack to changes in the permittivity and compare them to the sensitivities of SPRs.

This dissertation includes previously published and unpublished co-authored material.

CURRICULUM VITAE

NAME OF AUTHOR: Herbert Grotewohl

GRADUATE AND UNDERGRADUATE SCHOOLS ATTENDED:

University of Oregon, Eugene, Oregon
Colorado State University, Fort Collins, Colorado

DEGREES AWARDED:

Doctor of Philosophy, Physics, 2016, University of Oregon
Bachelor of Science, Physics, 2009, Colorado State University

AREAS OF SPECIAL INTEREST:

Roller Derby- Skater, Official, Volunteer and Board Member.

PROFESSIONAL EXPERIENCE:

Graduate Teaching Assistant, Department of Physics, University of Oregon, Eugene, 2009-2011 and 2015-2016

Graduate Research Assistant, Department of Physics, University of Oregon, Eugene, 2011-2016

Science Literacy Teaching Fellow, University of Oregon, Eugene, 2014-2015

GRANTS, AWARDS AND HONORS:

Weiser award, 2011, awarded for teaching excellence.

PUBLICATIONS:

Grotewohl, H., and Deutsch, M. (2015). Tunable geometric Fano resonances in a metal/insulator stack. Journal of Optics, 17(8), 085003. http://doi.org/10.1088/2040-8978/17/8/085003

ACKNOWLEDGEMENTS

Thanks go to all the graduate students with whom I interacted at the University of Oregon for time spent relaxing and discussing both research and non research. With out that atmosphere, I would not have survived the early parts of graduate school.

On the same grounds, I would like to thank my teammates of the Lane County Concussion. The inclusion into such a great group of guys really lifted my spirits in many times of need. Though I am departing the team as I move away from Eugene, I will never forget the times I had with all y'all.

I would like to thank my fellow research group members Brian Hake, Shikhadeep Gill-DeFazio, Andrea Georning and Caleb Holt for reminding me that I know things, helping me when I didn't know things and general camaraderie with grad school. Even though we didn't always interact while crammed into our little office, every time we did it was a positive. I always wanted to talk more and only finally came to due so towards the end.

Special thanks go to Chris Newby, whom took the time to help with with editing this dissertation. One day, I will learn that not every sentence needs the word "will" in it, one day.

I'd like to thank Miriam, because no job should be a thankless job.

Lastly, I would like to thank everyone who gave me encouragement in the end. Especially Amber Cooper, who got me involved with roller derby, helped keep me sane with lunches and without her love and encouragement who knows where I would be at this moment.

TABLE OF CONTENTS

LIST OF FIGURES

LIST OF TABLES

CHAPTER I

INTRODUCTION

In this dissertation we discuss the interactions of light in and near visible wavelengths (340 nm $< \lambda <$ 1350 nm) with structured metal/insulator thin film systems. The variations of the thin film thicknesses explored are smaller than the free space wavelength of light. The subwavelength confinement and manipulation of light on the order of tens of nanometers is one of the current frontiers in optics. The confinement comes from electromagnetic (EM) waves bound at the surfaces between metals and insulators. These surface bound modes, called surface plasmon polaritons (SPP) have come to the fore front due it recent advancements in nano-scale fabrication, optical characterization techniques and computational advancements[1]. Within the thin film stacks explored, we observe interactions between the surface bound modes with each other. The idea of mode interference is universal and once the proper analogues are made, a large depth of knowledge from mode interactions can be brought to understandings of our particular system. A particular type of atomic interaction was first treated theoretically by Ugo Fano, and now the interference and resonance bear his name. We use the breadth of knowledge about mode interference from atomic systems, which have been explored for sometime, and apply that knowledge to our structured layered system.

Surface Plasmons

The study of EM radiation interacting with surfaces has been studied for just over a century. The experimental work on EM radiation and surfaces started mid 19th century by Faraday[2]. Early theoretical work occurred around the start of the

1

20th century by Sommerfeld[3], Zenneck[4] and Mie[5]. Nearly forty years later, Ugo Fano brought together the work of Wood and Sommerfield[6] by combining freely propagating EM radiation with radiating surface modes. While this is one part of Fano's body of work, this is not the focus of the work by Fano we discuss in this dissertation. We discuss more about Fano in a bit. Applications of EM interactions with surfaces have been prevalent throughout the past century, with quite possibly the most important being the invention of transistors. Recently in the 1990's, there was an explosion of the plasmon research pushed by industry. Three primary applications have been pushing the research: The need for sub wavelength confinement due to the miniaturization of circuits, metamaterial applications for index manipulation and plasmonic sensors in the life sciences.

For information technology, there has been a push to continually decrease the size of computational components. As industry attempts to keep up with Moore's "law"[1] research into miniaturization of components continues. A fundamental limit being approached was the diffraction limit of light, in which optical devices were not able to surpass. Fortunately, that limit is only for free-space propagation and it has been shown that SPPs allow for sub wavelength confinement[8]. There has already been work done to show that plasmonic systems can be used to create fundamental circuit elements such as mirrors, beam splitters, interferometers, ring resonators, modulators and switches[9–14].

Another area of research is plasmonic metamaterial engineering. Metamaterials are a class of materials designed to have certain EM responses to simulate a given permittivity. Metamaterials consist of patterned subwavelength elements that

---

[1]In 1965, Gordon Moore (co-founder of IBM) noted that the component density of integrated circuits was doubling every year[7]. As this trend as continued, it has become to be referred to as a law.

interact with the EM radiation. The subwavelength elements allows for consideration of the metamaterial as an effective permittivity and permeability, akin to atomic patterning and lattices. The metamaterials can be designed to create permittivity and permeability properties that are not observed in nature. One such metameterial type is negative index materials (NIM), also known as left handed materials[15]. For these materials the permittivity, permeability and index of refraction are negative. NIM metamaterials have already been experimentally created in several different ranges of frequencies[16–18].

As the field of the SPP is confined to subwavelength dimensions, this creates a large field enhancement at the surface. This makes the system very sensitive to changes in the local environment at the interface. This has lead to the usage of the surface plasmon resonance (SPR) for optical sensing. Initially, SPR was used on a planar metal film under attenuated total reflection (ATR)[19]. The metallic surface can be functionalized to allow for binding of specific chemical or biological agents to the surface[20, 21]. The binding of the agents to the surface changes the local permittivity and alters the dispersion of the SPP. This results in a shift of the SPR, and this can be detected as either a shift of the resonance location or an intensity shift. For most biological systems, gold is used due to its lack of toxicity. When toxicity is not an issue, silver is used due to fewer losses in the metal and therefor a narrowed resonance. Early sensors were shown to have sensitivities on the order of 10^{-6} refractive index units[22]. Prism based SPR sensors are currently commercially available from many companies such as Biacore. Sensitivities have been pushed to lower values over the years and a move to phase based sensors has put the sensitivity on the order of 10^{-8}[23]. SPR has been used for a variety of sensing applications, such as detection of gas concentrations[24, 25], liquid identification[26],

temperature sensing[27], and biological and chemical sensors[25, 28, 29]. This is the focus of this dissertation, pushing the limits of the surface plasmon based sensors in a metal/insulator thin film stack.

Another area of interest in plasmonics is localized surface plasmons (LSP). Here the plasmonic excitation occurs in tunable nanoparticles. The shape and patterning of the particles can be tuned to different resonant frequencies. There is a large field enhancement near the particles and between the particles in these nano-particle systems. As with SPP systems, this makes the LSP system highly sensitive to changes in the local permittivity. This allows localized surface plasmons to also be used for sensing applications. Disordered plasmonic nanoparticles are one such system that has been used for biological detection[30–33]. Additionally, ordered plamonic nanoparticle arrays[34] and gold nano shells[35] have been used to increase the sensitivity of surface enhanced Raman spectroscopy.

Here, we have only begun to scratch the surface of the applications of surface plamons. A complete list of them all goes far beyond the scope of this dissertation, but it is worth while to note a few other areas of research. Just to name a few: cancer imaging and therapy[36, 37], targeted drug delivery[38], field enhancement in solar cells[39], photolithography below the diffraction limit[40], photon entanglement survivability[41] and surface plasmon amplification by stimulated emission of radiation (SPASER)[42]. Several of these examples come from optical analogues, such as the SPASER. We continue this trend and use more work done by Fano to understand the properties of our thin film system.

Fano Interference

Ugo Fano was born in Turin, Italy on July 28, 1912. Throughout his six decade career working in atomic and molecular, radiation physics and other areas, he published 5 books, wrote over 250 papers and had $\sim$30 PhD students[43]. He worked under Enrico Fermi and Werner Heisenberg for his post-doctorial work before moving to America in 1939. There he worked for several institutions, including the National Bureau of Standards (National Institute of Standards and Technology), before settling at the University of Chicago in 1966. He passed on February 13, 2001, leaving a large mark in physics. We focus on his work done on the interference between a discrete state and a continuum state in helium atoms, known as Fano interference (FI)[44]. This is not to be confused with other effects that bear his name such as Fano factor[45], Fano effect[46], and the Fano-Lichten mechanism[47].

In his 1961 paper on the interference in helium spectrum, Fano laid out the theory for interference between a discrete state and a broad continuum in autoionized states. In his work, the discrete state is "*modified by an admixture* of states of the continuum"[2] in which the interference of the two excitation pathways must be considered. Previous work failed to include the interactions between the discrete state and the continuum states. This theoretical work explained the previously mysterious asymmetric lineshape of the He spectrum, and the resulting phenomenon now bears his name. Fig. 1 shows the original Fano resonance (FR) plot, as well as the fits he made to experimental autoionized states in He.

---

[2][44] Emphasise by Fano
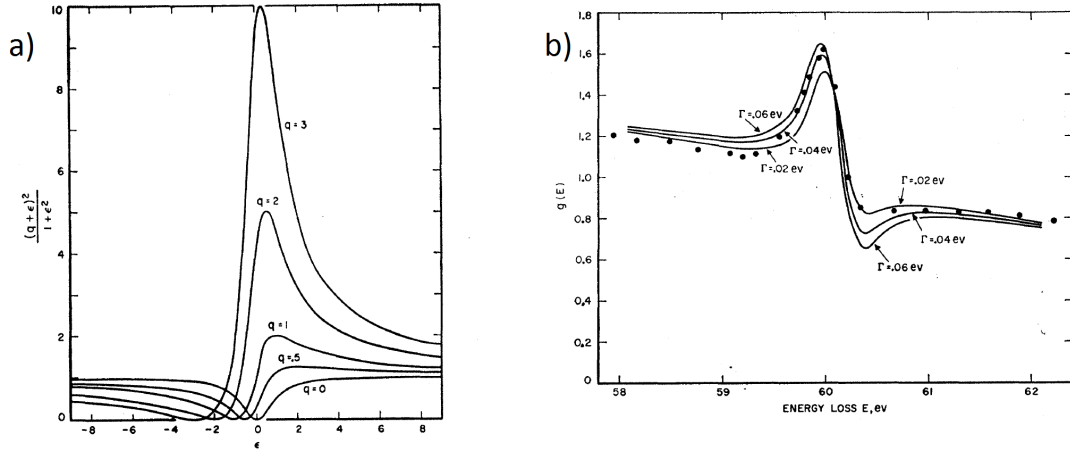
FIGURE 1. Fano resonance and fit to Helium

From reference [44]. **a)** Fano resonances with various degrees of asymmetry. The x-axes is the energy parameter detuned from resonance, while the y-axes is the Fano formula. **b)** Comparison of theory and experiment for Helium. The experimental output power vs the energy is shown as the data points, while the lines are the theoretical fits with different asymmetry parameters.

The mathematical base of the FI has found its way into other realms of physics. As such, the lineshape has been observed in many different systems[3] due to the analogs that can be found from atomic probabilities to wave equations. One well known case of FI is electromagnetically induced transparency (EIT)[48–52]. In the autoionized states, both quantum pathways are excited simultaneously and the spectral line shape exhibits FRs. In EIT the two indistinguishable pathways that interfere are the direct excitation to the upper state and a three step process. For EIT, two separate input beams are used to excite the two different atomic energy levels. The probe beam, in absence of the pump beam, exhibits a standard absorption resonance. When the pump beam is used to excite the secondary energy level to the same upper state, destructive interference between the two different excitation pathways occurs, making the atomic medium transparent at the resonant frequency, shown in Fig. 2. The pump beam

---

[3]A search on Web of Science of "Fano interference" returns over 1000 results at the time of this dissertation.

6
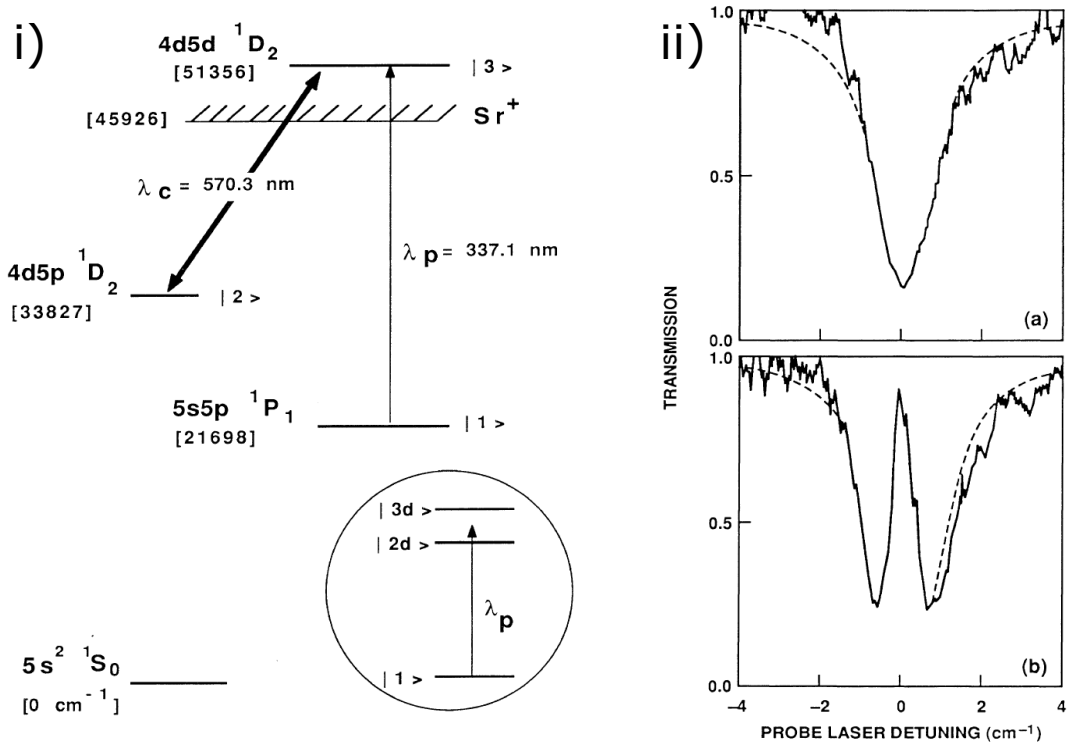
FIGURE 2. Electromagnetically induced transparency
From reference [48]. **i)** Energy level diagram for neutral Sr. The probe beam is varied across the frequencies in the region of the $|1\rangle$ to $|3\rangle$ transition, while the pump beam is set to the frequency of the $|2>$ to $|3>$ transition. The two excitation pathways responsible for EIT are from $|1\rangle$ to $|3\rangle$ and from $|1\rangle$ to $|3\rangle$ to $|2\rangle$ to $|3\rangle$. **ii)** Top (a) Frequency resonance sweep without pump beam. Bottom (b) Frequency resonance sweep with pump beam exhibiting EIT.

increases the amplitude of the three step process, allowing for the strong interference effect to be observed. This allows for an on/off switch of the EIT, which is not possible for FI in autoionized states.

Another example of atomic FI is lasers without inversion[53, 54]. In this case, FI is used to break the symmetry of the excitation and decay probabilities[55]. Another FI effect is seen in the electronic energy levels of quantum dots[56, 57]. As quantum probability amplitudes and classical waves are described the same mathematically, analogies can be observed in the interactions of optical modes; such as a cavity mode

coupled with a waveguide mode in an optical system[58]. Fano interference is observed in many different optical systems[59–66], as well as plasmonic systems[67–73], where classical wave analogs of EIT have also been observed[59, 60, 74–79]. Additionally, classical wave interference is the same as to the interactions of coupled oscillators. This has allowed for observation of FI and EIT-like transparencies in classical coupled oscillators and RC circuits[80–84]. FI analogs can be found in nuclei[85], hadronic systems[86], fluid flow[87] and other wave systems. This is by no means a complete list, but shows the breadth of applications of Fano interference.

Outline of this Dissertation

In this dissertation a metal/insulator thin film stack is explored. The multiple metal/insulator interfaces allow for surface plasmon modes and metallic waveguide modes in the system. We look at the interactions between a waveguide mode and a surface plasmon mode. We show that the interference between these modes is in fact an analog of FI. The tunability of the system is explored by varying the thicknesses of the films as well as the permittivities. The tunability is then used to maximize the sensitivity of the system for several different Fano lineshapes.

In chapter 2, Fano interference and the Fano resonance are reviewed in a quick tutorial. The Fano interference is discussed, and how its analogs are able to relate to it. The FR is shown and variations of the Fano lineshape are discussed, including the reversal of the asymmetry of the resonance. We lastly introduce and discuss the idea of a geometric Fano resonance (GFR), which occurs in the angular domain.

In chapter 3, a review of surface plasmons is done. It starts with a discussion of metal properities and how they relate to the excitation of the surface plasmons. We then discuss surface plasmon polaritons at a planar interface. It is discussed how to

input energy into the SPP and the common Kretschmann configuration is employed to show the surface plasmon resonance. The chapter is wrapped up by discussing the SPP as a geometric Fano system.

In chapter 4, we introduce more layers to the system, allowing for coupling between different interfaces. First discussed is a three layer system consisting of a insulator film sandwiched between two semi-infinite metals. Next a four layer system is discussed consisting of an insulator film and a metallic film with an asymmetric cladding. The asymmetric cladding is a semi-infinite thickness insulator abutting the metal film and a semi-infinite thickness metal abutting the insulator film. In this system we analyse the waveguide mode and the SPP mode as the continuum and discrete modes of the FI (respectively). Using the same momentum matching scheme as the Kretschmann configuration for SPR, the GFR of a five layer system is shown. The chapter is capped off by showing that a FR does not exist in the frequency domain for this system.

In chapters 5 and 6, the parameters of the five layer system are explored. In chapter 5, the emphasise is on the reflected intensity of the system, while chapter 6 focuses on the phase behavior. The thicknesses of each of the finite films are explored: a metal film that spatially separates the modes, the insulator film that houses the waveguide mode and a metal film that allows for input light into the system. The metal films are unchanged from silver, but variations to all three insulator layer are explored.

In chapter 7, the parameters of the system are optimized for maximal sensitivity. We start be defining our sensitivity, both intensity and phase based. We then compare several parameter sets of our metal/insulator stack with SPR.

CHAPTER II

FANO INTERFERENCE

Consider the interference of two separate, indistinguishable excitation pathways to a continuum state, where these two paths are directly and indirectly excited through a discrete state. This is the system in which Ugo Fano was able to work out the theory for the interference observed in autoionization of He[44] which the phenomenon now bears his name: Fano interference (FI). Direct excitation to the ionized continuum states is indistinguishable from the excitation to the ionized state with an intermediate step in a discrete atomic state, as shown in Fig. 3 (a) and (b). The interference between the modes creates an asymmetric resonance, which comes from the changing phase profile of the discrete state compared to the relatively unchanged phase of the continuum state. For working out the theory of the asymmetric resonance, In a special case of FI, in which the two states share the same resonant frequency, is electromagnetically induced transparency (EIT). In EIT the two indistinguishable pathways that interfere are the direct excitation to the upper state and a three step process, as shown in Fig. 3 (c) and (d). In this case, the upper state is not continuum state, but instead a broad state with a large mode width. It is useful to examine FI by examining the energy level diagram of the system. With different noninteracting pathways, the different modes of the system cross at given energies. This is shown in Fig. 4 (b) and (d) as the dashed lines. When the modes interact in atomic systems the dressed state formalism can be used to show an avoided crossing in the energy level diagrams, given by the solid lines in Fig. 4(b). We also examine another system, coupled classical oscillators as shown in Fig. 4(c), and we look at the energy diagrams for the oscillators in Fig. 4(d), we see the same avoided
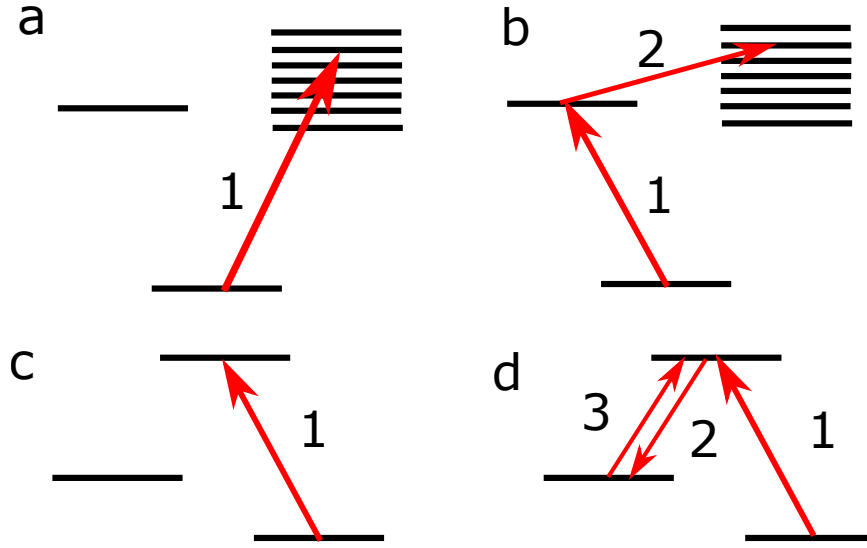
FIGURE 3. Energy level diagrams for two indistinguishable excitation pathways Excitation pathways for autoionization (a and b) and electromagnetically induced transparency (c and d). **a)** Direct excitation to the continuum. **b)** Excitation to continuum via the discrete state. **c)** Normal excitation to the upper state. **d)** A second excitation pathway to the upper state. The first step is directly to the upper state. The next path is a de-excitation to a different lower state. A final re-excitation to the upper state completes the indistinguishable pathway.

crossing as observed for the atomic system. Recognition of these avoided crossing as a sign for FI in systems.

The shape of the resonance is unique and a good understanding of the Fano line shape allows for recognition of the effect in other systems. For a diverse set of systems, the general form for a Fano resonance (FR) has become[69] [1]

$$I = \frac{(F\gamma + \omega - \omega_0)^2}{\gamma^2 + (\omega - \omega_0)^2} \tag{2.1}$$

---

[1]The original equation set about by Fano was given as[44]

$$I = \frac{(q + \epsilon)^2}{1 + \epsilon^2}$$

where ϵ is the energy parameter and q is a constant. This equation has historical significance and is the origin of the term q-reversal, discussed later in this chapter.
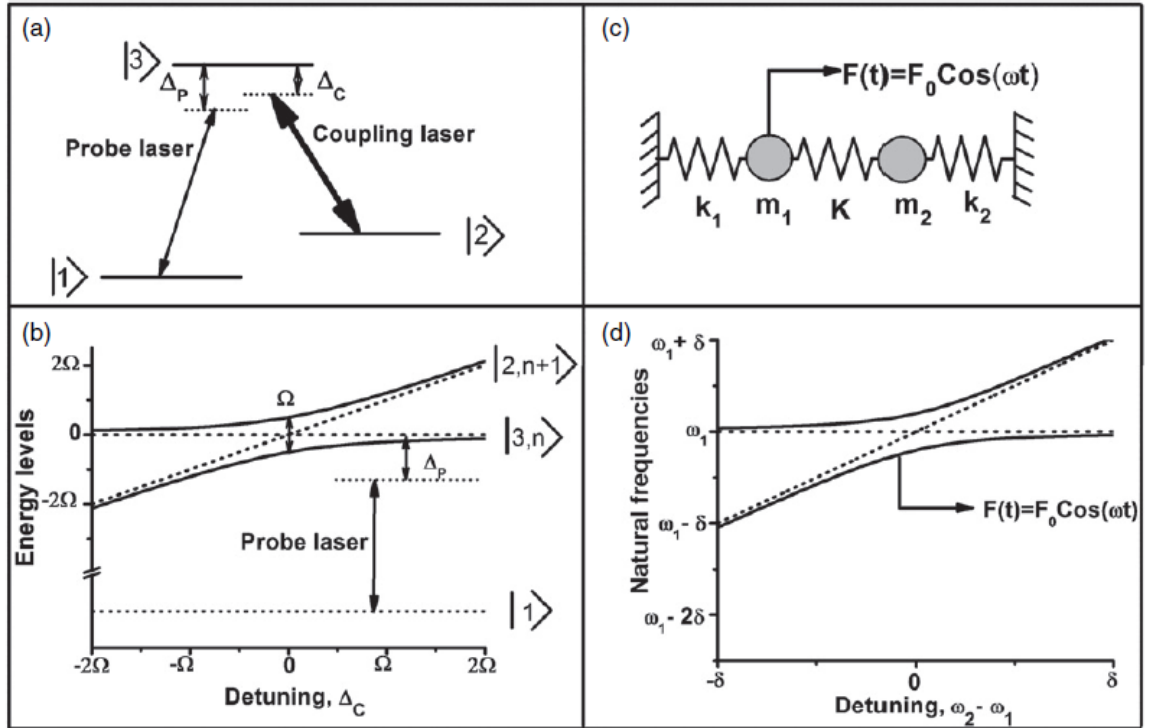
FIGURE 4. Atomic and classical Fano systems

From reference [84]. **a)** Level scheme for a lambda EIT atomic system. **b)** Dotted lines are the bare atomic states and the solid lines are the dressed states of the system. The split of the energy levels is given by the Rabi Frequency, Ω. **c)** Coupled oscillator system having a classical analog to EIT. The two masses are coupled by a spring and have a driving force on one mass. **d)** Frequency diagram of the oscillator system. Uncoupled oscillator modes are shown are dashed lines, and coupled system shown by solid lines. As in (b), the mode diagram shows an avoided crossing of the modes.

where γ is the line width parameter, ω_0 is the resonant frequency and F is the Fano parameter. The Fano parameter determines the asymmetry of the resonance, as shown in Fig. 5(a). When F is zero, the resonance is a Lorentz Resonance, but as F increases, a peak begins to emerge as the minimum intensity shifts away from the resonant frequency. There is a balance at $F=1$ when the minimum and maximum are of equal magnitude. The addition of the line width parameter allows for the broadening/narrowing of the resonance, as shown in Fig. 5(b). For small γ, the
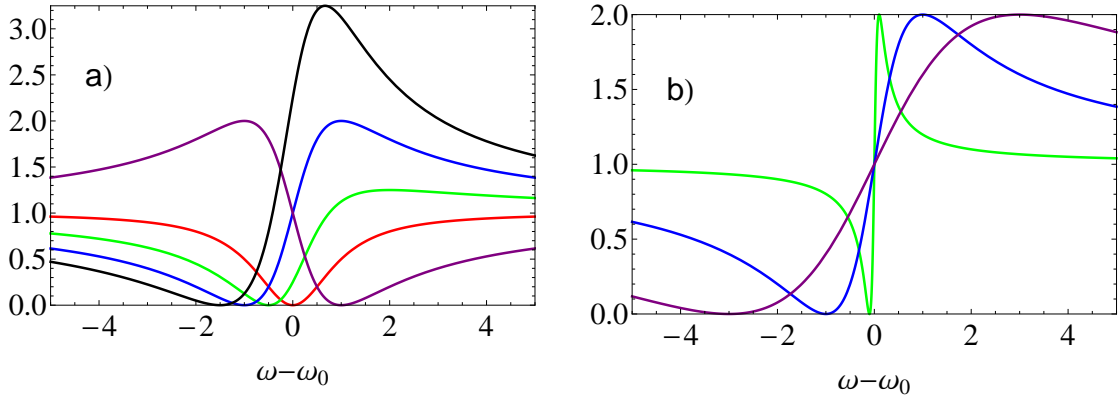
FIGURE 5. Fano resonance plots

a) The Fano resonance (Eq. (2.1)) with $\gamma = 1$ and F is 0 (red), 0.5 (green), 1 (blue), 1.5 (black) and -1 (purple). The switched sign of the Fano parameter mirrors the plot about the resonant frequency. **b)** The Fano resonance (Eq. (2.1)) with $F = 1$ and γ is 0.1 (green), 1 (blue), and 3 (purple).

resonance is quite narrow and as γ increases, the resonance widens while maintaining the same intensity.

If the sign of the Fano parameter is negative, the lineshape is mirrored about the resonant frequency. When this occurs, it is referred to as q-reversal, referencing Fano's form of the equation and was originally observed in autoionized atomic systems[88–90]. It was found that the discrete narrow resonances were different in the degree and direction of the asymmetry depending on the spectral location of the mode. Fano interference is highly sensitive to the relative phase of the two modes. As the phase profiles are swept through each other, the regions of constructive and destructive interference switch, causing the q-reversal. For many systems exhibiting FI, the noninteracting modes can be shifted by changing the physical parameters of the system. The common result is a change in the relative resonance locations of the noninteracting modes. From this it is shown that the independent resonance locations determine the asymmetry[58, 61, 66, 72].

The discussion thus far has been focused on FRs in the frequency domain. Alternatively, there can be the manipulation of geometric modes in space. As discussed in the following chapter on surface plasmons, SPRs are a manifestation of FI in the angular domain[91]. Additional geometric systems, such as guided wave structures[72, 92] and plasmonic systems[77], which is a new interpretation that we have termed a Geometric Fano Resonance (GFR). The idea of quantum interference in space using geometrical parameters enables control of mode coupling in guided-wave structures in manners analogous to FI. The control of quantum interference of geometrical resonances allows for the extension of known quantum coherence theory to the spatial domain.

In previous work done by our group, an EIT plasmonic analogy was observed in metal/insulator microspheres[77]. In that work, we observed the two main signatures of FI: an avoided crossing in the mode dispersion (Fig. 6(a)) and a large change to the output signal (Fig. 6(b)). The continued extension beyond energies and frequencies is a focus of this dissertation.

In the next chapter we discuss surface plasmons, with a focus on surface plasmon resonance. Surface plasmon resonances are the discrete state for the GFR in our system. It is important to discuss the nature of the surface plasmon resonance to understand the how changes to the non-interacting surface plasmon resonance affect the GFR.
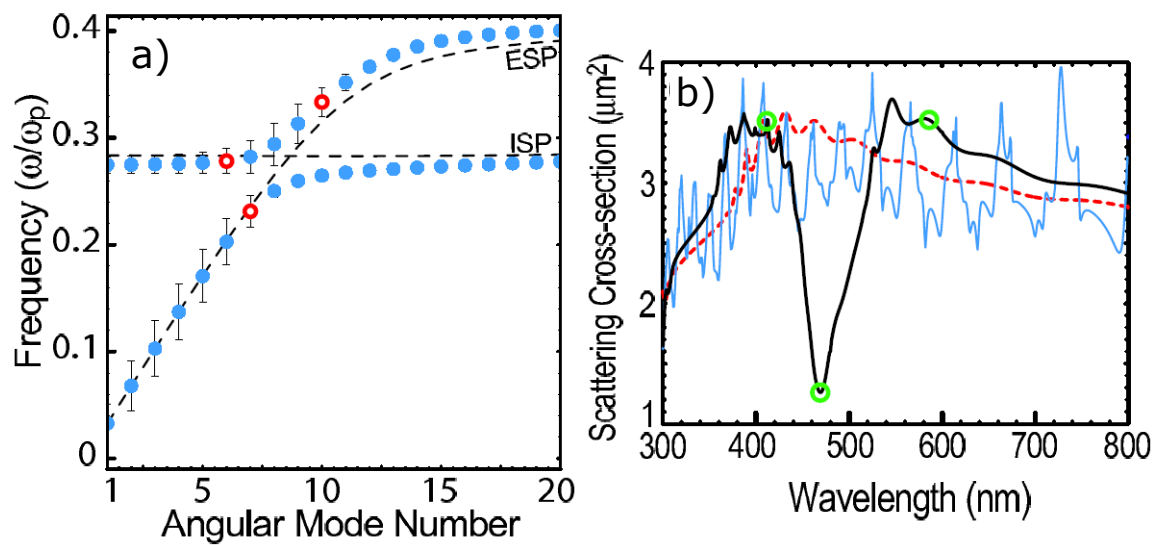
FIGURE 6. Plasmon assisted transparency

Figures from [77]. **a)** Angular mode dispersion of a metal microsphere surrounded by two shells, the inner of which is an insulator and the outer being a metal shell. Referred to as a MIM microsphere. In this case the avoided crossing is seen in the angular modes, not an energy or frequency detuning. **b)** Scattering cross section for a silver microsphere (red dashed), a silver shell (blue) and a MIM microsphere (black). The combined system exhibits a transparency expected from the mode diagram.

CHAPTER III

SURFACE PLASMON POLARITONS

In this chapter we provide a review of surface plasmons (SPs). SPs are oscillations of free electrons coupled to an EM field at a metal/insulator interface. The electromagnetic field peaks at the interface and then decays exponentially as you move away from the interface. Surface plasmons can be excited in many systems, and the excitation depends on the geometry of the system, leading to both propagating and localized SPs. The SP enhances the EM field at the interface, and this field enhancement has applications in solar cells[93], fiber optics[94], photochemical processes[95], immunosensors[96], cancer treatment[97], and other biological systems[25, 28, 29].

For light interacting with a SP system under a suitable coupling scheme, a dip in output intensity is observed with the excitation of the SP. This is known as surface plasmon resonance (SPR) and is strongly affected by changes to the system, such as variations of the permittivity, film thicknesses and other variations. As discussed in the introduction, this has led to many applications of SPR.

We look at the specific geometrical arrangement of planar films which support surface plasmon polaritons (SPPs). The SPP is a coupling of an electron charge density to the EM field that is propagating along a metal surface. We can see in Fig. 7 the magnetic and electric field for a planar surface. The electric field lines point from regions of low to high electron density. The regions of high and low concentration alternate as the SPP propagates along the surface. SPPs typically have wavelengths of the order 100s of nm, which is close to the wavelength of the freely propagating light that excites the charged density wave. For noble metals, such as Ag and Au,
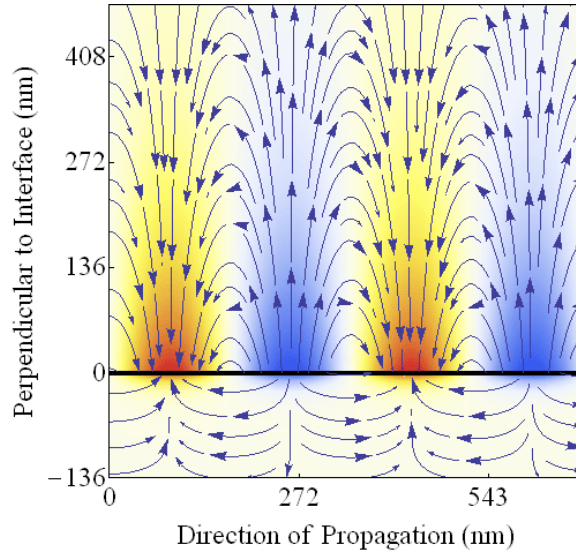
FIGURE 7. SPP field plots

The EM fields of a planar SPP. The magnetic field is transverse to the propagation and is shown as the red/blue density plot. The electric field occurs in the plane of propagation and is shown as the field lines. The interface occurs at zero in the perpendicular region with the metal and dielectric be in the negative and positive directions, respectively. The wavelength of light used is 357nm.

the excited frequencies are in the visible and infrared spectrum, and for metals and dielectrics the decar lengths of the EM field into the medium is of the order 10 to 100s of nm. The propagation distance of the wave along the surface is of the order μm.

In this chapter we present the basics of SPPs as they relate to our multilayer systems. We first discuss the dielectric function of metals, as understanding the dielectric function allows for a better understanding of why metals are required for surface plasmons. Second, we discuss the conditions for a SPP to exist for a planar interface. Following that we explore the excitations of the SPPs using the prism coupling method. Lastly, we discuss the SPP excitation as a GFR.

17

Dielectric Properties of Metals

To describe surface plasmons accurately, an analytic description of the metal permittivity, $\epsilon_m(\omega)$, is required as it varies with the frequency which has a large effect on the SPPs. For our formalism we use the Drude-Sommerfeld model (DSM) to describe the dielectric response function of the metals[98]. This model treats the metal as a non-interacting free electron gas with a background lattice and a loss term Γ; giving a permittivity of the form

$$\epsilon_m(\omega) = \epsilon_b - \frac{\omega_p^2}{\omega(\omega + i\Gamma)} \tag{3.1}$$

where ϵ_b is the high frequency limit and ω_p is the plasma frequency, the minimum frequency at which electromagnetic waves can propagate in bulk metals[1] and is given by [98]

$$\omega_p \equiv \sqrt{\frac{ne^2}{\epsilon_0 m^*}} \tag{3.2}$$

where n is the free electron density, e is the electron charge, ϵ_0 is the vacuum permittivity and m^* is the effective electron mass. The plasma frequency is Typical scale for ω_p are in the ultraviolet for noble metals. Later in this chapter, we use the the no loss approximation ($\Gamma = 0$) in Eq. (3.1) in order to have a purely real dielectric function. This approximation,

$$\epsilon_m = \epsilon_b - \frac{\omega_p^2}{\omega^2}, \tag{3.3}$$

is quite useful when determining resonant behavior.

Throughout this dissertation, we use silver as our metal due to its optical properties in the visible region of the EM spectrum: low losses and suitable permittivity to support SPPs, as discussed later. The DSM parameters for a silver-
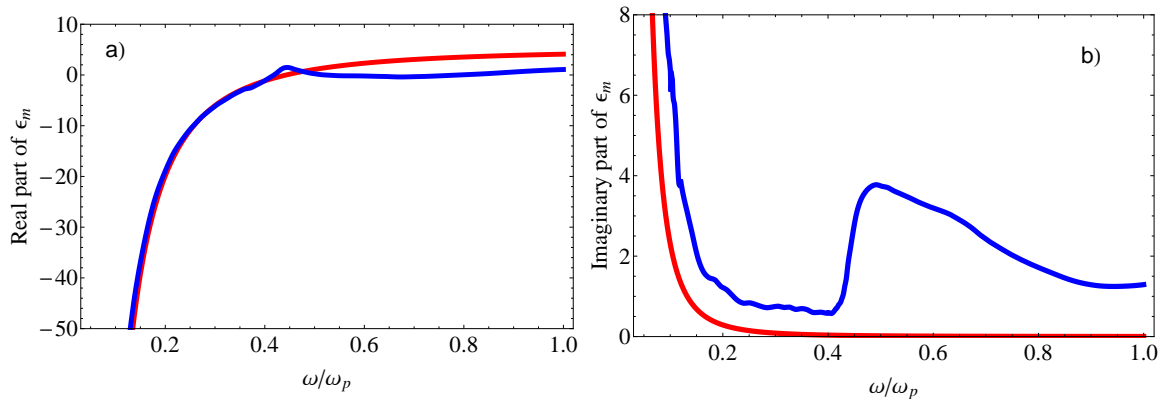
FIGURE 8. Silver permittivity
Real (a) and Imaginary (b) parts of the permittivity for silver using the Drude-Sommerfeld model (red) and tabulated data from Palik[99] (blue).

like metal[100] are $\hbar\omega_p = 9.1$ eV, $\hbar\Gamma = 0.021$ eV, and $\epsilon_b = 5.1$. Fig. 8 shows a comparison of the DSM and experimental data for silver tabulated by Palik[99]. In the region below $\omega/\omega_p < 0.4$, the DSM well describes the real part in comparison to the experimental data while fitting the general imaginary permittivity line-shape of the experimental data only shifted down meaning the DSM has lower overall loses for silver compared to experimental data. In the region $\omega/\omega_p > 0.4$, a large deviation occurs due to inter-band transitions in the silver[1]. More recently, the permittivity of epitaxial growth silver exhibiting lowered losses has been reported[101], and the DSM is a better approximation for such systems, but it still underestimates the losses. The lower losses of the model have an effect of narrowing both modes and resonances when using the DSM in comparison to what is experimental measured.

Lastly, losses begin to increase dramatically below $\omega/\omega_p \sim 0.1$ From these considerations, we only consider frequencies in the range of $0.1 < \omega/\omega_p < 0.4$ which corresponds to a wavelength range of 340nm $< \lambda <$ 1350nm. As we will see in the nest section, this range of frequencies covers the supported range for the SPPs.
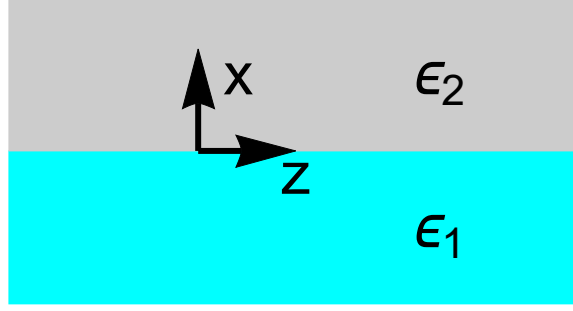
FIGURE 9. SPP system

Schematic diagram of two layer system, with coordinates used for Eqs. (3.4) and (3.5).

Surface Plasmon Polaritons at a Planar Interface

As mentioned previously, the SP is dependant upon the system setup and materials. There are two main categories of material geometries that support plasmonic excitations: nanoparticles/structures and planar systems. Nanoparticles exhibit different localized surface plasmons (LSP) depending on the shape, size and spacing of the particles[102, 103]. The focus of this dissertation is on infinite planar systems.

In this section we discuss the SPP at a single planar interface, and move to more interfaces in later chapters. The system consists of two layers infinite in y and z and each layer is semi-infinite in x with the interface at the $x = 0$ $y - z$ plane, as shown in Fig. 9. We assume a transverse magnetic (TM) solution that propagates along the interface in the z direction and decays in the direction perpendicular to the interface (x-direction). The electric field is in the $x - z$ directions and have translational invariance in the y direction:

$$\boldsymbol{E} = \begin{cases} (\hat{\boldsymbol{x}}E_{2x} + \hat{\boldsymbol{z}}E_{2z}) \cdot e^{ik_\parallel z - k_2 x - i\omega t} & x > 0 \\ (\hat{\boldsymbol{x}}E_{1x} + \hat{\boldsymbol{z}}E_{1z}) \cdot e^{ik_\parallel z + k_1 x - i\omega t} & x < 0 \end{cases} \qquad (3.4)$$

20

where subscripts 1 and 2 refer to the two layers, $E_{x,z}$ are the electric field components in the x and z direction, ω is the frequency of the propagating wave, $k_{\parallel}$ is the wave vector along the direction of propagation, and $k_{1,2}$ are the decay terms into each respective layer; $k_{1,2}$ are assumed to be positive, the sign in exponential determines the decay. The corresponding magnetic field is a TM solution solely in the y-direction,

$$\boldsymbol{H} = \begin{cases} (\hat{\boldsymbol{y}} H_1) \cdot e^{ik_{\parallel}z - k_1 x - i\omega t} & x > 0 \\ (\hat{\boldsymbol{y}} H_2) \cdot e^{ik_{\parallel}z + k_2 x - i\omega t} & x < 0 \end{cases} \tag{3.5}$$

We can relate the electric and magnetic fields using Maxwell's equations in the absence of a source term, specifically

$$\boldsymbol{\nabla} \times \boldsymbol{H} = \frac{\epsilon}{c}\frac{\partial}{\partial t}\boldsymbol{E} \tag{3.6}$$

where ϵ is the permittivity and c is the speed of light. Inputting Eqs. (3.4) and (3.5) into Eq. (3.6) and looking at the z component results in the relation:

$$\begin{aligned} H_1 &= +\frac{\epsilon_1}{k_1} i\frac{\omega}{c} E_{1z} \\ H_2 &= -\frac{\epsilon_2}{k_2} i\frac{\omega}{c} E_{2z} \end{aligned} \tag{3.7}$$

We can also find a relation involving E_x if we use the x component instead. This relation is

$$\begin{aligned} H_1 &= \frac{\epsilon_1}{k_{\parallel}} \frac{\omega}{c} E_{1x} \\ H_2 &= \frac{\epsilon_2}{k_{\parallel}} \frac{\omega}{c} E_{2x} \end{aligned} \tag{3.8}$$

21

equating $H_{1,2}$ in Eq. (3.7) to the right hand side of Eq. (3.8), we get

$$
\begin{aligned}
E_{1x} &= +\frac{k_\parallel}{k_1} i E_{1z} \\
E_{2x} &= -\frac{k_\parallel}{k_2} i E_{2z}
\end{aligned}
\tag{3.9}
$$

We now apply the boundary conditions:

$$
E_{1\parallel} = E_{2\parallel}
\tag{3.10}
$$

$$
H_{1\parallel} = H_{2\parallel}
\tag{3.11}
$$

Using Eq. (3.7) for H in Eq. (3.11) we get

$$
\begin{aligned}
E_{1z} &= E_{2z} \\
\frac{\epsilon_1}{k_1} E_{1z} &= -\frac{\epsilon_2}{k_2} E_{2z}
\end{aligned}
\tag{3.12}
$$

so following must be true for a solution to exist

$$
\frac{\epsilon_1}{k_1} = -\frac{\epsilon_2}{k_2}
\tag{3.13}
$$

As $k_{1,2}$ were assumed to be positive, this tells us that ϵ of one of the materials must be negative, otherwise Eq. (3.13) does not hold. We use a silver-like Drude metal for the negative permittivity. The decay length into each medium is be proportional to the inverse of the decay terms ($k_{1,2}$). This tells us that the relative decay length in each layer is be related to the ratio of the magnitudes of the permittivities.

Now for the dispersion relation we apply the wave equation

$$
\left(\boldsymbol{\nabla}^2 - \frac{\mu\epsilon}{c^2} \frac{\partial^2}{\partial t} \right) \boldsymbol{E} = 0
\tag{3.14}
$$

where μ is the permeability, to get

$$k_i^2 = k_\parallel^2 - \epsilon_i \left(\frac{\omega}{c}\right)^2 \tag{3.15}$$

where i refers to medium 1 or 2. We combine Eq. (3.13) and Eq. (3.15) and solving for $k_\parallel$ we get the SPP mode dispersion relation

$$k_{sp} \equiv k_\parallel = \frac{\omega}{c}\sqrt{\frac{\epsilon_1 \epsilon_2}{\epsilon_1 + \epsilon_2}} \tag{3.16}$$

As the metal permittivity is frequency dependent, there is a given frequency in which the denominator in Eq.(3.16) is zero, assuming purely real permittivities. The frequency at which this occurs is defined as the surface plasmon frequency. A lossless Drude metal (permittivity given by Eq. (3.3)) is used for one of the permittivities and then solving for the SP frequency gives

$$\omega_{sp} = \frac{\omega_p}{\sqrt{\epsilon_b + \epsilon_2}} \tag{3.17}$$

The surface plasmon frequency (ω_{sp}) is be smaller than the plasma frequency of the metal and depends on which metal is being used and the dielectric abutting the metal. For our Drude parameters for the metal layer and vacuum for the other dielectric, $\omega_{sp} = \omega_p/\sqrt{6.1} = 0.405\omega_p$. This is at the upper edge of the region in which the Drude model adequately describes the metal. Increasing the dielectric permittivity pushes the SP frequency to lower values, but still within our region in which the Drude model holds ($0.1 < \omega/\omega_p < 0.4$).

Similar formalism can be used assuming the full Drude model. The solution is slightly modified by the loss term (Γ) in the model, and k will become complex.
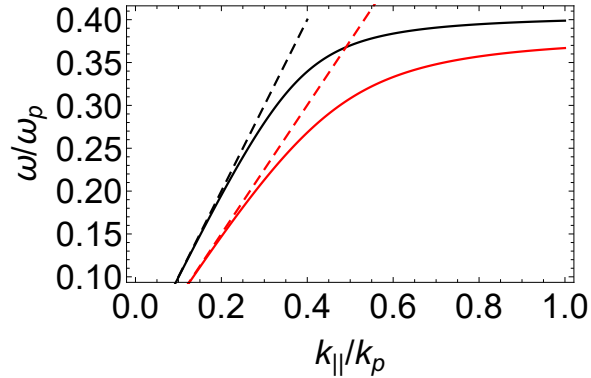
FIGURE 10. SPP mode diagram
SPP mode diagrams for silver/vacuum layers (black) and silver/water layers (red). Included as dashed lines are the light lines in vacuum (black) and water (red). Real part of $k_\parallel$ is used to plot. $k_p = \omega_p/c$.

It is important to note that for complex permittivities, the eigenvalue solutions for the modes are also complex which causes the modes to have a width proportional to the imaginary component of the eigenvalue solution. This solution for the plasmon frequency is only valid for this planar system, and needs to be reformulated for other geometric systems as the boundary conditions are different.

In Fig. 10 we plot the mode diagram for the SPP mode, Eq. (3.16), for lossless silver-like Drude metal with two different dielectrics, vacuum and water. At lower frequencies, the mode approaches the light line, and as the frequency increases the mode asymptotically approaches the ω_{sp}. The mode for water approaches a lower frequency as indicated by Eq. (3.17) due to the increased permittivity of water. It is important to note that the SPP modes have a higher wave vector, and therefore more momentum, than the light line for each dielectric. This indicates that light can not be coupled directly to the SPP mode from the dielectric as there is a momentum mismatch. We address this issue in the next section
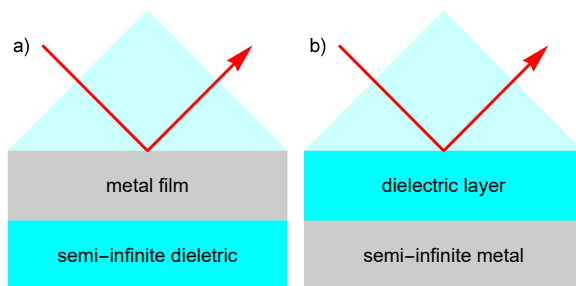
FIGURE 11. Attenuated total internal reflection configurations
a) Kretschmann-Raether configuration **b)** Otto configuration.

Coupling light into the SPP mode

As mentioned above, there is a momentum mismatch which needs to be overcome in order to excite the SPP mode. There are two main mechanisms for achieving this: attenuated total internal reflection (ATR) and grating coupling. In this work we focus on ATR coupling in detail below. Grating coupling causes the incoming photons to be scattered by a periodic structure parallel to the surface in integer values of the crystal lattice momentum and is covered in detail in standard plasmonic books[1, 104]. Lesser used excitations schemes exist such as four wave mixing[105] and other nonlinear methods[1, 104, 106].

There are two configurations for ATR: Otto and Kretchsmann-Raether[107]. They can be seen in Fig. 11. Both configurations work under the principle that input light comes from a higher index, and thus have the required additional momentum. To be able to achieve this, the coupling medium must be in the shape of a prism, typically a semi-cylindrical or a right angle one. When light in air strikes a dielectric interface, it gains momentum relative to the permittivity of the dielectric. The light, now inside the prism, hits the two layer system at an angle above the critical angle. Due to the nature of total internal reflection, evanescent waves are excited at the prism edge, and these evanescent waves excite the SPP at the interface. The angle
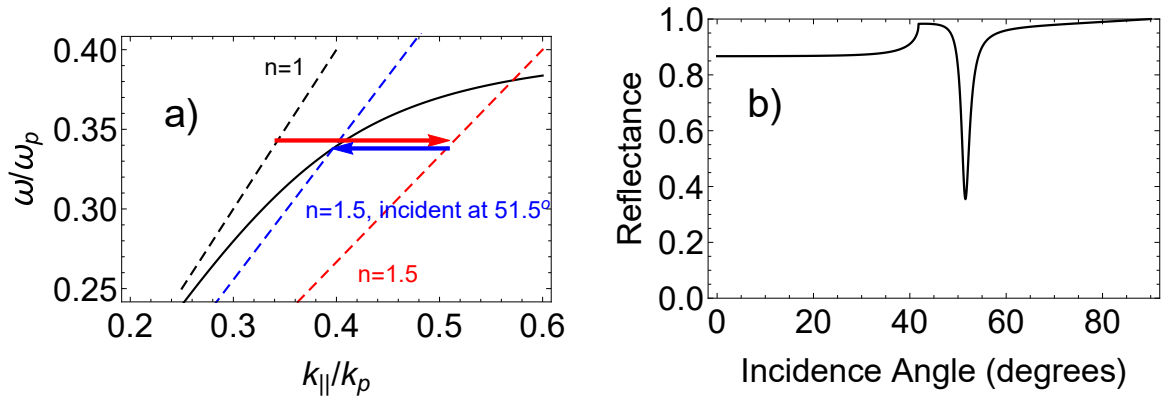
FIGURE 12. Attenuated total internal reflection mode diagram and associated surface plasmon resonance

a) Light from air (black dashed line) enters the prism dielectric, boosting k by the index of refraction (red arrow and red dashed light line). To excite the SPP, the light inside the prism strikes the prism/metal interface at an angle matching the k component parallel to the interface with that of the SPP mode (blue arrow and blue dashed light line). For $\omega = 0.34\omega_p$, the light line in silica crosses the SPP mode at an angle of 51.5^o, as shown. **b)** Reflectance as a function of the incidence angle from the prism to the system, for the mode diagram in **a**, with $\omega = 0.34\omega_p$. The angle is related to $k_\parallel$ by $k_\parallel = \sqrt{\epsilon}(\omega/c)\sin\theta$. The SPP mode is excited at an angle greater than the angle for total internal reflection, which the resonance minimum at 51.5^o.

can be varied to match the parallel k component to k_{sp} and excite the SPP mode. The arrows in Fig. 12(a) show the boosted wave vector, that is then adjusted to an appropriate angle to match $k_\parallel$ to the SPP mode.

We can also see this effect in the reflected light from the interface. In the reflectance, we can see a resonant dip in the total internal reflection from the higher index prism into the lower index dielectric layer. As an example of this, we consider the Kretschmann-Raether configuration with a silver film of thickness 55nm. The dielectric layer is vacuum (n=1), while the prism is fused silica (n=1.5). We use a frequency of $\omega = 0.34\omega_p$ ($\lambda = 400$nm). Reflection is calculated using standard Fresnel formulation for two interfaces[108]. Fig. 12(b) shows the surface plasmon resonance (SPR).
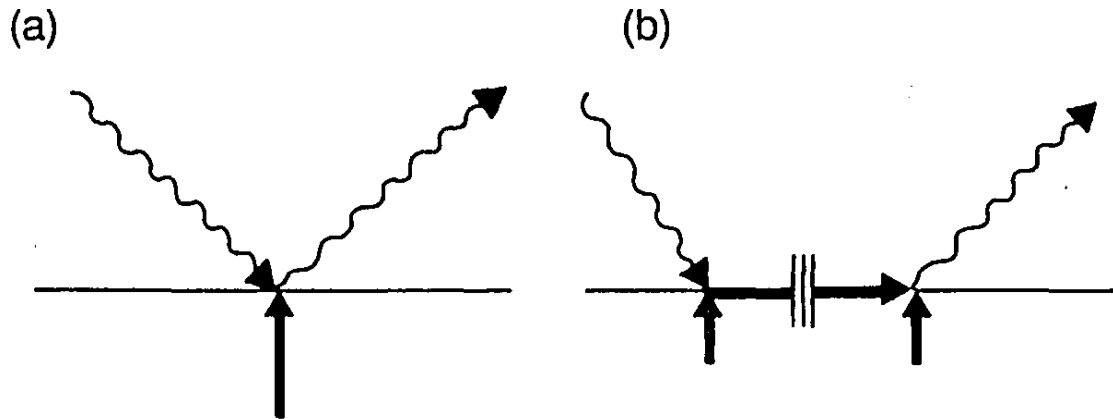
FIGURE 13. Surface plasmon indistinguishable pathways
Figure from [91]. Feynman diagrams of the two possible photon paths leading from the light source to the detector: **a)** total internal reflection, **b)** temporary conversion of the photon into a SPP and re-emission into the prism.

In this work we focus on the Kretschmann-Raether configuration. The experimental process for depositing silver onto the prism is often simpler and more precise than creating a dielectric spacer or film.

Surface Plasmon Polaritons as a Fano system

Fano interference occurs due to interference from two indistinguishable modes and SPR can be considered to be of this form[91]. The two pathways considered are direct total internal reflection (TIR) and the temporary conversion to a SPP, then re-emission into the prism, shown graphically in Fig. 13. TIR is excited for any angle above the critical angle for TIR, but the SPP is only excited for small range of wave vectors, and therefore a small range of angles. With this identification, the SPP takes the place of the discrete mode, while TIR is the continuum mode for Fano interference.

As mentioned in the chapter on Fano resonances, the SPR is one case of a geometric Fano resonance and the SPR shows the asymmetric nature of the Fano
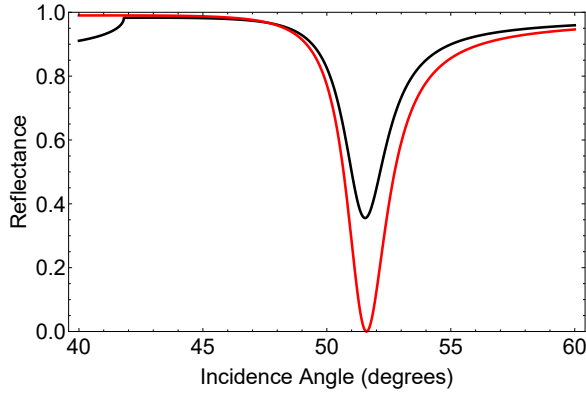
FIGURE 14. Surface plasmon resonance as a Fano resonance
SPR (black) and Fano lineshape (red). The SPR clearly follows the same trend at the Fano lineshape with a steeper slope below the SPR angle.

lineshape. The geometric Fano equation in terms of the angle is given by:

$$I(\theta) = \frac{(F\gamma + \theta - \theta_0)^2}{(\theta - \theta_0)^2 + \gamma^2} \tag{3.18}$$

where F and γ now represent the Fano parameter and line width, albeit in the angular domain. In Fig. 14, Eq. (3.18) is compared with Fig. 12(b) with $F = -0.1$, $\gamma = 1$ and $\theta_0 = 51.5^0$. Here, the Fano line shape is vertically scaled to have a baseline of the reflected intensity from the semi-infinite metal to match the intensity de-tuned from resonance. For both, the line shape shows a steeper slope at angles below the resonance angle than above the resonance angle. Below the critical angle for TIR ($\sim 42^0$), they deviate greatly as the TIR background is no longer available to support the excitation of the SPP mode.

As we move forward, the SP mode is used as the discrete state for a different continuum mode. In the next chapter we discuss waveguides and how they can take the role of the continuum mode for Fano interference.

CHAPTER IV

MULTILAYER SYSTEMS - MODES AND REFLECTANCE

In planar thin film systems, there can bound EM waves in the system, referred to as waveguide modes. Similar to the SPP bound mode, the fields propagate parallel to the interfaces, while decaying perpendicular to the interfaces, but unlike the SPP bound mode, optical modes can be confined without the need of metallic layers. Some guided waves are unable to propagate in the external insulator layers and are bounded in the waveguide film. Other guided modes can radiate into the exterior insulator and are called leaky waveguide modes. When you have metallic layers, SPP mode propagation becomes possible in addition to the waveguide modes. These systems have been covered previously[109], including the study of plasmonic waveguide modes[110, 111]. In systems with increasing number of layers, approximation solutions have been found due to symmetrical arguments[109, 112].

We have taken the analytical expression for increasing number of interfaces and analytically found the dispersion relations. By induction, we are able to write the mode dispersion for an arbitrary number of interfaces with arbitrary permittivities and thicknesses.

While this relation allows us to examine the modes for an arbitrary thin film system, it does not lend itself to an easy display. Because of this, we hold off showing this relation until App. A where the analytic expressions for the dispersive modes for multilayer thin film systems are calculated and shown, and App. B contains the code used for calculations in this dissertation. In this work, we focus on the TM modes of the waveguide. While TE modes exist in the waveguide structure, they do not couple to the SPP mode.

In this chapter we first discuss the nature of a finite thickness insulator thin film sandwiched between two semi-infinite silver-like metals. Second, we make one of the silver layers a finite film, which allows for the addition of a SPP mode at the new metal/insulator interface. Then with proper system parameters, we show the existence of a geometric Fano interference in this thin film stack. To show this, we look at the the mode diagrams, which exhibit an avoided crossing indicative of interference effects, then we add a prism, akin to the Krestchmann configuration for SPR, to look at the reflected intensity from the system.

Waveguide Systems

As stated above, two interface waveguide modes have been covered in the past and are now textbook material[109], and with the emergence of surface plasmon modes, the realization that coupled surface plasmon modes could exist in metallic waveguides arose[110, 111, 113, 114]. There are two standard layered systems, shown in Fig. 15, an insulator film sandwiched between semi-infinite metal cladding layers (MIM) and a metal film sandwiched between two semi-infinite insulator cladding layers (IMI). In each system, there can be two different couplings of the fields of the plasmonic modes: symmetric and anti-symmetric. The symmetric field coupling has large field confinement in the film, while the anti-symmetric field coupling has a larger field confinement in the exterior layer. For the two types of systems, MIM and IMI, the symmetric and antisymmetric couplings are called differently due to different interactions with the metal layers[111]. For MIM, because losses occur in metal, the symmetric mode, where the field is more confined to the insulator thin film, is called the long range surface plasmon polariton (LRSPP) and the anti-symmetric mode is the short-ranged surface plasmon polariton (SRSPP). Conversely, for the

30
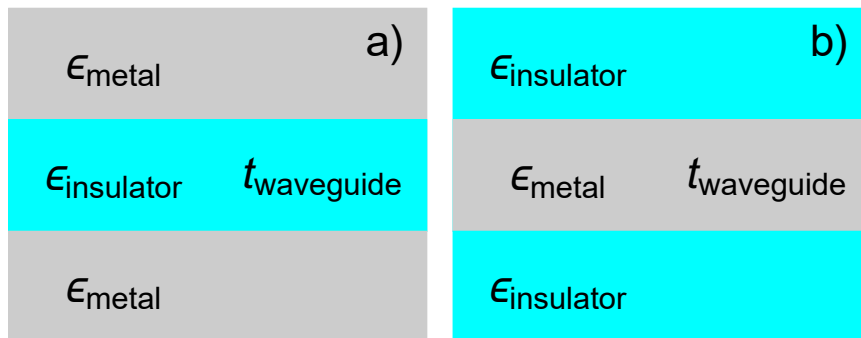
FIGURE 15. Metallic waveguide diagrams
Metal-insulator-metal (a) and insulator-metal-insulator (b) diagrams. The system is infinite in the plane of the interfaces and the capping layers are semi-infinite the in perpendicular direction. The only finite length is the film thickness as shown.

insulator-metal-insulator (IMI) system, the anti-symmetric mode is the LRSPP and the symmetric mode is the SRSPP. In this dissertation, we focus on the MIM system for our waveguide mode.

We start by looking at a TiO_2 film between two silver cladding layers. TiO_2 is chosen for its high permittivity and low losses in the visible frequencies ($\epsilon \sim 6.7$ in the visible)[115], and initially the thickness is chosen to be 80 nm.

Unlike the one interface system which contained a single mode, the MIM system has many different modes, shown in Fig. 16(a). The lowest energy mode is purely plasmonic in nature, and this mode is similar in description to the standard SPP modes. This mode favors lower frequencies as the surface plasmon frequency is much lower for TiO_2 than vacuum, as given by Eq. 3.17. The mode is described and explored thoroughly by Dionne et al[110, 111]. The plasmonic modes are special to metallic waveguides and does not appear if the cladding layers are insulators. This mode is not the focus of our work.

At higher frequencies than the plasmonic waveguide mode are similar to standard waveguide modes that would be observed in pure dielectric waveguides, but these modes are modified in comparison to pure dielectric modes by the presence of the

31

metal. Bands of allowable energies can be seen in Fig. 16(a). The lowest order metallic waveguide mode, which we will be focusing on for the rest of this dissertation, is symmetric in the electric field and anti-symmetric in the magnetic field, as can be seen in Fig. 16(b). As would be expected from resonance theory, the next higher order mode is anti-symmetric in the electric field and symmetric in the magnetic field, as the symmetry alternates as the energy levels are increased. We briefly discuss interactions with higher order waveguide modes later in this dissertation.

It is important to note, except for the lowest order plasmonic mode, that the waveguide modes cross the light line. These are leaky waveguide modes, and energy from the waveguide can be lost to an exterior insulator. This allows for free space light to be coupled into the waveguide from free space. For comparison to SPR, we make one of the silver cladding layers have a finite thickness and send input light from a now semi-infinite dielectric layer chosen to be fused silica ($n = 1.5$), shown as the inset in Fig. 16(c). Using the HeNe wavelength of 632.8 nm ($\omega/\omega_p = 0.224$) and a metal film thickness of 55 nm, the angle of incidence is varied. As expected, we see a resonance dip for the waveguide mode shown in Fig. 16(c), but unlike SPR, the dielectric input layer does *not* need to be a prism *and* does not need to have a higher permittivity than the waveguide due to the leaky nature of the waveguide mode.

Changing the thickness or permittivity of the waveguide insulator has the primary effect of changing the optical thickness of the waveguide; increasing the thickness or the permittivity both increase the optical thickness which shifts the modes to lower frequencies. Fig. 17 (a) shows the same mode for different thicknesses. We initially used a thickness of 80 nm which results in a waveguide mode being nearly flat. A thickness for a flat waveguide mode can be computed[116], but this thickness does not perfectly match with simulations, it is a good estimation for the desired
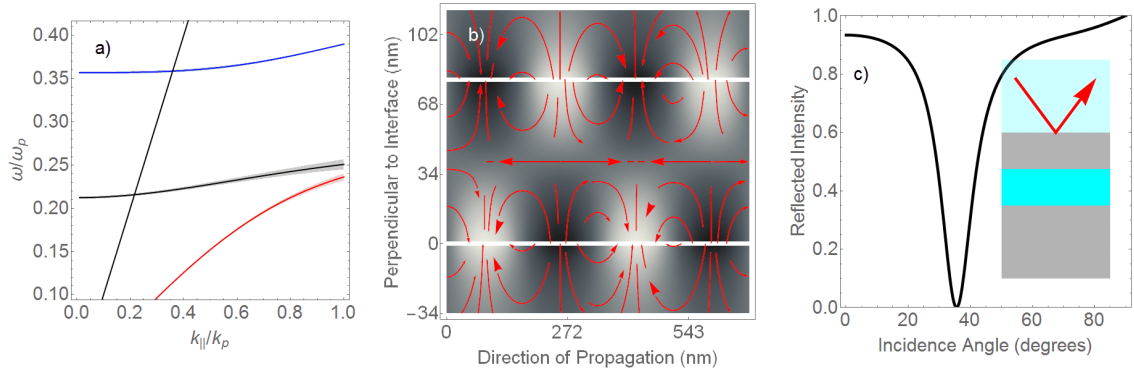
FIGURE 16. Metallic waveguide modes

a) TiO$_2$ film of thickness 80 nm sandwiched between two semi-infinite silver cladding layers. **a)** Modes for the MIM system. Three different modes are observed, the lowest mode (red) resembles the SPP mode while the black and blue modes resemble standard waveguide modes. The light line for vacuum is shown as the solid black line. **b)** Field distribution for the green line at $k_{||}/k_p = 0.4$ and $\omega/\omega_p = 0.223$. The magnetic field is given by the grey scale density function as is observed to be antisymmetric. The electric field is shown by the red lines, arrows indicate the direction of the field. The electric field is observed to be symmetric. **c)** Reflection for the MIM system with a Krestchmann configuration for inputting light into the system. For a wavelength of 632.8 nm ($\omega/\omega_p = 0.224$) a resonance dip is observed in the angular domain. **Inset** Schematic diagram of the system. The finite metal film has a thickness of 55 nm.

length scales in our waveguide. Higher thicknesses red shifts the mode to lower frequencies, while narrower waveguide thickness blue shifts the to higher frequencies. Note that the mode, regardless of the thickness, approaches the surface plasmon frequency as $k_{||}$ trends towards infinity. As noted before, decreasing the permittivity, such as using silica ($\epsilon = 2.25$), decreasing the optical thickness and shifting the mode to higher frequencies, shown in Fig. 17(a)[1].

When looking at the reflectance of the system as the thickness is varied, small changes to the waveguide greatly affect the resonance. Fig. 17 (b) shows the reflectance for three thickness in steps of 1 nm. The change of 1 nm shifts the

---

[1]Note that for silica the SP frequency is higher than for TiO$_2$, so the behavior as $k_{||} \to \infty$ is shifted to higher frequencies
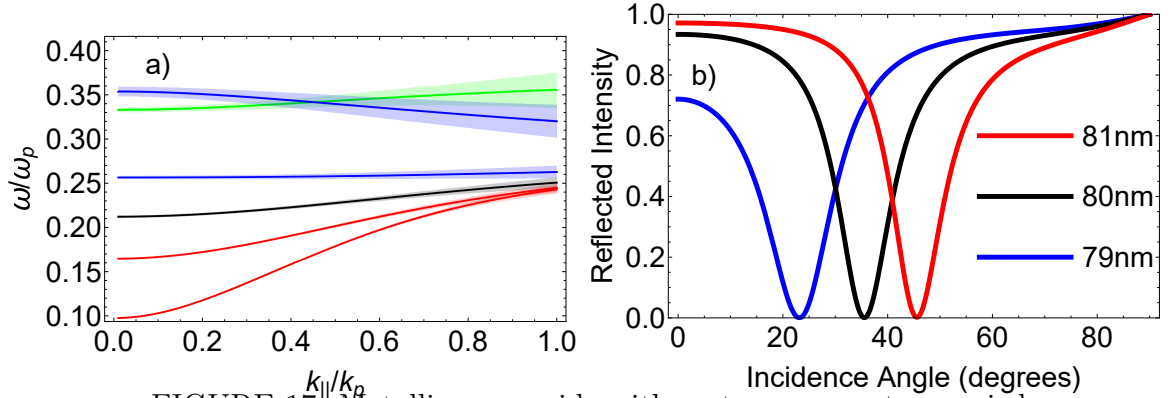
FIGURE 17. Metallic waveguide with system parameters varied

a) Mode diagrams for a MIM system. The black line is the same line in Fig. 16(a) for TiO$_2$ waveguide with thickness 80 nm. The red lines are for an increase to the film thickness, while the purple lines are for decreases to the film thickness. Also plotted is the same mode for a silica film, shown as a black line. Mode widths are given by the imaginary part of the eigenvalue solution. **b)** Reflections from the MIM system with a finite input metal film. Three different thickness in 1 nm steps are shown to greatly shift the resonance location.

resonance angle by 10°, showing an extreme sensitivity to the waveguide thickness. This is extremely useful as we can use this feature to change the resonance location as desired. This is exploited when adjusting the coupled system in the next chapter.

Fano Interference in Metal-Insulator-Metal-Insulator System

We now add an additional interface and insulator layer, so the system is now a metal-insulator-metal-insulator (MIMI). This new interface can support a SPP mode at the new metal/insulator interface, and the fields from the SPP mode can interact with the fields of the MIM mode, because the thickness of the metal film is chosen to be 70 nm, which is on the order of the decay length in the silver. This layer controls the coupling strength and is therefor called the metal coupling layer. Effects of changing the thickness, and thus the coupling, are explored later.
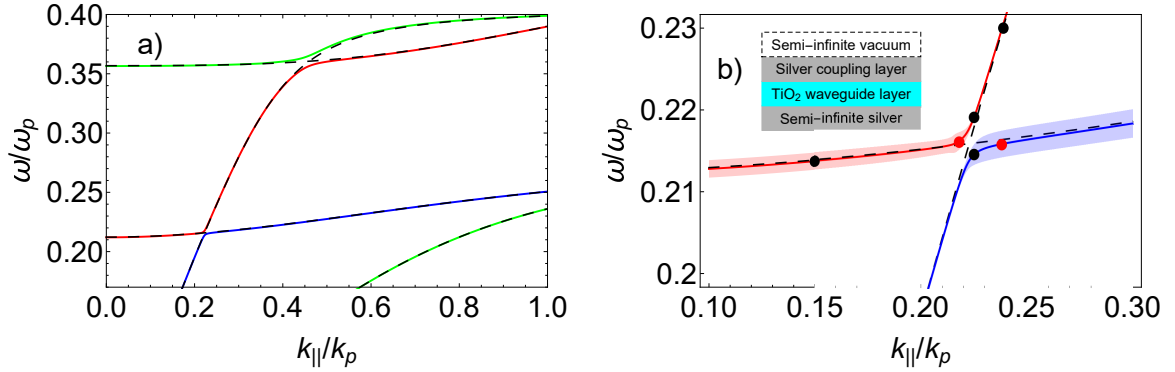
FIGURE 18. Metal-insulator-metal-insulator dispersion
a) The modes of the MIMI system are shown as the green, blue and red lines. The noninteracting SPP and MIM modes are given as the dashed lines. Three noninteracting MIM modes are shown, the same modes as in Fig. 16(a). Two separate avoided crossings appear in the MIMI dispersion. The avoided crossing at the lower frequency has the two modes colored red and blue to highlight the crossing. **b)** A zoom in of the lower frequency avoided crossing in a). The widths of the modes are given by the imaginary component of the eigenvalue solutions for the mode. In the region where the noninteracting modes cross, a clear avoided crossing is observed in the MIMI modes as the SPP and MIM modes interact. The black dots are reference points for the ω and $k_{||}$ values in Fig. 19 and the red dots are for values used in Fig. 20. **Inset** Schematic diagram of the MIMI system. For these plots, the silver coupling layer has a thickness of 70 nm and the TiO_2 waveguide layer has a thickness of 80 nm.

We first look at the modes of the system. Using the formalism as detailed in Appendix A, we calculate the modes of this new system, solid lines in Fig. 18, and we plot the noninteracting SPP and MIM modes, shown as dashed lines. In the frequency and wave vector range in which the noninteracting SPP and MIM modes cross, we see a avoided crossings in the MIMI modes, indicative of the Fano interference. The modes of the lower frequency crossing have been colored red and blue to show the continuation of each mode. Specifically we will focus on the red/blue modes at lower frequencies, or the lower frequency anti-crossing.

The two noninteracting modes experience hybridization in regions in which they interact[67], which is observed as the modes evolve from a MIM-like field distribution

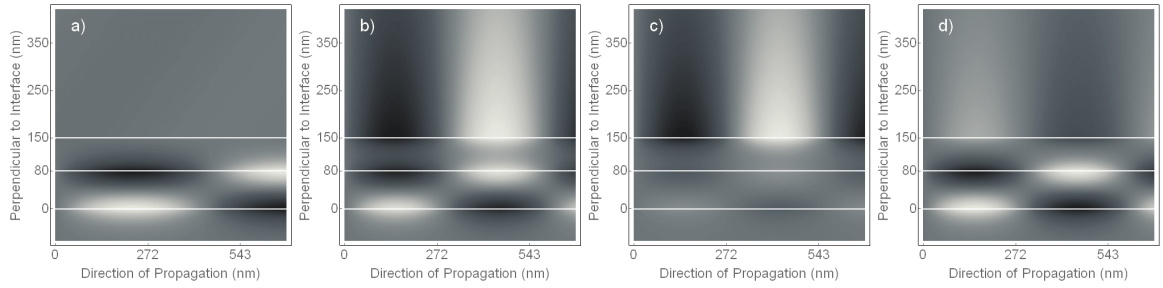FIGURE 19. Metal-insulator-metal-insulator magnetic field plots
The magnetic fields of the MIMI modes for values shown as black dots in Fig. 18(a). The interfaces are given by the horizontal white lines at 0, 80 nm and 150 nm. **a)** $\omega = 0.214\omega_p$, and $k_{||} = 0.150k_p$, the fields are confined to the waveguide layer. **b)** $\omega = 0.219\omega_p$, and $k_{||} = 0.225k_p$, here the field exists in both the waveguide and SPP modes. **c)** $\omega = 0.230\omega_p$, and $k_{||} = 0.239k_p$, the fields are confined to the exterior interface, thus in the SPP mode. **d)** $\omega = 0.215\omega_p$, and $k_{||} = 0.225k_p$, a field plot for the lower mode. Here the field exists in both the waveguide and SPP modes, but with a different symmetry than (b), which has the same value for $k_{||}$.

to a SPP-like distribution as the frequency moves through the region of interaction. Fig. 19(a-c) shows the magnetic field distribution as we step through this region for the upper mode in Fig. 18(a). At $k_{||} = 0.15k_p$, Fig. 19(a), the MIMI field distribution is tightly confined to the waveguide layer and the mode is strongly MIM-like. At $k_{||} = 0.225k_p$, Fig. 19(b), the field distribution is now found in both modes, as would be expected in the region of interference. And finally, at $k_{||} = 0.15k_p$, Fig. 19(c), the MIMI field distribution is tightly confined to the exterior interface, and the mode is significantly SPP-like. We also observe the lower mode at $k_{||} = 0.225k_p$ in Fig. 19(d). Here the fields are in both modes, but we observe a shift in the relative phase of the field distributions from Fig. 19(b). For the higher energy mode, the magnetic fields regions of high amplitude are in phase with each other, a symmetric coupling, and as expected, for the lower energy mode's magnetic field distribution at the exterior interface are out of phase with the fields at the closer waveguide interface, or the asymmetric coupling.
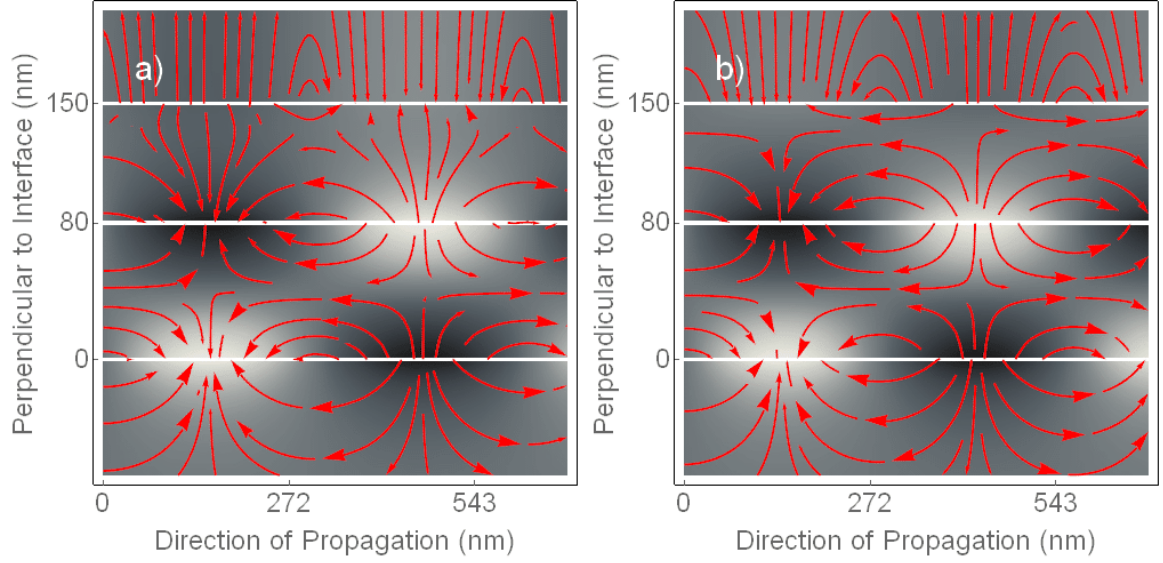
FIGURE 20. Metal-insulator-metal-insulator electric field plots
The magnetic and electric fields of the MIMI modes for values shown as purple dots in Fig. 18(a). The interfaces are given by the horizontal white lines at 0, 80 nm and 150 nm. **a)** $\omega = 0.216\omega_p$, and $k_{||} = 0.218k_p$. Within the waveguide insulator (0 - 80 nm), we observe the fields for the MIM mode as seen in Fig. 16(b). The electric field in the metallic coupling layer (80 nm - 150 nm) now shows a antisymmetric distribution of the electric field as the field lines point directly from one interface to the other. **b)** $\omega = 0.216\omega_p$, and $k_{||} = 0.238k_p$. The electric field in the metallic coupling layer now shows a symmetric distribution of the electric field, as the field lines parallel to the interface point in the same direction.

The different phase of the two modes is also observed in the electric fields, as shown in Fig. 20, where we plot the magnetic and electric fields of the MIMI modes for $\omega = 0.216\omega_p$, and $k_{||} = 0.218k_p$ and $k_{||} = 0.238k_p$. Looking at the fields in the metallic coupling layer (80 - 150 nm from the interface), the electric field is anti-symmetric and symmetric in direction for Fig. 20 (a) and (b), respectively. As was the case for the MIM fields distributions, the magnetic and electric fields have opposite symmetries.

This MIMI stack has the same layers as was used for the MIM reflectance in the previous section. The interference effect was not observed in Fig. 16(c), due to the region of interest happening outside of the light cone. This comes directly from the
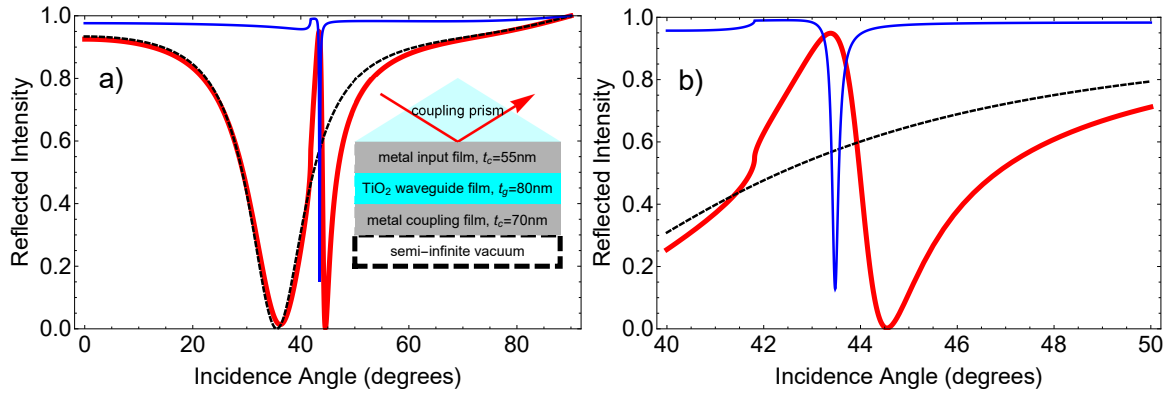
FIGURE 21. Reflectance from a prism-metal-insulator-metal-insulator stack
A TiO$_2$ film of thickness 80 nm sandwiched between silver films. This infinite
sandwich is capped by a silica prism on one side and semi-infinite vacuum on the
other. The metal input film abutting the prism has a thickness of 55 nm and the
metal coupling film abutting the semi-infinite vacuum has a thickness of 70 nm.
Light of wavelength 632.8 nm is incident on the system from the prism. The PMIMI
reflectance is given by the red line. Also included are the SPR (blue thin line) and
the MIM resonance (black dotted) with an metal thickness of 55 nm for both. **a)**
Reflectance from the systems in the full range of angles (0-90°). **Inset** Schematic
diagram of the system. **b)** A narrowed angular range to focus in on the GFR. The
asymmetric Fano lineshape is observed for the PMIMI system. Away from the GFR
the PMIMI lineshape follows the MIM resonance as expected. In the direct region of
the SPR a strong transparency is observed.

fact that we are unable to excite the SPP mode at the metal/vacuum interface with
light incident from the vacuum.

In the next section we discuss the addition of a prism which admits a resonance
in this metal/insulator thin film stack.

Geometric Fano Resonance in a Metal-Insulator-Metal Sandwich

In analogy to the Kretschmann Configuration used for SPR, we now add a prism
to the MIMI stack. This is shown schematically as the inset in Fig. 21(a). We call
this system a prism-metal-insulator-metal-insulator (PMIMI) stack. The parameters
we use are the same as explored for the MIMI stack, with the addition of a finite

input metal thickness and the prism layer is treated as a semi-infinite silica layer ($\epsilon = 2.25$). The metal film abutting the prism is referred to as the metal input film, and is silver with a thickness of 55 nm. Sandwiched between two of the metal films is a TiO$_2$ waveguide film of thickness 80 nm. The second metal film is referred to as the coupling metal film because it couples the MIM and SPP modes. The metal coupling film has a thickness of 70 nm. Abutting this metal coupling film is a semi-infinite vacuum layer. We use the HeNe wavelength of 632.8 nm ($\omega = 0.216\omega_p$) for the input light.

We plot the reflected intensity from this PMIMI stack in Fig. 21. As expected from the modes in Fig. 18, a geometric Fano resonance occurs in this PMIMI stack. Also included in Fig. 21 are the noninteracting noninteracting SPR and MIM resonance. For the SPR, a film thickness of 55 nm was used and we see the resonance location at 43.5^0. As can be observed more clearly in Fig. 21(b), the critical angle for TIR occurs at 41.8^0 at the cusp in the SPR and PMIMI lines. This angle is for the parameters of going from silica to air, and does not appear in the waveguide resonance, because there is no TIR as the TiO$_2$ waveguide is a higher permittivity than silica. In the angular range of the SPR, we observe a Fano lineshape in the angular domain for the PMIMI stack, and far detuned from the SPR angle, the PMIMI line shape follows the MIM resonance, which is a general feature of all Fano resonances.

To show the PMIMI response of the system, we plot the magnetic field in the system for several different input angles. This is done in Fig. 22 for 35°, 43°, 43.4^o and 44°. In Fig. 22(a) we show the field when on resonance of the waveguide mode, and the field is completely contained in the waveguide. This angle is far detuned from the SPR angle and experiences no effects from the coupling, and it is below the critical angle for TIR, so the SPP mode cannot be accessed at all. Just above the
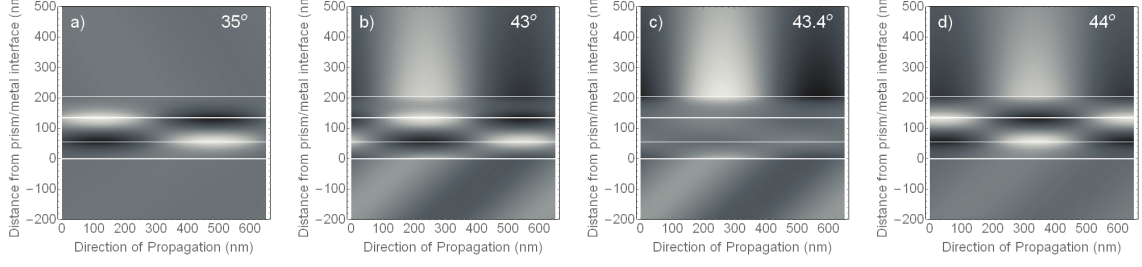
FIGURE 22. Prism-metal-insulator-metal-insulator magnetic field plots
The magnetic fields of the PMIMI system for four different input angles. The interfaces are given by the horizontal white lines at 0, 55 nm, 135 nm and 205 nm. **a)** $\theta = 35^o$, the fields are confined to the waveguide layer. **b)** $\theta = 43^o$, here the field exists in both the waveguide and SPP modes, as well as a reflected field is observed. **c)** $\theta = 43.4^o$, most of the field is reflected, while some remains at the SP interface. The field in the waveguide has been quenched. **d)** $\theta = 44^o$, here the field is again in both modes, however the symmetry of the fields has switched from $\theta = 43^o$.

critical angle at 43°, the SPP and MIM modes are accessible to the input EM field, shown in Fig. 22(b), and the fields are symmetric about the coupling film. Compare this plot with Fig. 19(b), in which $k_{||}$ is lower than the region of highest interference and see the same symmetry of the fields. As the reflected intensity is nonzero, we also observe freely propagating waves in the prism. In Fig. 22(c), the field has been quenched from the MIM mode and is only in the SPP mode and the reflected field. Lastly, we see in Fig. 22(d) that beyond the maximum of intensity at 44°, and the symmetries of the fields in the SPP and MIM modes have swapped. At this point we have gone to the other MIMI mode where the fields flup symmetries, as observed in Fig. 19(d).

We can also examine the GFR by plotting three separate views of the reflected field in Fig. 23. In Fig. 23(a) we plot the intensity and phase of the field. This is the the same as in Fig. 21, but now we have added a plot of the phase. It is important to know the intensity as this is what would be experimentally observed in an output detector, and the phase will is useful for integration into interferometric systems.
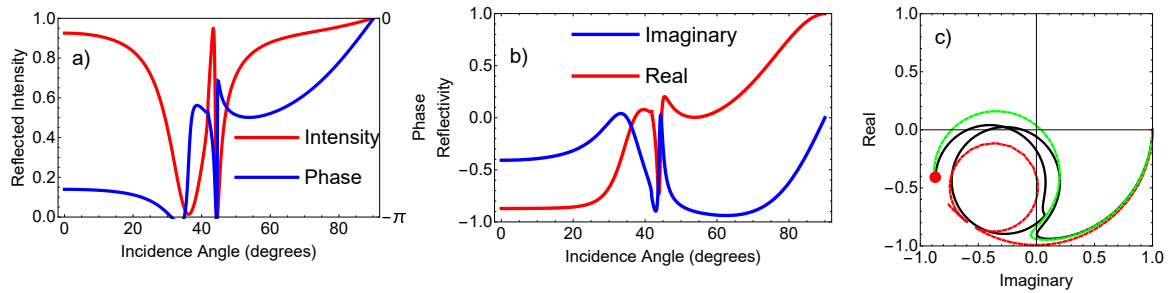
FIGURE 23. PMIMI reflected field represented in three ways
For the same parameters used in Fig. 21, we plot the reflected field in three ways. Each plot gives insight into different aspects of the field. **a)** Intensity and Phase. Shows experimental achievable output intensity, as well as phase for possible interference effects. **b)** Quadratures plotted independently. This allows for direct analyzing of the fields components. **c)** Polar plot of quadratures. Contains the same information as (a) and (b), but does not give insight into the angular location of the resonance. The non interacting SPR and MIM resonance are shown as the red and green dotted lines, respectively. The red dot indicates $\theta = 0$ for the MIM and PMIMI.

Fig. 23(b) plots the real and imaginary parts of the reflected field. The field response of this GFR is analogous to the quadratures of an atomic dressed system[50], which provides a useful analogy. Lastly, we show a polar plot of the field in Fig. 23(c). For reference of direction, a red dot has been added at $\theta = 0^o$. As the angle of incidence is increased, the line is continuous and smooth, with the exception of the TIR critical angle which appears as a cusp. An important feature to note is that the resonance curves appear to be loops in the polar plot. In this case, we have two loops, one from the interactions of the MIM resonance and one from the SPR. This is explored further later in this dissertation.

It should be noted that the addition of the silica prism adds another metal/insulator interface. At this metal/insulator interface, a SPP mode exists. This SPP mode is shifted to lower frequencies compared to the vacuum SPP mode and this silica SPP mode interferes with the waveguide mode, albeit at a different wave vector than the vacuum SPP mode. This effect is shown in Fig 24. In comparison to
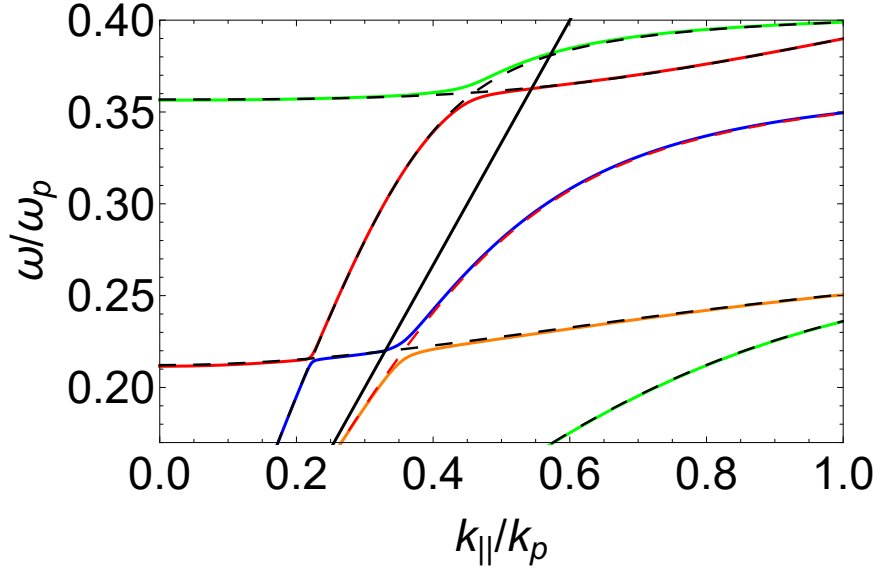
FIGURE 24. PMIMI modes

A TiO$_2$ film of thickness 80 nm sandwiched between two finite silver films. The sandwich is contained by a semi-infinite vacuum cladding on one side and a silica cladding on the other. The non interacting silica SPP mode is given by the red dashed line. The addition of the prism cladding layer modifies the modes in comparison to Fig. 18. There is the addition of the SPP mode for the silica/metal interface. The avoided crossing of the modes lies outside of the light cone for silica (solid black line) and is not observed in the reflected fields.

Fig. 18, there is an additional avoided crossing of the PMIMI where the noninteracting silica SPP mode crosses the waveguide mode. This interference region lies outside of the light line for silica. As such, we do not see the interference effect from the light in the silica, but it is interesting to note that if this second avoided crossing was to be explored via input light, an additional momentum matching scheme would be required.

As a final comment on the PMIMI stack, we look at the resonance in the frequency domain. In doing so, we see that the Fano resonance occurs only in the angular domain making this resonance a Geometric Fano Resonance.
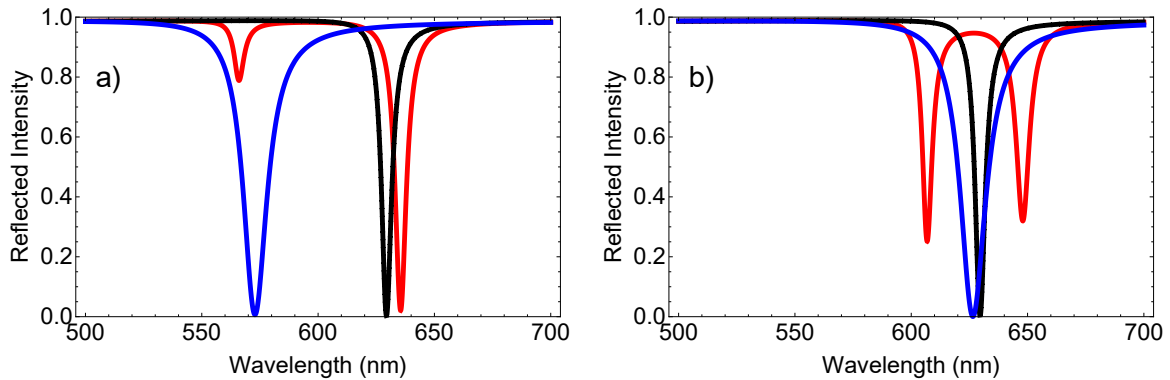
FIGURE 25. PMIMI reflectance in the frequency domain
Reflectances for the PMIMI (red), the SPR (blue) and the MIM resonance (black dotted) for two different angles: **a)** 44° and **b)** 43.5^o. The PMIMI line shapes do not represent the Fano line shape.

Reflectance vs. Frequency

So far we have purely explored the angular domain while looked at the reflected field, claiming a geometric Fano resonance. In Fig. 25, we plot the reflected intensity for two fixed angles in the spectral domain as a function of the wavelength for the PMIMI, SP and MIM resonances. The SPR and MIM resonances are shown as the blue and black/dashed lines respectively. In the spectral domain, the MIM resonance has a lower resonance width that the SPR. This is due primarily to the fact that the MIM mode is nearly horizontal and is excited by a narrow range of frequencies. The SPR is not horizontal and a large range of wavelengths excite the SPP mode. The PMIMI line does not exhibit the Fano line shape. First looking at Fig. 25(a) for an angle of 44°, we see two separate resonances in the line for a large detuning of the noninteracting resonances, and both are modified from the noninteracting SPR and MIM resonance. The difference between the two independent resonances and a Fano line shape is illuminated in Fig. 25(b) in which the two greatly overlap. In this case, the PMIMI line shape still appears as two separate resonances and not a single Fano resonance. This distinction has its atomic analog and is described as the difference

43

between Fano interference and Autler-Townes splitting[117]. In this case, the line shape in the spectral domain is reminiscent of two separate resonances, as opposed to two modes interfering destructively.

Due to the lack of a Fano resonance in the frequency domain, we focus only on the angular domain to explore the GFR. In the next chapter, we vary the material parameters of the PMIMI stack to see the effects on the GFR line shape.

CHAPTER V

MATERIAL PARAMETER VARIATION IN THE METAL/INSULATOR
SANDWICH

As one would expect, the physical parameters of the system affect the resonances of a system. In traditional Lorentz resonances, the two main features that are affected are the resonance depth and line width. In Fano resonances there is also an additional variation of the asymmetry parameter, as mentioned in chapter II. This additional tunability allows for more drastic changes to the line shape over a simple Lorentz resonance. In non-atomic systems, such as plasmonics and waveguide systems, variations to the material parameters are easily achievable experimentally, and these have been demonstrated in many Fano analog systems[56, 58, 61–64, 68, 69, 71, 72, 118–120].

The GFR seen in our PMIMI stack depends on the physical parameters of the stack. This chapter is dedicated to observing the effects of each material parameter on the PMIMI modes and we focus on the reflected intensity of the resonance. A discussion of phase occurs in chapter VI.

Variations to the parameters of each individual layer affects the overall resonances differently. The permittivity of the exterior semi-infinite insulator layer modifies the modes of the noninteracting SPP mode, and in effect modify the SPP contribution to the coupling. The thickness and permittivity of the waveguide insulator layer modify and affect the noninteracting MIM mode and the MIM contribution to the coupling. The metallic coupling film between the insulators controls the coupling strength between the interacting MIM and SPP modes. Finally, we discuss the metallic input film between the waveguide and the prism and the effects on the GFR.

In this chapter, we use the parameters for the PMIMI stack in the previous chapter as a base line, where the prism is treated as a semi-infinite silica layer (ϵ_p=2.25), the metal input film is silver with a thickness of 55 nm, the waveguide film is TiO$_2$ with a thickness of 80 nm[115], the metal coupling film has a thickness of 70 nm, and the semi-infinite exterior insulator is vacuum (ϵ_e=1). We only consider Ag for our metal layers. Using different metals allows for the same effects to be observed in different frequency ranges with different losses in the system. Au, for example, has a lower plasmon frequency and is more suitable for use in the infrared. We continue to use the HeNe frequency for reflection plots.

Waveguide Film

We first discuss variations to the waveguide film, where changes to this film can be treated as variations to the noninteracting MIM mode, and we can use our knowledge of the waveguide modes in the previous chapter as a guide for changes to our GFR. Generally, increasing the optical thickness results in a lowering of the frequency of the mode, and vice versa for decreasing the optical thickness. Looking at the noninteracting MIM resonance, this results in a higher resonance angle for the increased optical thickness and a lower resonance angle for decreased optical thickness. Because of this it is possible for the noninteracting MIM mode to be moved out of the frequency and angular range we are interested in, which results in an absence of the waveguide resonance in the angular reflectance. This in turn eliminates the GFR from our selected frequency as the SPP and MIM modes do not intersect in the available wave-vector range at the given frequency.
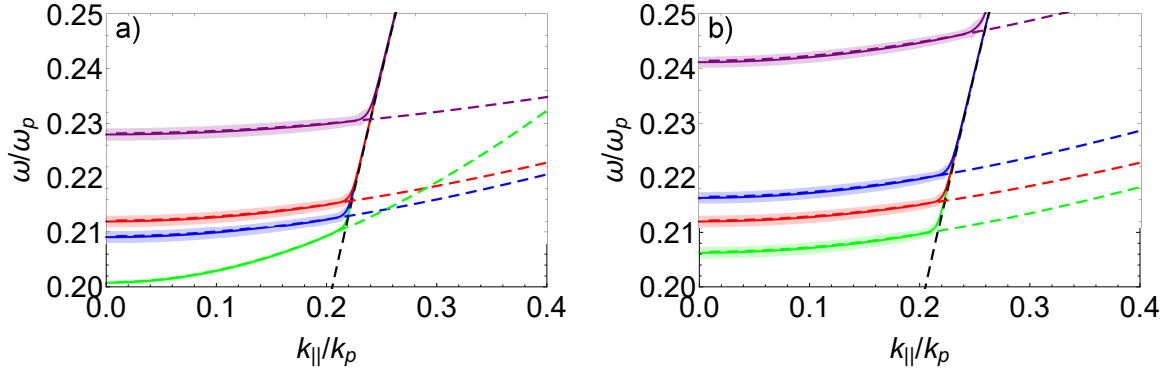
FIGURE 26. Waveguide variations - mode plots

a) Modes for the MIMI system (solid) and noninteracting MIM and SPP modes (dashed) for different thicknesses. The widths of the MIMI modes are given by the imaginary component of the complex eigenvalue solution for the mode. The nearly vertical black dashed line is the SPP mode. The thickness of the waveguide for both the MIMI and MIM modes are 70 nm (purple), 80 nm (red), 82 nm (blue) and 220 nm (green). **b)** Modes for the MIMI system (solid) and noninteracting MIM and SPP modes (dashed) for different permittivities. The widths of the MIMI modes are given by the imaginary component of the complex eigenvalue solution for the mode. The nearly vertical black dashed line is the SPP mode. The permittivity of the waveguide for both the MIMI and MIM modes are 5 (purple), 6.37 (blue), $TiO_2 \sim 6.67$ (red) and 7.07 (green).

Waveguide Film Modes

In Fig. 26 we plot the MIMI stack mode as we vary the thickness, t_g, and permittivities, ϵ_g, of the waveguide. For the MIMI system, we only plot the higher frequency mode, allowing for clear observation of the MIM modes at higher wave vector. Note that both the thickness and permittivity affect the modes of the system, changing the mode away from the baseline. Decreasing the thickness or permittivity brings the modes to higher frequencies, as this can be seen in Fig. 26(a) for thicknesses, or in Fig. 26(b), for permittivities, and conversely increasing the thickness or permittivity brings the modes to lower frequencies.

We also can move the higher order MIM mode into the frequency range of by increasing the thickness further. At a thickness of 220 nm, the next higher order

mode is observed in Fig. 26(a) as the green line. This mode is not nearly as flat as the lowest order mode and results in a narrower resonance, as shown below in Fig. 27(a). Additionally shown in Fig. 26(b), an increased permittivity of 7.07 (green) decreases the frequency of the mode, but for realistic values of permittivity, it is not possible to observe higher order modes for the thickness of 80 nm.

The ability to tune the dispersion by varying the waveguide thickness and permittivity allow for the non interacting MIM mode to cross the SPP mode at any frequency. This allows us to tune the avoided crossing to many different frequencies. Next, we discuss the reflectance observed for the PMIMI system while varying these parameters.

Waveguide Film Reflectance

In Fig. 27 (a) and (b), we plot the GFR of the PMIMI system for a wavelength of 632.8 nm for varying thicknesses and permittivities of the waveguide. Additionally shown in both plots are the noninteracting MIM resonance as a black dashed line for each PMIMI line. The baseline parameters GFR are shown in both plots as the red lines and Fig. 27(a) is generated by varying the thickness and Fig. 27(b) by varying the permittivity.

To start, let's examine the effect of the thickness in Fig. 27(a). Beginning at the baseline 80 nm and increasing the thickness by 0.5 nm steps to 82 nm, we see the noninteracting MIM resonance shift its resonance angle by 20° per 2 nm change. This shows a large sensitivity of the MIM and PMIMI resonances to the thickness of the waveguide. During this resonance shift, the GFR of the PMIMI system undergoes a q-reversal as the relative location of the MIM resonance angle to the SPR angle switches. At 80.83 nm, the SPR and MIM resonance share the same resonance angle.
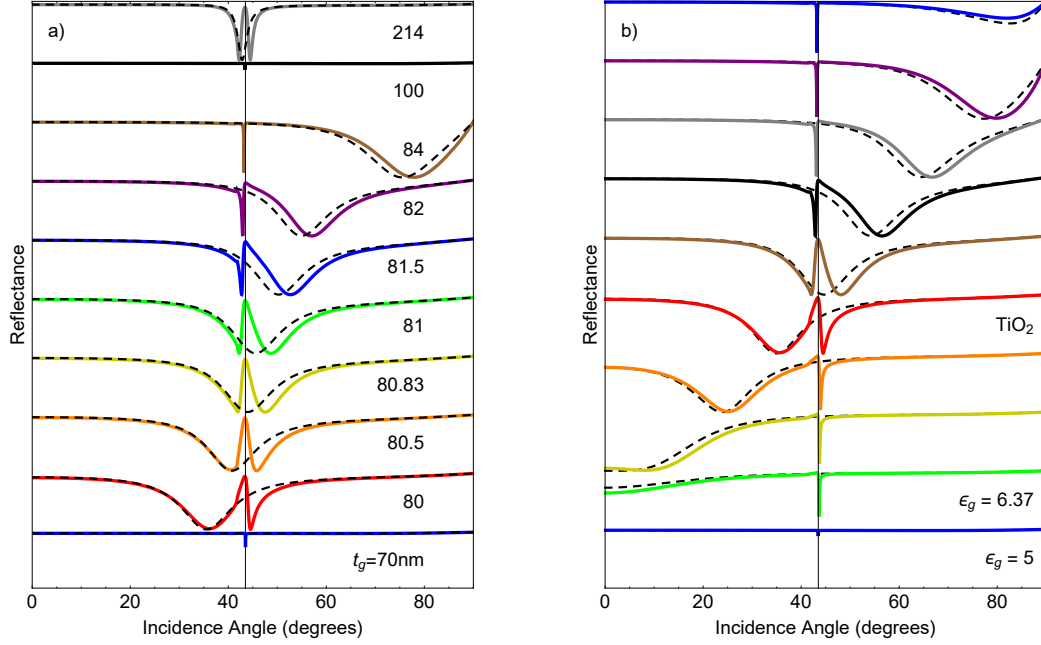
FIGURE 27. Waveguide variations - reflectance plots

a) Reflectance for the PMIMI system (solid) and noninteracting MIM (dashed) for different thicknesses. The vertical black line is the SPR angle. The thickness of the waveguide is given under each line. The baseline GFR with $t_g = 80$ nm thickness is shown as the red line. **b)** Reflectance for the PMIMI system (solid) and noninteracting MIM (dashed) for different permittivities. The vertical black line is the SPR angle. The lowest blue line is for a permittivity of 5. The green line above it is 6.37. Each line above that steps up the permittivity by 0.1, up to 7.17 for the top blue line. The baseline GFR for TiO_2 is shown as the red line.

Near this thickness, the GFR appears as an increase of the output field in comparison to the MIM resonance, and this is analogous to EIT. It is called a plasmon induced transparency (PIT), and in this case, the transparency is in the reflected field unlike EIT where the transparency is in the transmitted field. At 84 nm, we observe that the SPR and MIM resonance are far detuned from each other. For this thickness, the two modes still interact, but the coupling strength between the two is quite small and each resonance is only slightly modified from the noninteracting resonance.[1]

---

[1]This has region of parameters has been explored for its sensing capabilities and is called Waveguide Coupled Surface Plasmon Resonance (WCSPR)[121, 122].

It is important to note that the SPP mode is excited by input light that has traveled through 135 nm of silver films. The coupling between the modes allows for the energy transfer through the films, but the field strength inside the films is drastically decreased due to the destructive interference of the MIM and SPP fields in the metallic layers. For thicknesses in which the MIM mode does not occur in our frequency and wave-vector range, such as 70 nm or 100 nm, the SPP mode is screened by the metal layers and the SPR is weakly observed, though as discussed above, the higher order mode can be excited at even larger thickness. The top most plot in Fig. 27(a) shows this possibility as it clearly has the GFR (for 214 nm thickness), when both the noninteracting MIM resonance and GFR show a decrease in the resonance line width as expected.

In Fig. 27(b) we examine changes to the GFR from changes to the permittivity of the waveguide film. The observations are quite similar to the effects seen in the variations of the waveguide thickness. however there is a difference in the relative insensitivity to the permittivity. With a change of the permittivity by 1, the entire evolution of the GFR is observed, which is a wide range of permittivities compared to the small 10 nm variation in thickness to see the same effect. For a permittivity of 5, the noninteracting MIM mode is out of range of wave vectors for our baseline, as seen in Fig. 26(a), and as such for this frequency there is no MIM resonance; only a weakly excited SPR is observed. Moving up one plot, the permittivity is 6.37 and we observe a SPR-like resonance when the MIM and SPR resonances are far detuned. As we step the permittivity by 0.1 steps, we see the shifting of the independent MIM resonance to higher angles. This in turn changes the asymmetry parameter of the GFR as we observe the GFR change and undergo q-reversal, as expected. We once again observe the SPR-like WCSPR at large detunings of the SPR and MIM resonance.
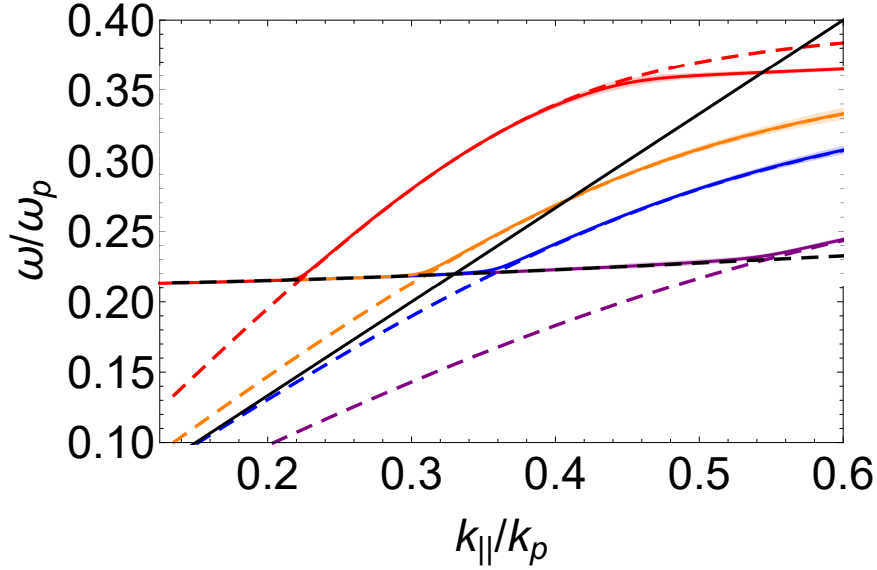
FIGURE 28. Exterior permittivity variations - mode plot
Modes for the MIMI system (solid) and noninteracting MIM and SPP modes (dashed) for different permittivities. The widths of the MIMI modes are given by the imaginary component of the complex eigenvalue solution for the mode. The nearly horizontal black dashed line is the MIM mode. The exterior permittivity for both the MIMI and SPP modes are $\epsilon_e = 1$ (red), $\epsilon_e = 1.78$ (water, orange), $\epsilon_e = 2.25$ (silica, blue) and TiO_2 $\epsilon_e \sim 6.67$ (purple). The black solid line is the light line in fused silica A deviation in the vacuum MIMI line occurs at higher frequencies due to the interacts with a higher waveguide mode. This waveguide mode is not shown.

The ability to tune the waveguide thickness and permittivity allow for the non interacting MIM resonance to be shifted in comparison to the SPR, which allows for the tuning of GFR to a desired shape with fine tuning of the permittivity and thickness of the waveguide for a given exterior insulator. Next we discuss variations to the exterior permittivity.

Exterior Insulator Variations

We now look at the semi-infinite exterior insulator layer. This layer has the primary effect of varying the SPP contribution to the Fano resonance. Increasing the permittivity, ϵ_e, decreases the surface plasmon resonance as shown by Eq. 3.17, which

results in a general shift of the SPP mode to lower frequencies, and thus higher wave vectors for a given frequency and a shift of the SPR to higher angles.

The modes of the MIMI system for different exterior permittivities are shown in Fig. 28. As before, the non interacting modes are given by the dashed lines and the MIMI modes are the solid lines. We only plot the higher frequency mode to show clearly the noninteracting SPP modes below. The red line is for the base parameter; in this case vacuum. As in Fig. 18(a), we observe a deviation at higher frequencies from interactions with the higher order waveguide mode. We also show three higher permittivities: water, $\epsilon_e = 1.78$; fused silica, $\epsilon_e = 2.25$; and TiO_2, $\epsilon_e \sim 6.67$ (the same as the waveguide). Increasing the permittivity adjusts the noninteracting SPP mode to higher wave vectors along the MIM line, which shifts the avoided crossing to higher wave vectors. It is important to note that with the fused silica prism, all the avoided crossings shown would not be accessible, because only the wave vectors to the left of the line are accessible. As expected from the regular Kretschmann configuration, the light can only couple to the resonance when the exterior permittivity is lower than the prism permittivity. For this reason, we limit our exterior permittivities to values less than that of silica.

For Fig 29(a) we increase the permittivity from 1 to 2 in increments of 0.2. As expected, the resonance location shifts to the right, as does the non interacting SPR. The plot for $\epsilon_e = 2$ does not exhibit the SPR-like shape and follows the MIM resonance, due to a shifting of the avoided crossing to the light line of fused silica. In Fig 29(b) we change the waveguide thickness to 82 nm. This shifts the MIM resonance to a higher angle and we can now observe q-reversal via increasing the exterior permittivity. From the three plots with $\epsilon_e = 1$, $\epsilon_e = 1.4$ and $\epsilon_e = 1.8$, we observe the q-reversal as the $\epsilon = 1.4$ GFR exhibits the PIT. As with the waveguide
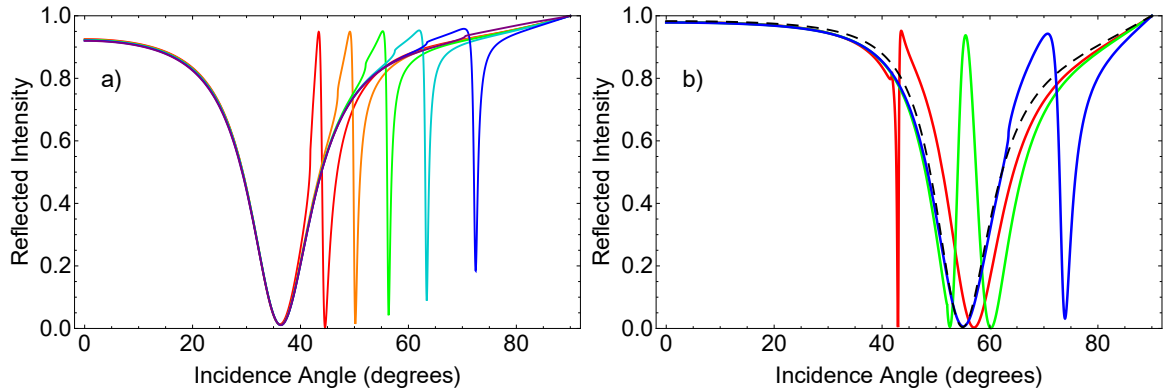
FIGURE 29. Exterior permittivity variations - reflectance plots
a) Reflectance for the PMIMI system for different permittivities. Starting with the red line with $\epsilon_e = 1$, the permittivity is increased by steps of 0.2. The last is the purple line with $\epsilon_e = 2$ in which only the MIM resonance is observed. **b)** Reflectance for the PMIMI system for a waveguide thickness of 82 nm for three different permittivities: 1, 1.4 and 1.8. The noninteracting MIM resonance is shown as the black dashed line. From 1 to 1.8, a clear q-reversal is observed, and 1.4 shows a clear transparency.

film, the exterior permittivity can be tuned to give a desired GFR lineshape. With the two waveguide parameters and the exterior permittivity, we are able to shift the resonance to a given frequency and wave vector at will.

We now discuss the metallic coupling layer that controls the coupling strength of the modes.

Coupling Metal Film Thickness

The coupling film determines the spatial overlap of the fields in the waveguide and the exterior interface. We start with the extreme of a large coupling film thickness, t_c, such as 200nm, in which there is no spatial overlap of the fields, and thus no coupling. The two modes can be considered completely noninteracting and cross normally in the mode diagram, which is not shown as the modes are trivial. When attempting to put light into the system from the prism, the energy is unable to penetrate the
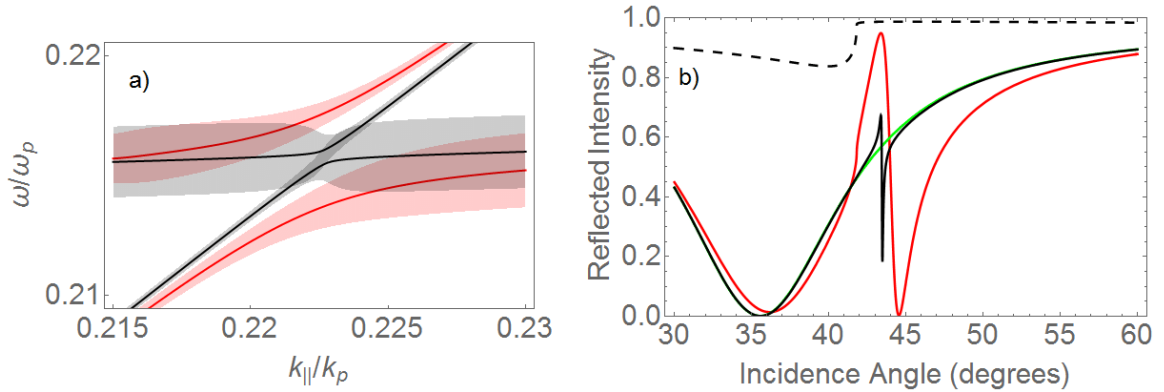
FIGURE 30. Coupling film variations
a) Dispersion modes for two coupling films thicknesses; 70 nm (red) and 110 nm (black). The increased thickness decreases the center to center mode separation. **b)** Reflectance for different coupling film thicknesses. In addition to the 70 nm (red) and 110 nm (black) lines corresponding to the modes in a), we show a large thickness of 200 nm (green) and a small thickness of 20 nm (black and dashed).

coupling film, and is only input into the waveguide mode. Therefore you see the MIM resonance as shown in Fig. 30(b) as the green line.

As we decrease the thickness of the coupling film and the fields of the modes begin to overlap spatially, a small avoided crossing occurs in the modes. At 110 nm, the avoided crossing is smaller than the width of the modes as shown in Fig. 30(a). This is considered a weak coupling of the modes. In the reflectance from this system, the PMIMI line appears as a SPR-like resonance on a MIM background, shown in Fig.30(b). As the thickness decreases further, and thus the separation of the modes becomes greater than the line widths, we enter the strong coupling regime. This is shown in Fig. 30(a) for our baseline parameters of a coupling film thickness of 70 nm. As we have seen previously, this exhibits a clear Fano resonance as seen in Fig. 30(b). For smaller thicknesses of the coupling film, the MIM mode and SPP mode are no longer properly supported in the film, so they can no longer be thought of as a hybridization between the MIM and SPP modes. For a thickness of 20 nm,
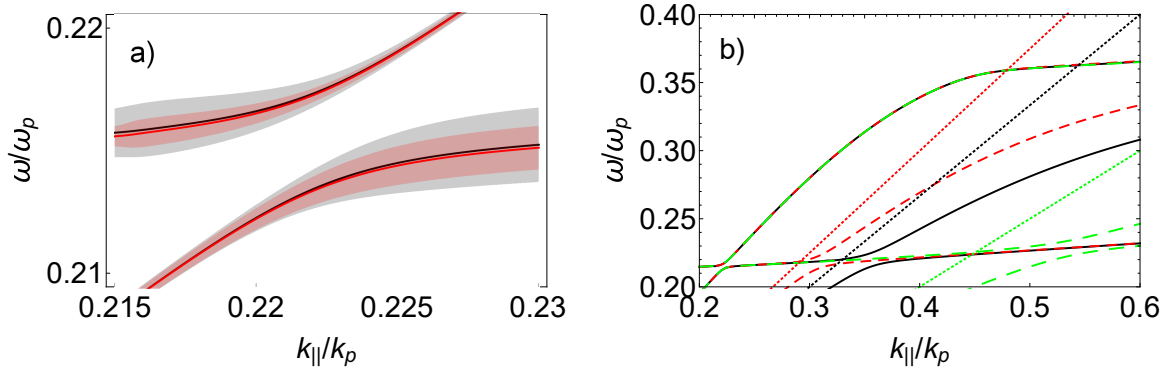
54

FIGURE 31. Prism permittivity and input film thickness variations - mode plots **a)** Mode diagrams for the PMIMI system for two different input metal thicknesses: 100 nm (black) and 65 nm (red). The decrease in metal thickness decreases line width as the modes become more leaky. **b)** Mode diagrams for three different prism permittivities: 1.78 (red dashed), 2.25 (black) and 4 (green dashed). The light lines for each permittivity is given by the dotted line of the same color. In all cases shown the vacuum SPP and MIM mode coupling region is unaffected.

no modes exist in the range shown in Fig. 30(a), and the reflectance of the system no longer shows any resonance as it is primarily reflected from the metallic film, with small amounts of transmission below the critical thickness, as shown in Fig. 30(b).

The coupling film gives direct control over the coupling strength via the spatial overlap of the fields of the MIM and SPP modes. With this we are able to explore different coupling regimes and focus on their aspects. Next we discuss the final parameters of the system, the input metal layer and prism permittivity, which affect the input light.

Input Metal Film Thickness and Prism Permittivity

When looking at the modes of the system, the primary effect of the input metal film thickness, t_i, is determining the mode width. For large thickness, such as $t_i = 100$ nm, the fields are well confined from the prism. As the thickness decreases, the modes become leaky and can lose energy to emission into the prism. This results
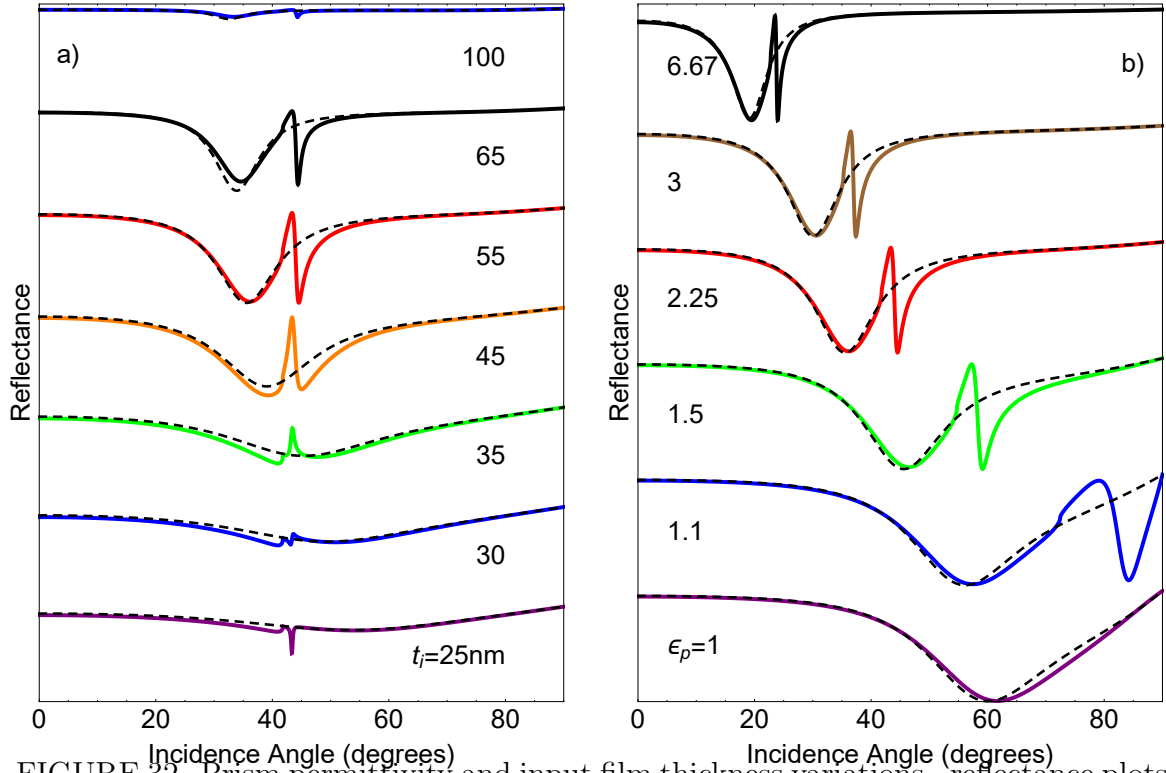
FIGURE 32. Prism permittivity and input film thickness variations - reflectance plots **a)** Reflectance from the PMIMI (solid) and semi-infinite MIM (dashed) systems for different input metal film thicknesses. For lower thicknesses the MIM resonance location shifts, resulting in different asymmetries of the GFR. As the thickness increases beyond 65 nm, the GFR becomes screened by the large thickness of the input film. **b)** Reflectance from the PMIMI (solid) and semi-infinite MIM (dashed) systems for different prism permittivities. For permittivities sufficiently large enough, the GFR is observed. As the permittivity is further increased, the resonance narrows and shifts to lower angles.

in a narrowing of the resonance, as shown in Fig. 31(a) with $t_i = 65$ nm. Once the

thickness starts to decrease below this, the MIM mode becomes unsupported and the

system is not adequately described by the hybridization of the MIM and SPP mode,

as mentioned for the coupling metal film for small thicknesses. This can be observed

in Fig. 32(a), where the dashed lines are the resonances for the same input metal

film, but a semi-infinite thickness for the coupling metal film. The line shape does

not resemble a MIM resonance, and the minimum location moves drastically, but for

these minima, a q-reversal is still observed. At the thickness of 100 nm, most of the energy is reflected, with little making it into the system, resulting in weak resonances.

For the prism permittivity, ϵ_p, we first discuss the modes of the system. As mentioned previously, the addition of the prism adds a second avoided crossing for the PMIMI modes. This occurs along the same MIM mode, but at higher wave vector than for the vacuum interface. As we change the prism permittivity, the prism interface avoided crossing moves along with the new light lines in the prism as shown in Fig. 31(b) for three different prism permittivities: water, $\epsilon_p = 1.78$; silica, $\epsilon_p = 2.25$; and $\epsilon_p = 4$, a non realistic permittivity used to show effects of higher permittivities in the wave vector range plotted. In all cases the lines overlap for the avoided crossing of the MIM and vacuum SPP modes, meaning that the prism permittivity does not change the properties of those coupled modes.

While the interactions of the MIM and vacuum SPP modes are unaffected, by a change in the permittivity the reflectance is modified. As the prism's permittivity in increased, the momentum of light in the prism increases. This allows for a large range of wave vectors for the angular range of 0° to 90°, and this results in a decrease of the resonance width and an overall shift of the resonance to lower angles. This is shown for several values of the permittivity in Fig. 32(b). It is important to note that the asymmetry of the resonance does not change as the non interacting modes are unaffected. The exception is for permittivities approaching 1. For these values, the SPP modes are still inaccessible, as one would expect.

So far we have focused on how the resonance changes in the angular domain as the material parameters are varied. For comparison to experiment and sensitivity measurements, it is important to see how the resonance looks as a function of the permittivity, which we explore next.
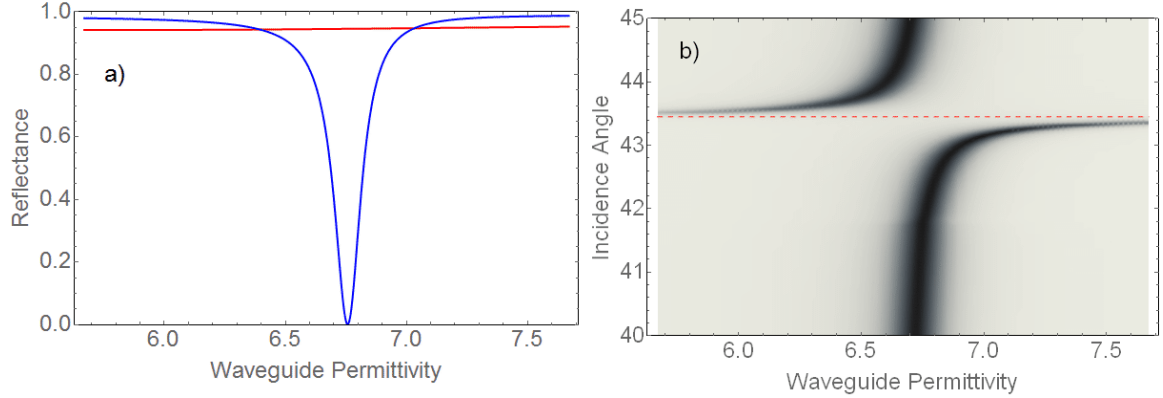
FIGURE 33. PMIMI reflectance vs. waveguide permittivity
a) Reflectance from the PMIMI (red) and semi-infinite MIM (blue) as the waveguide permittivity is varied. The PMIMI shows a distinct absence of a resonance due to destructive interference with the SPR mode. **b)** Reflectance from the PMIMI for variations of the angle and waveguide permittivity. The intensity is given by the grey scale with black being zero and white being 1. The horizontal red dashed line represents the SPR angle used in a. The MIM resonance splits and vanishes upon approaching the SPR angle.

Reflectance vs. Insulator Permittivities

So far we have only looked at the GFR as the angle is varied, but we can also evaluate the reflectance line shapes as the insulator permittivities are varied. In doing so, we hope to observe the sensitivity of the system to variations of the permittivities, and knowing these sensitivities can be informative for certain applications such as chemical or bio-sensing applications, as have been done for plasmonic sensors. A quantitative analsis of sensitivities are done in chapter VII, but we start with a qualitative discussion.

Reflectance vs. Waveguide Permittivity

We begin with varying the waveguide insulator film permittivity. In Fig. 33(a) we plot the reflectance of the PMIMI system and the MIM waveguide reflectance at the SPR angle: 43.45^o. The PMIMI line is devoid of any resonance, whereas the

MIM line shows the clear resonance at $\epsilon = 6.67$. The PMIMI line is flat because the surface plasmon mode and the MIM mode always interfere destructively at the SPR angle, resulting in a maximal output intensity. This is shown in Fig. 33(b), in which the reflected intensity is show as a function of both the incidence angle and the waveguide permittivity. We see that far detuned from the SPR angle, such as at 40°, the MIM resonance is clearly observable, but as we approach the SPR angle, the resonance is driven away from the MIM resonance permittivity and becomes the maximal output at the SPR angle due to the destructive interference. Unfortunately, this eliminates the waveguide layer for use as a permittivity sensor, and as such we keep the waveguide permittivity as TiO_2 for the remainder of this dissertation.

Reflectance vs. Exterior Permittivity

We can also vary the permittivity of the exterior layer, analogous to standard SPR sensing. First we examine the reflectance while varying the incidence angle and exterior permittivity for the baseline physical parameters. In this case, the MIM resonance, which does not depend on the exterior permittivity, is observed as the horizontal minimum at about 35° in Fig. 34(a). A second resonance appears at higher angles for higher permittivities, as one would expect from SPRs. Fig. 34(a) has three horizontal dashed red lines, corresponding to three different bench marked angles of incidence: 43.45^o (SPR angle), 48° and 65° and the PMIMI reflectance for each are plotted in Fig. 34 (b), (c) and (d), respectively. Also included in the figures are the SPR and MIM line for each angle. The MIM reflectance is a horizontal line because it does not depend on the exterior permittivity at all, only the incidence angle, as expected. The SPR shifts to higher permittivities for higher angles. In each of these plots a Fano resonance is observed in the PMIMI line, albeit cut off at $\epsilon = 1$
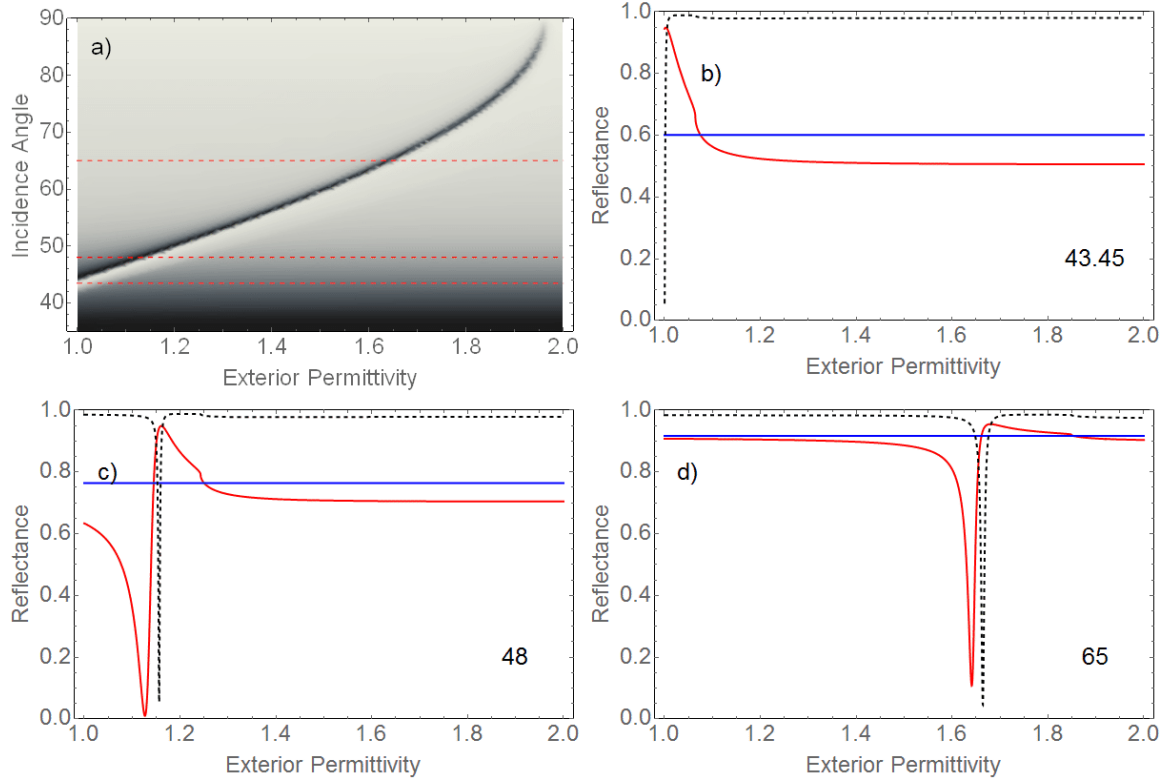
FIGURE 34. PMIMI reflectance vs. exterior permittivity with baseline parameters
a) Reflectance from the PMIMI for variations of the angle and exterior permittivity
for the baseline parameters. The intensity is given by the grey scale with black being
zero and white being 1. The horizontal red dashed lines represents three different
angles: **b)** 43.45^o, **c)** 48°, and **d)** 65°. In (b), (c) and (d) the PMIMI (red), SPR
(black dashed) and MIM (blue) are plotted.

in Fig. 34(b). For the SPR angle, the Fano resonance is cut off at $\epsilon = 1$, but the GFR

becomes apparent as the angle is further increased for Fig. 34 (b) and (c). In these

three plots, we do not observe the q-reversal, as we have seen in the past, because

the two resonance did not cross one another in our baseline parameter set.

In Fig. 35, we increase the waveguide thickness to 82.5 nm to move the MIM

resonant angle to approximately 60°. The density plot in Fig. 35(a) now shows an

avoided crossing of the SPR and MIM resonance. Fig. 35(a) has three horizontal

dashed red lines, corresponding to three different angles of incidence: 50°, 60° and 70°,
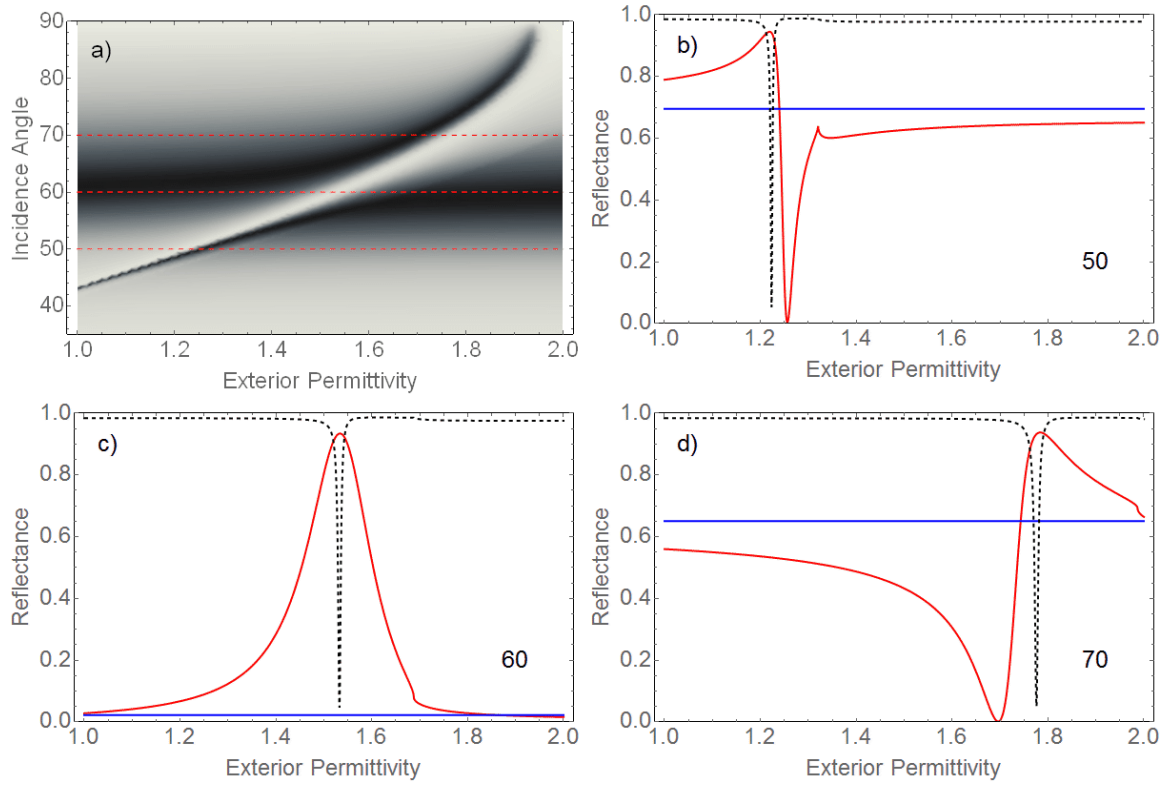
FIGURE 35. PMIMI reflectance vs. exterior permittivity with waveguide thickness increased

a) Reflectance from the PMIMI for variations of the angle and exterior permittivity where the waveguide thickness has been increased to 82.5 nm. The intensity is given by the grey scale with black being zero and white being 1. The horizontal red dashed lines represents three different angles: **b)** 50°, **c)** 60°, and **d)** 70°. In (b), (c) and (d) the PMIMI (red), SPR (black dashed) and MIM (blue) are plotted.

and the PMIMI reflectance for each are plotted in Fig. 35 (b), (c) and (d), respectively. Now that the SPR angle is swept through the MIM resonance, q-reversal is observed in the three plots. In comparing Fig. 35 (b) and (d), there is a clear reversal in the asymmetry of the lines. Fig. 35(c) shows the PIT when the MIM resonance is near its minimum.
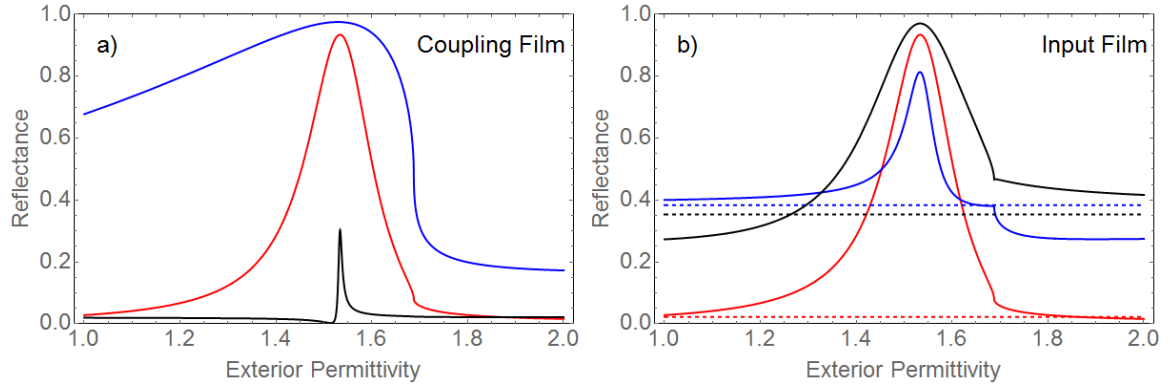
61

FIGURE 36. PMIMI reflectance vs. exterior permittivity with metal film variations **a)** Reflectance from the PMIMI for varying the exterior permittivity for different coupling film thicknesses. The thicknesses are 50 nm (blue), 70 nm (red) and 90 nm (black). **b)** Reflectance from the PMIMI for varying the exterior permittivity for different input film thicknesses. The thicknesses are 40 nm (blue), 55 nm (red) and 70 nm (black)

Conclusion

Now that we know that the GFR is observable as the exterior permittivity is varied, this allows us to use our knowledge of the PMIMI system to discuss the effects of the resonance. We have already shown that the location of the waveguide resonance can be adjusted via the waveguide permittivity and thickness. This allows us to set the GFR to a desired exterior permittivity and with a given asymmetry. We also know that we can adjust the coupling and therefor shape the resonances via the coupling metal film thickness, as shown in Fig. 36(a). We have plotted the GFR for three different coupling film thicknesses: 50 nm, 70 nm, and 90 nm. The thinner coupling film allows for greater overlap of the fields and exhibits a broadening of the line width. The thicker coupling film narrows the line width as the expense of peak intensity. It can also be observed that the asymmetry is reversed in the process as the PMIMI mode locations are slightly modified by the coupling film thickness, in addition to the mode widths. For the input metal film, varying the thickness from 55

nm changes the MIM resonance minimum from the relative zero value. This causes a decrease in the amplitude of the GFR. Additionally, the more (less) metal there is, the line width broadens (narrow) as the losses from the metal film are increased (decreased). These effects are shown in Fig. 36(b). As was seen previously, changes to the prism permittivity will adjust the GFR to a different angle and narrow the resonance for increased permittivity.

We showed that in the angular domain, we are able to set the location and shape the GFR while varying the exterior permittivity. As we explore later, this can be used to optimize the sensitivity of the PMIMI system, but before we discuss that, we first examine the phase of the PMIMI system in the next chapter, enabling us to discuss both the intensity and phase sensitivities at the same time.

CHAPTER VI

PHASE OF MULTILAYER SYSTEMS

So far we have extensively covered the intensity of the reflected field, so all that is left is to discuss the phase of the reflected field. It is a well known fact that phase based measurements are more sensitive to small changes in the system. This is why many measurements are made using interferometers, including recent advances in plasmonic sensing[123–128]. The large change in phase of the SPR allows for great interference sensitivity and has lowered the limit of refractive index sensing[23]. However, this is not without its own set of challenges. One of these issues is that phase based SPR creates low intensity output fields on resonance where the greatest change in phase occurs. But EIT and its analogs have greatly increased intensity in a region of steep change in phase[80]. We explore the GFR to observe this change in phase in a region of high intensity. In this chapter we discuss the phase of the SPR, MIM resonance and PMIMI GFR. Understanding the SPR and MIM phase behavior helps guide understanding of the PMIMI phase. Additionally, this allows for comparison of the relative phase changes of the systems.

SPR Phase

We begin by examining the phase behavior of the SPR. Still considering the Kretschmann configuration with a fused silica prism and light of the HeNe wavelength, we have three parameters that can be varied to change the phase behavior: metal film thickness, exterior permittivity and angle of incidence. As done previously, we first start by observing the fields as the angle is varied for several metal film thicknesses and exterior permittivities. In Fig. 37(a), the polar plots of the fields are shown for two
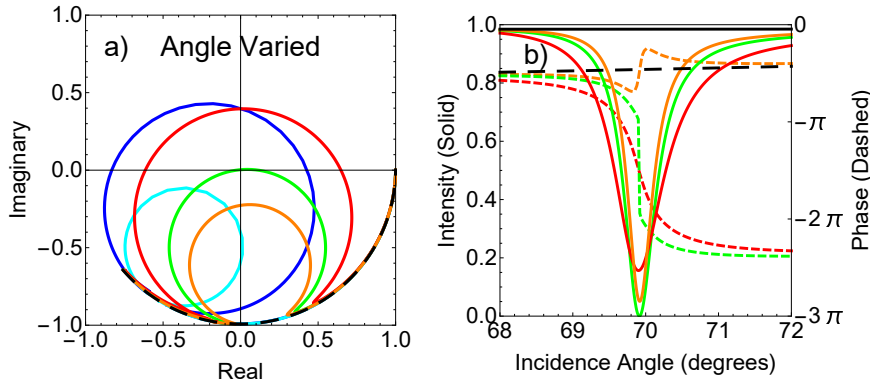
FIGURE 37. Surface plasmon resonance phase in angular domain
Field plots and reflected intensity and phase for the SPR in the Kretschmann configuration. **a)** Polar plot of the reflected field as a function of angle for the following parameter sets: $\epsilon_{ext.} = 1$ with $t_{metal} = 55$ nm (blue) and $t_{metal} = 70$ nm (cyan), and $\epsilon_{ext.} = 1.774$ with $t_{metal} = 55$ nm (red), $t_{metal} = 64.6$ nm (green) and $t_{metal} = 70$ nm (orange). Reflected field from a semi-infinite thickness metal layer is shown as the black dashed line. **b)** Reflected intensity and phase as a function of angle for water for three thicknesses: 55 nm (red), 64.6 nm (green) and 70 nm (orange).

different exterior permittivities: water and vacuum. Additionally, several thicknesses are chosen: 55 nm and 70 nm for each permittivity and a thickness of 64.5 nm is used for water. Also plotted is the reflected field from a semi-infinite thickness metal, shown as the dashed black line. For the same thickness the difference between the two fields is the location of the resonance, as would be expected. When we vary the metal layer thickness however, an interesting feature is noted. For smaller thicknesses, the loop in the field encompasses the origin, while for larger thicknesses it does not. The phase of the larger thickness is nonmonotonic and oscillate about the metal background phase, as shown in Fig. 37(b). Also shown in Fig. 37(b), the smaller thicknesses have a monotonic change in phase that circles the origin, and eventually undergoes a 2π phase shift to end up back in phase with the metal background. There is a critical thickness in which the resonance loop crosses the origin. For the water permittivity and the silver-like Drude metal, this occurs just above 64.6 nm. At the critical thickness, the intensity goes to zero and the phase undergoes a π phase shift
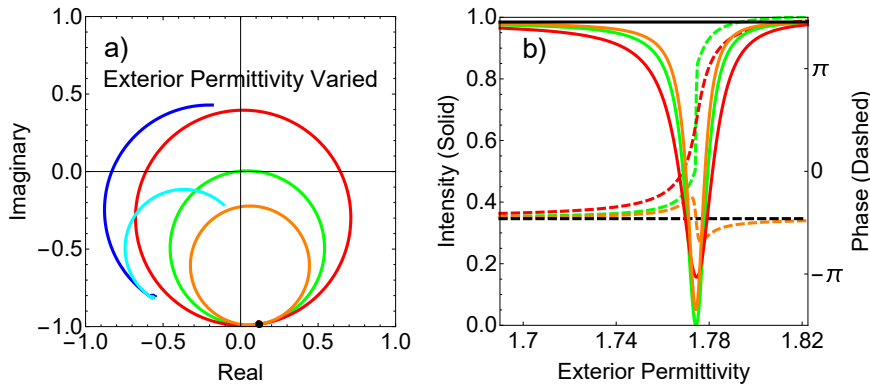
FIGURE 38. Surface plasmon resonance with varying exterior permittivity Field plots and reflected intensity and phase for the SPR in the Kretschmann configuration. **a)** Polar plot of the reflected field as a function of exterior permittivity for the following parameter sets: $\theta = 43.5^o$ with $t_{metal} = 55$ nm (blue) and $t_{metal} = 70$ nm (cyan), and $\theta = 69.9^p$ with $t_{metal} = 55$ nm (red), $t_{metal} = 64.6$ nm (green) and $t_{metal} = 70$ nm (orange). Reflected field from a semi-infinite thickness metal layer is shown as the black dot. **b)** Reflected intensity and phase as a function of permittivity for $\theta = 69.9^o$ for three thicknesses: 55 nm (red), 64.6 (green) and 70 nm (orange). Reflected intensity and phase from a semi-infinite thickness metal layer is shown as black.

jump at the resonance. In experiment, this exact critical thickness would not be achievable due to finite lattice spacing and surface roughness, but is important to understand the effects of being above or below the critical thickness.

We also investigate the reflected field as the exterior permittivity is varied. In this case, a fixed angle is chosen and then the permittivity is varied from 1 to 2. In Fig. 38(a) we plot the fields in the polar domain for two different angles: 43.5^o and 69.9^o; angles near the SPR angle for vacuum and water, respectively. Also included is the reflected field from a semi-infinite metal layer for an angle of 69.9^o, as the black dot. As there is no exterior permittivity in this case, the intensity and phase are constant for the semi-infinite metal. When looking at the water-like traces, all three thicknesses have a loop that starts and ends at the metal background phase. This is the same behavior as seen in the angular domain with one exception: the loops occur
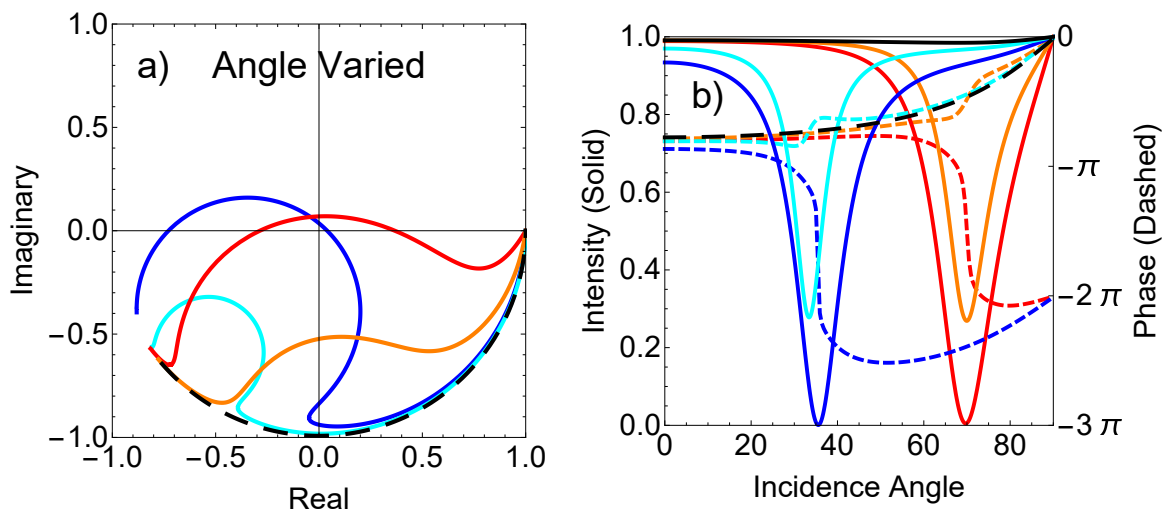
FIGURE 39. MIM phase

Field plots and Reflectance for the semi-infinite MIM resonance. **a)** Polar plot of the reflected field as a function of angle for the following parameter sets: $t_{TiO_2} = 80$ nm with $t_{metal} = 55$ nm (blue) and $t_{metal} = 70$ nm (cyan), and $t_{TiO_2} = 83.5$ nm with $t_{metal} = 55$ nm (red) and $t_{metal} = 70$ nm (orange). Reflected field from a semi-infinite thickness metal layer is shown as the black dashed line. **b)** Reflected intensity and phase as a function of angle with colors corresponding to the parameter traces in (a).

in the opposite direction. This can be observed in Fig. 38(b) as the phase shifts in the positive direction instead of the negative. For the vacuum-like traces, the loop is incomplete becauase the resonance is cut off at $\epsilon = 1$. The potential use for sensing at $\epsilon = 1$ is important, but to allow full observation of the resonances, we later focus on changes to the system about the permittivity of water, $\epsilon = 1.774$.

MIM Phase

We now discuss the phase of the MIM resonance. As a reminder, to observe this resonance, we need have a finite metal film and a TiO_2 waveguide film, with a semi-infinite fused silica cladding adjacent to the metal film and a semi-infinite metal cladding adjacent to the TiO_2 film. Light with the HeNe frequency is incident from the fused silica layer at varying angles. We keep the waveguide layer as TiO_2, which

allows for two variable parameters: metal and waveguide film thicknesses. As shown previously, the waveguide film thickness changes the relative location of the resonance, as seen in Fig. 39(b). Changing the thickness to 83.5 nm brings the MIM resonance angle to 70°, which is near the SPR angle for water. In this case, the angular range in which the resonance occurs no longer makes the resonance appear to be a near circular loop. The background phase of the semi-infinite As such, the phase change of the resonance is less than the 2π seen for the SPR but still more than π. The MIM resonance returns to the semi-infinite metal reflection detuned from the resonance, as expected Varying the metal film thickness has the same effect seen for the SPR; the loop decreases in size for increased metal film thickness. When observing the phase, the same trends are seen: below the critical thickness, the phase is monotonic and above the critical thickness the phase oscillates. The metal film thickness of 55 nm used is just below the critical thickness for the MIM resonance and gives a steep angular shift on resonance.

This resonance is independent of the exterior permittivity and the SPR. As we will see in the PMIMI, the MIM acts similarly to the semi-infinite metal background for the SPR. For a given angle, the MIM resonance sets an intensity and a phase that the SPR is coupled to and modify. This is shown later in this chapter.

PMIMI Geometric Fano Resonance Phase in the Angular Domain

For the PMIMI system the number of variable parameters increases greatly. We keep the fused silica prism, silver-like Drude metal and TiO_2 waveguide permittivities fixed, as well as the input HeNe light. This still allows for variations of the three film thicknesses, the angle of incidence and the exterior permittivity. As before, we first explore the angular domain, while varying the other parameters. This is done in a

step-by-step process varying one parameter at a time. We start with the baseline parameters of $t_i = 55$ nm, $t_g = 80$ nm, $t_c = 70$ nm and the exterior permittivity is vacuum. First, we adjust the waveguide thickness, t_g, to adjust to a PIT. Second, we vary the input metal thickness, t_i, to observe changes in the resonance loop size and phase. Finally, the coupling metal thickness, t_c, is then varied to observe changes of the resonance loop and phase. Then we discuss the variations to the exterior permittivity.

We begin with the baseline parameters used throughout this dissertation in Fig. 40(a) and (b)[1]. When comparing the PMIMI and MIM trace, there is a large deviation below the critical angle for TIR. This is seen as the kink just after the grey marker dot. This deviation actually causes the nature of the MIM resonance to change its behavior and not encompass the origin, causing the PMIMI plot to oscillate and not be monotonic. In this case we see that there are two loops associated with the PMIMI GFR, the first is associated with the MIM and within that semi-circular loop a second loop occurs from the SPR. Both loops do not contain the origin, causing the phase to oscillate twice, once at each minimum in the PMIMI reflectance. Due to the rapid phase change of the SPR caused loop, there is a change in phase in the region of high intensity, as shown in Fig. 40(b) at about 43°-44°. This enhanced phase change in a region of high intensity has the phase signature that we are looking for, and now we move onto variations to maximize this

We next adjust the waveguide thickness to achieve a PIT. In Fig. 40(c) and (d), we plot the field plots with the waveguide thickness increased to 80.5 nm. This creates a PIT as seen in Fig. 40(d), and we see the change in phase inside the window of transparency looks promising, though it should be noted that the change of phase is

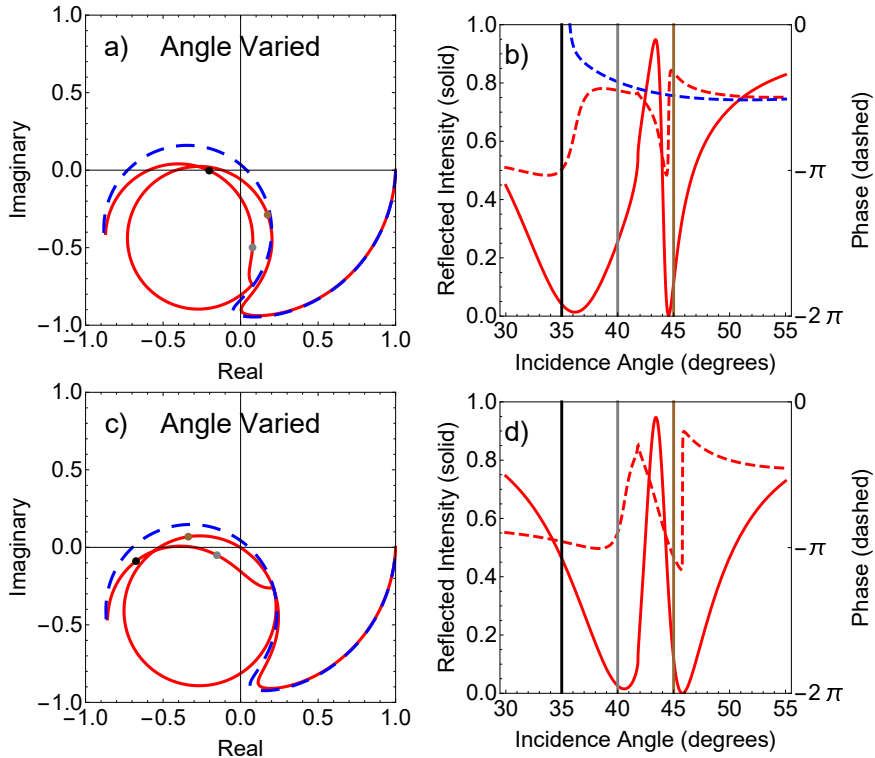[1]It should be noted that this uses the same parameters as Fig. 23.

FIGURE 40. PMIMI phase with baseline parameters and PIT

Field plots and reflected intensity and phase for the PMIMI GFR. **a)** Polar plot of the reflected field as a function of angle for the PMIMI with $t_i = 55$ nm, $t_g = 80$ nm, and $t_c = 70$ nm (red). Also included is the semi-infinite MIM (dashed blue). The black, gray and brown dots on the PMIMI trace correspond to 35°, 40° and 45°, respectively, showing a clockwise path of the curve. **b)** Reflected intensity and phase for the PMIMI GFR and the phase of the MIM resonance. The vertical lines correspond to the same colored dots in (a). **c)** Polar plot of the reflected field as a function of angle for the PMIMI with $t_i = 55$ nm, $t_g = 80.5$ nm, and $t_c = 70$ nm (red). Also included is the semi-infinite MIM (dashed blue). The black, gray and brown dots on the PMIMI trace correspond to 35°, 40° and 45°, respectively, showing a clockwise path. **d)** Reflected intensity and phase for the PMIMI GFR and the phase of the MIM resonance. The vertical lines correspond to the same colored dots in (c).

just less than π over a range of 5°.[2] We have lost phase sensitivity to gain intensity in this system. This is explored quantitatively in chapter VII. Before that though, we

---

[2]In comparison to the phase of the SPR from Fig. 37(b), which is larger than π over a range of less than 1 degree.
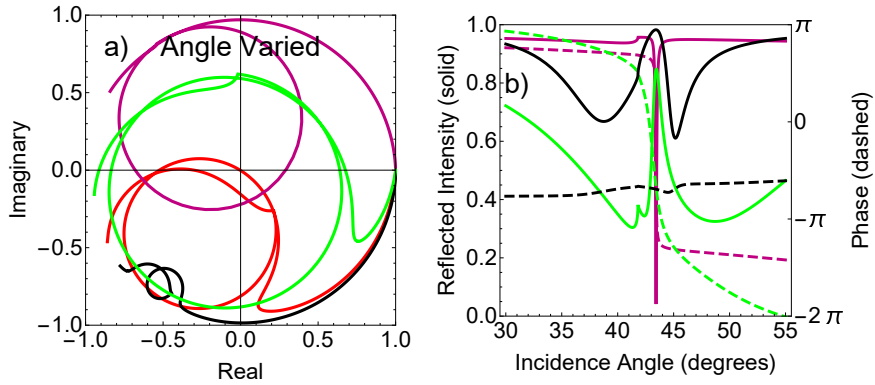
FIGURE 41. PMIMI phase with input metal film varied
a) Polar plots of the fields for the PMIMI GFR with four different input film thicknesses: 10 nm (purple), 40 nm (green), 55 nm (red) and 80 nm (black). **b)** Reflectance and phase for the corresponding colors of thicknesses in (a).

still need to learn how the metal layers of the system are going to affect the PMIMI system.

We now explore changes to the input metal film. If we increase the input metal film thickness, the MIM loop shrinks. The SPR loop is contained within the MIM loop and also decreases in size until the entire trace approaches the reflectance of a semi-infinite metal layer, as shown in Fig. 41(a) and (b). As would be expected from screening input energy from the system, the resonance minimums are greatly reduced, though the general GFR shape is still observed. As noted before, changing the input metal thickness shifts the MIM resonance location, and the GFR appears as the more general Fano lineshape and not the PIT. Additionally, the changes in phase are greatly decreased as less of the field interacts with the system. As such, higher input thicknesses does not exhibit the greatest sensitivity of the system. If we instead decrease the input metal film thickness, such as to 40 nm, we increase the MIM loop to encompass the origin. When this happens, the SPR loop contains the origin, and undergoes a phase change of greater than 3π over the entire resonance. In the 2 degree region of the transparency, we get the 2π phase shift expected from the
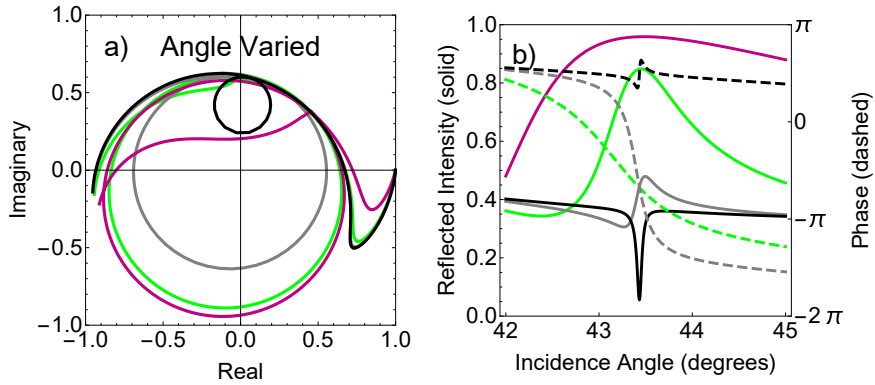
71

FIGURE 42. PMIMI phase with coupling metal film varied
a) Polar plots of the fields for the PMIMI GFR with four different coupling film thicknesses: 50 nm (purple), 70 nm (green), 90 nm (gray) and 120 nm (black). Here $t_i = 40$ nm matching green traces in Fig. 41. **b)** Reflectance and phase for the corresponding colors of thicknesses in (c). Note the change in angular range.

additional loop. If the thickness gets too low, the MIM mode cannot be supported and the lineshape approaches that of a standard SPR. This shows that the SPR still has a steeper phase slope than the GFR, but the increase in intensity may have merit when it comes to phase detection.

The next film varied is the coupling metal film, which the film thickness affects the coupling between the modes. For observation of additional effects, we set the input metal film thickness to 40 nm. In the polar plots, this is exhibited by the changing size of the SPR loop shown in Fig. 42(a). As the loop size decreases the change in phase increases rapidly and the resonance narrows, as seen in Fig. 42(b). Again, the large coupling metal film causes the resonance to become more SPR-like as the field overlap between the modes decreases. At a thickness of 120 nm, the PMIMI phase line shape looks more akin to the SPR phase oscillating about the MIM phase. Increasing the thickness further, the loop no longer encompasses the origin and oscillates about the MIM phase.
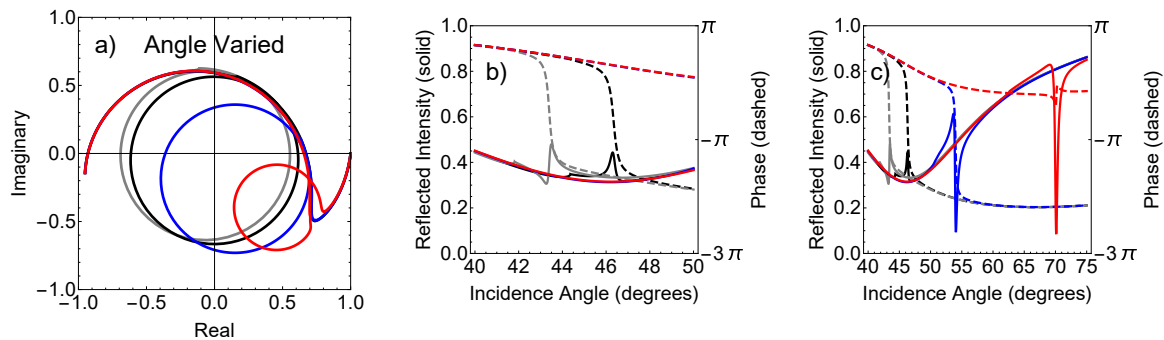
FIGURE 43. PMIMI phase with exterior permittivity variation
Field, intensity and phase for the PMIMI GFR with with different exterior permittivities: $\epsilon_e = 1$ (gray), $\epsilon_e = 1.1$ (black), $\epsilon_e = 1.35$ (blue) and $\epsilon_e = 1.774$ (red). Here $t_i = 40$ nm, $t_g = 80.5$ nm and $t_c = 90$ nm. **a)** Polar plots of the fields. **b)** Reflectance and phase near waveguide minimum. **c)** Reflectance and phase in expanded angular range.

We have shown that both decreasing the input metal thickness and increasing the coupling film thickness improve the slope of the phase in the angular domain. In both cases, this begins to approach a resonance that begins to resemble the SPR, with the exception of the PIT. We explore the sensitivity of the phase quantitatively in the chapter VII.

To complete the set, we finish with a change in the exterior permittivity, ϵ_e. In Fig. 43 we plot the fields for four different permittivities. For small changes to the permittivity such as 1 to 1.1, the phase is relatively unaffected by the change. We can see that the intensity undergoes a q-reversal in Fig. 43, though this has little effect on the phase slope. For large variations of the exterior permittivity, the phase can transition through the origin and start to oscillate instead of behaving monotonically. This is similar to what we observed before in the limit of weak coupling between the MIM and SPR and the resonance again appears to become more like two independent resonances. As was discussed previously, if we want to have a GFR at

a different exterior permittivity, we can adjust our waveguide thickness to place the MIM resonance near the SPR angle.

In the next section we examine the phase behavior as a function of the exterior permittivity. We adjust the waveguide thickness such that the MIM resonance angle is around the SPR angle for water (69.9^o). This is done so that the entirety of the GFR can be observed and is not cut off below $\epsilon = 1$.

PMIMI Geometric Fano Resonance Phase vs. the Exterior Permittivity

Now we examine the PMIMI resonance while varying the exterior permittivity. A waveguide film of thickness 83.5 nm is used to adjust the MIM resonance angle to the SPR angle as shown in Fig. 44(b), and in the angular variations of the fields in the polar plot, we see the expected loop within the MIM background. To explore the phase behavior, we pick three angles 65°, 69.9^o and 75° and plot the fields as the exterior permittivity is varied in Fig. 44(c) and see a similar effect to the loops observed in Fig. 38(a). The primary difference here is that the background is no longer the semi-infinite silver, but the MIM resonance. Each loop originates from the MIM field location shown as the dots on the plot, which are the same as the dots on the gray MIM fields in Fig. 44(a). While this is un-physical, to show the continuation of the field to the MIM background the permittivity was allows to go below one to mathematically show the limit of the background for the PMIMI resonance. On the other end, at higher indexes the GFR gets modified as there is no longer TIR and energy is lost to transmitted light. For the three different angles, we observe the q-reversal through a transparency as the angle is increased, as shown in Fig. 44(d), and is as expected. As for the phase, we also see that it undergoes a transition from monotonic to non-monotonic, but this transition does not occur at the transparency,
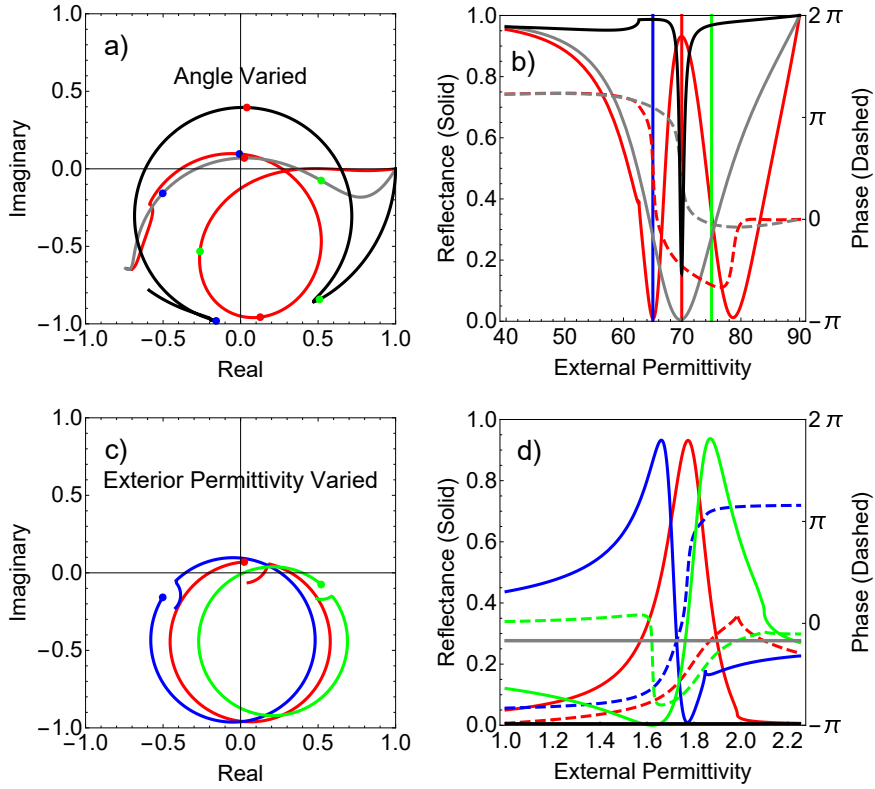
FIGURE 44. PMIMI phase vs. exterior permittivity

Field plots and reflected intensity and phase for the PMIMI GFR adjusted for maximal interference near the index of refraction for water. **a)** Polar plot of the reflected field as a function of angle for the PMIMI with $t_i = 55$ nm, $t_g = 83.5$ nm, and $t_c = 70$ nm (red). Also included is the semi-infinite MIM (gray) and the SPR (black). The blue, red and green dots on each trace correspond to 65°, 69.9^o and 75°, respectively. **b)** Reflected intensity and phase for the PMIMI GFR and MIM resonance and the SPR reflectance. The vertical lines correspond to the same colored dots in (a). **c)** Polar plot of the reflected field as a function of exterior permittivity for the PMIMI for three different angles: $\theta = 65^o$ (blue), $\theta = 69.9^o$ (red), and $\theta = 75^o$ (green). The blue, red and green dots on each trace correspond to the same dots on the gray MIM trace in (a). **d)** Reflected intensity and phase for the PMIMI for each angle corresponding to the colors in (c).

where q-reversal occurs. It occurs when the minimum of the Fano resonance reaches zero, which not occur during the transparency. As was observed in the angular domain, the steepness of the slopes is greater when approaching the minimum of the Fano resonance as compared to the transparency.
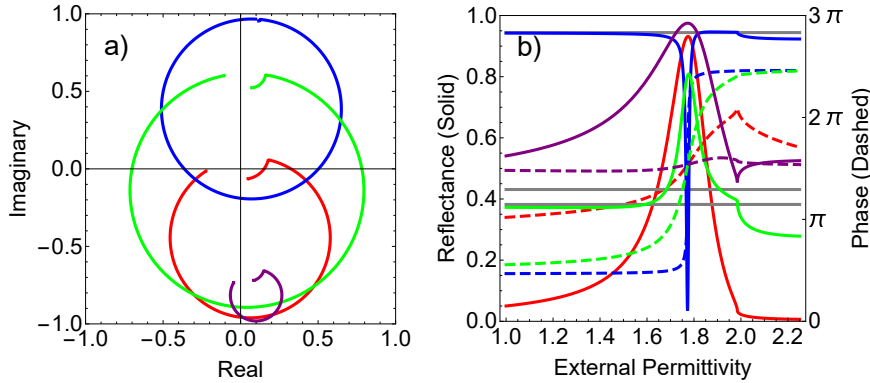
75

FIGURE 45. PMIMI phase vs. exterior permittivity with input metal film varied
a) Polar plots of the fields for the PMIMI GFR with four different input film thicknesses: 10 nm (blue), 40 nm (green), 55 nm (red) and 75 nm (purple). **b)** Reflectance and phase for the corresponding colors of thicknesses in (a).

As we move forward in exploring the parameters than can be varied, we know that angle and waveguide parameters primarily change the resonance location, so we focus on variations to the metal film thicknesses. We use our knowledge from the angular domain to guide us through the process.

We first begin by exploring the input film thickness. In Fig. 45(a) the fields are plotted as the exterior permittivity is varied for several different thicknesses. The same trends as Fig. 41(a) are observed: as the thickness increases from 10 nm to 75 nm the loops shift downwards, and seen to expand in size and then decrease. As the background MIM in this case does not change, the loops in Fig. 45(a) are much simpler than Fig. 41(a) in which the background also changes with angle. As we look at Fig. 45(b) for the phase, we see that the phase undergoes the expected monotonic change in phase for lower input metal film thicknesses, ignoring the change in behavior when TIR is not occurring. For greater thicknesses, the origin is not enclosed by the loop and the phase oscillates with small amplitude. Again this is the same as seen in the angular domain in Fig. 41(b).
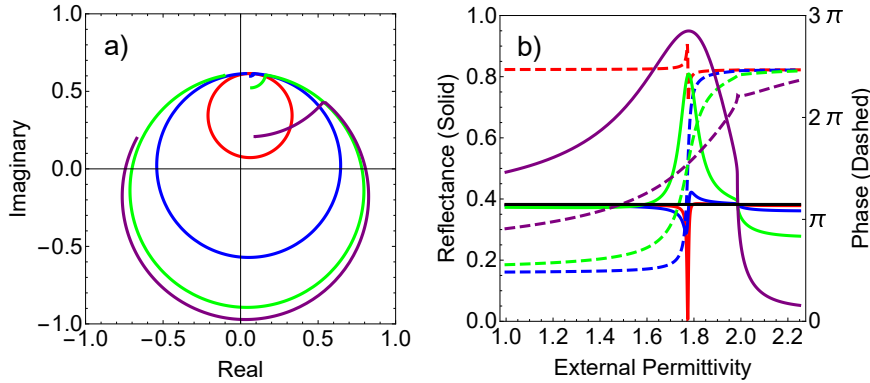
FIGURE 46. PMIMI phase vs. exterior permittivity with coupling metal film varied **a)** Polar plots of the fields for the PMIMI GFR with four different coupling film thicknesses: 50 nm (purple), 70 nm (green), 90 nm (blue) and 110 nm (red). Here $t_i = 40$ nm matching green traces in Fig. 45. **b)** Reflectance and phase for the corresponding colors of thicknesses in (c). Phase for 110 nm has been vertically shifted by 2π for visibility. Black horizontal line represents the semi-infinite MIM intensity.

Fig. 46(a) shows the fields as the coupling metal thickness is varied. For this plot we have selected the input metal thickness of 40 nm, such that our background value is neither non-zero nor near unity in intensity. Again we see that same trends as the angular domain, as the thickness is increased the loop shrinks in size. We also see that the PMIMI resonance follows the same trends here as in the angular domain in Fig. 46(b). The phase undergoes the transition from monotonic to non-monotonic as the thickness is increased. This transition occurs once again when the resonance minimum hits zero.

Unsurprisingly, we see the same exact trends in the exterior permittivity domain as we see in the angular domain. Decreasing the input metal thickness and increasing the coupling film thickness both improves the slope of the phase in the angular domain, except in extreme limits. We explore the sensitivity of the phase quantitatively in the following chapter.

CHAPTER VII

SENSITIVITIES OF MULTILAYER SYSTEMS

We are interested in the application of the PMIMI system as a sensor for detection of index changes. Our motivation comes the the already existing applications of surface plasmon resonance in the field of sensors as discussed in the introduction. There are different techniques for refractive index sensing: resonant angle shift, resonant frequency shift, intensity change, phase change and more. We focus on the change in intensity and phase for this dissertation and calculate the phase and intensity sensitivity. We use

$$S_R = \left| \frac{dR}{dn} \right| \tag{7.1}$$

$$S_\phi = \left| \frac{d\phi}{dn} \right| \tag{7.2}$$

for our definition of the sensitivity for the intensity and phase, respectively. We switched to the index of refraction to align with standard sensing nomenclature. The reflectance has been normalized, so S_R has units of inverse refractive index units (1/RIU), while S_ϕ has units of radians per RIU (rad/RIU). We also discuss the dynamic range and use the full-width at half max (FWHM) as a measure, which has units of refractive index units (RIU).

In addition to finding the sensitivities of the PMIMI system, we also calculate the sensitivities of the SPR system to directly compare sensitivities. As discussed previously, the change in phase is maximal when the resonance is at its minimum[1]. However, all the resonances with a zero intensity at resonance have an infinite phase slope. To be able to compare relative phase sensitivities, we select parameter

---

[1]For the transparency, there is an overall change in phase at the maximum.
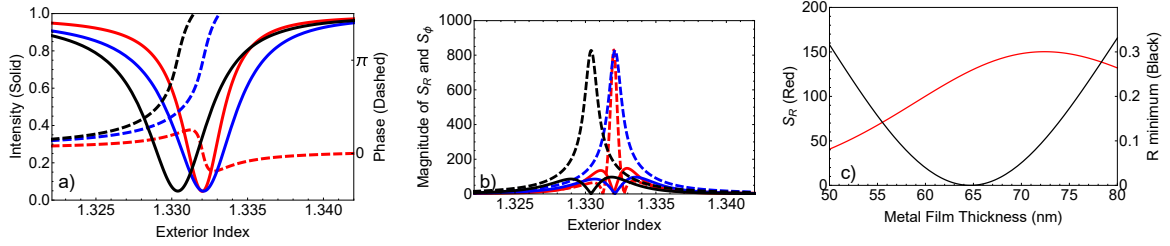
FIGURE 47. SPR sensitivity

a) SPR reflected intensity and phase for two metal film thicknesses: 59.8 nm (blue/black) and 69.8 nm (red). The red and black lines are at the SPR angle for water (69.92^o), while the black line has been adjusted to an angle of 69.7^o, for increased intensity sensitivity at $n = 1.332$. **b)** The magnitude of the sensitivities for the matching colors in (a). Note that the sensitivities for the two angles with a thickness of 59.8 nm have the same features. **c)** Intensity sensitivity and minimum intensity for each metal thickness.

values that give a minimum value of 0.05 for the normalized reflectance, and we can

extrapolate the increasing phase as the resonance minimum approaches zero.

Surface Plasmon Resonance

We explore the sensitivities of the SPR first, were the only tunable parameter is

the thickness of the metal film. The angle of incidence is chosen to be 69.92^o, the SPR

angle for water. The intensity and phase for the SPR are plotted in Fig. 47(a), for

one above and one below the critical thickness. Both exhibit the same magnitude of

sensitivity in phase at the resonance minimum in Fig. 47(b) of 830 rad/RIU. Above

the critical thickness, the line width is narrower resulting in an increased intensity

sensitivity (150 1/RIU) compared to below the critical thickness (100 1/RIU). The

narrower resonance decreases the dynamic range of the intensity, and the oscillatory

behavior of the phase decreases the dynamic range of the phase. While the resonant

location is slightly affected by the change in thickness, we do not re-adjust the angle

of incidence to maximize the sensitivity at $n = 1.332$. The change in the sensitivity
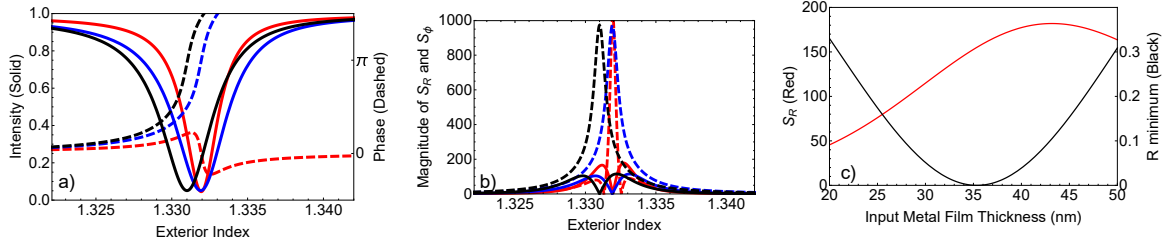
FIGURE 48. WCSPR sensitivity

PMIMI with $t_g = 115$ nm and $t_c = 40.8$ nm. **a)** Reflected intensity and phase for two input metal film thicknesses: 30 nm (blue/black) and 40.4 nm (red). The red and black lines are at $\theta = 69.00^o$), while the black line has been adjusted to $\theta = 68.89^o$, for increased intensity sensitivity at $n = 1.332$. **b)** The magnitude of the sensitivities for the matching colors in (a). Note that the sensitivities for the two angles with a thickness of 30 nm have the same features. **c)** Intensity sensitivity and minimum intensity for each metal thickness.

is minimal in comparison to the peak value of sensitivity for a small detuning of the angle of incidence, as shown in Fig. 47(b).

An interested feature is that the maximal intensity sensitivity does not occur at the critical thickness, shown in Fig. 47(c). The sensitivity is maximal nearly 10nm above the critical thickness. The decreasing resonance width increases the intensity sensitivity, which is countered by the decreasing depth of the resonance. Above the maximal sensitivity, the resonance depth becomes the dominate factor and sensitivity drops.

Waveguide coupled surface plasmon resonance - 115 nm waveguide

We first tune the parameters of our PMIMI stack to get the WCSPR, which has similar features to the SPR. In this case, $t_g = 115$ nm to shift the MIM resonant angle far from the SPR angle. The interactions between the two modes shifts the resonance location, an incidence angle of $\theta = 69.00^o$ results in the WCSPR at $n = 1.332$. The observed resonance of the WCSPR in Fig. 48(a) is similar to the SPR shown above and the same trends seen for the SPR are observed for the WCSPR. We can see
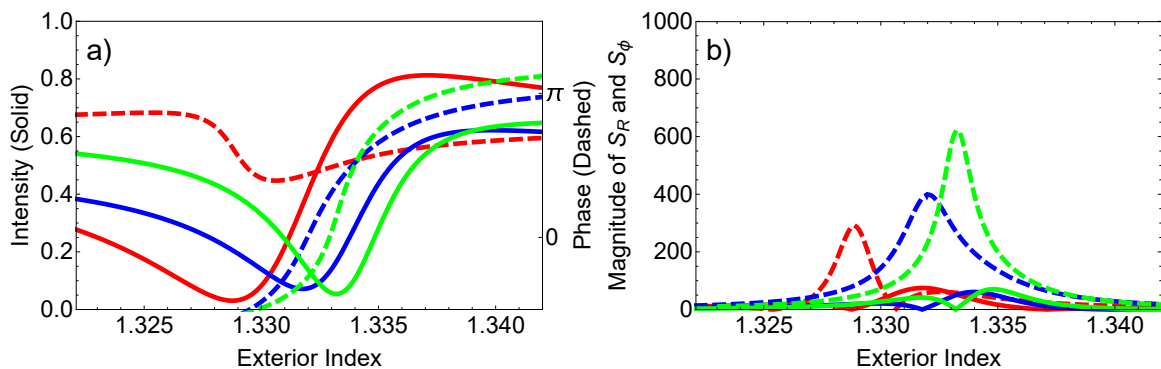
FIGURE 49. Fano sensitivity
PMIMI with $t_g = 82.5$ nm and $t_c = 90$ nm. **a)** Reflected intensity and phase for three input metal film thicknesses: 34 nm (green), 40 nm (blue) and 55 nm (red). All lines are at $\theta = 70.25^o$. **b)** The magnitude of the sensitivities for the matching colors in (a).

that the sensitivity of the WCSPR is greater than the SPR in Fig. 48(b). While the SPR had a maximal phase sensitivity of 850 rad/RIU and intensity sensitivity of 150 1/RIU, the WCSPR has 1000 rad/RIU and 180 1/RIU, respectively, showing a promising increase over SPR. The WCSPR sensitivity is also not affected by a small angular shift. Fig. 48(c) shows that the maximal intensity sensitivity does not occur a zero resonance, as expected from the SPR-like nature of the WCSPR.

Geometric Fano resonance - 82.8 nm waveguide

We now change t_g to 82.5nm, to observe the asymmetric Fano line shape in Fig. 49(a). As we decrease t_i, the asymmetry decreases as the minimum becomes the primary feature of the resonance. The changes in the asymmetry drastically change the location of the maximal sensitivities in comparison to the WCSPR, as seen in Fig. 49(b). For the asymmetric Fano line shape, the maximal phase sensitivity (290 rad/RIU) occurs at the minimum of the resonance, and the phase sensitivity in increased as t_i decreases, as expected. At $t_i = 34$ nm, the SPR-like resonance has a minimum intensity of 0.05, allowing for comparison to the SPR which has
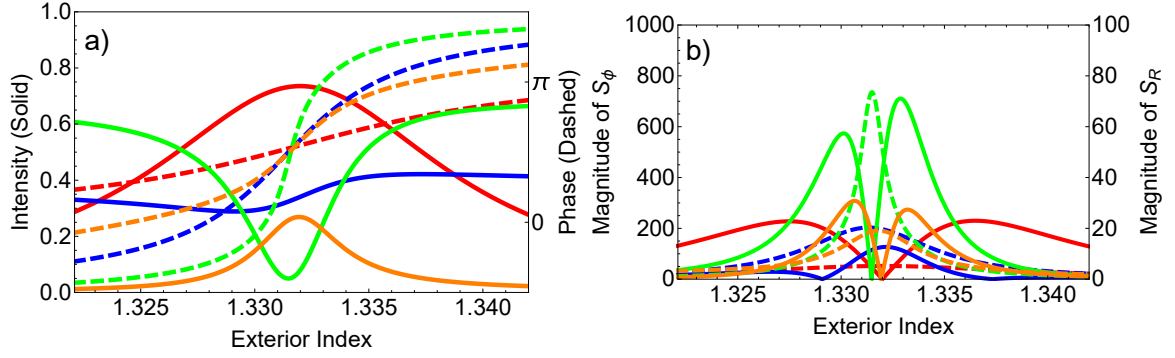
FIGURE 50. PIT sensitivity

PMIMI with $t_g = 83.5$. **a)** Reflected intensity and phase for different metal film thicknesses: $t_i = 55$ nm and $t_c = 90$ nm (red), $t_i = 40$ nm and $t_c = 90$ nm (blue), $t_i = 30.2$ nm and $t_c = 90$ nm (green), and $t_i = 55$ nm and $t_c = 110$ nm (orange). All lines are at $\theta = 69.92^o$. **b)** The magnitude of the sensitivities for the matching colors in (a). The intensity sensitivities have been magnified and the scale is shown on the right.

a value of 620 rad/RIU, less than the SPR sensitivity. The intensity sensitivity remains relatively unchanged about a value of 75 1/RIU. An observable increase in the dynamic range does occur when looking the the asymmetric Fano lineshape.

Plasmon induced transparency - 83.5nm waveguide

We now examine the PIT line shapes by having $t_g = 83.5$ nm. This adjusts the MIM resonance angle to the SPR, as such we again use $\theta = 69.92^o$. We observe the resonances for several different metal film thicknesses in Fig. 50(a). Discussed in the chapter VI, we can increase the phase sensitivity by either decreasing t_i or increasing t_c. As t_i is decreased, this causes the line shape to transition from a PIT to a SPR-like resonance. The PIT line width is broader than the SPR or WCSPR, this results in a decreased sensitivity in both intensity (25 1/RIU) and phase (50 rad/RIU), shown in Fig. 50(b). The dynamic range is greater than the SPR or WCSPR, due to the increase line width. When we try and compare the SPR-like resonance for this t_g, we
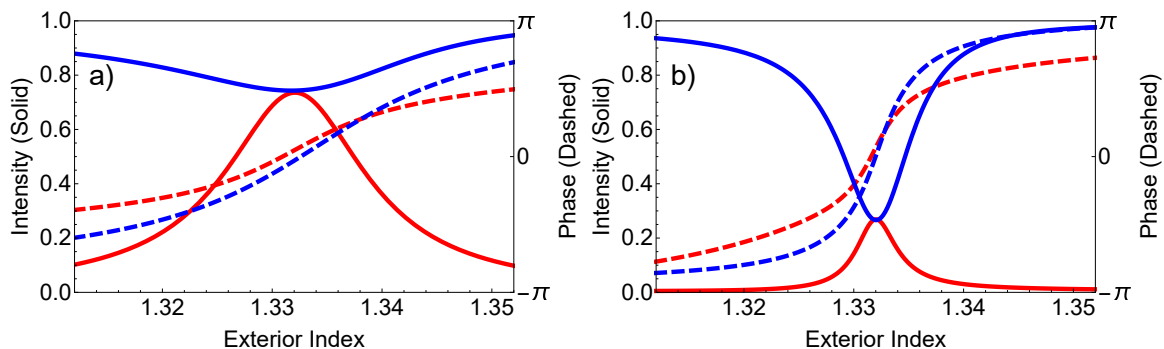
FIGURE 51. PIT and SPR comparison

PMIMI with $t_g = 83.5$. **a)** Reflected intensity and phase for different metal film thicknesses: $t_i = 55$ nm and $t_c = 90$ nm (red), $t_i = 40$ nm and $t_c = 90$ nm (blue), $t_i = 30.2$ nm and $t_c = 90$ nm (green), and $t_i = 55$ nm and $t_c = 110$ nm (orange). All lines are at $\theta = 69.92^o$). **b)** The magnitude of the sensitivities for the matching colors in (a). **c)** Intensity sensitivity and minimum intensity versus metal thickness. Kink happens at 40 nm as the sign of the sensitivity changes.

see a decrease in sensitivity compared to SPR ($S_R = 70$ 1/RIU and $S_\phi = 740$). This is expected from the lesser depth of this resonance compared to SPR.

Increasing t_c increases of the phase sensitivity at the expense of the transparency peak value, as shown in Fig. 50(a). This also decreases the line width, which increases intensity sensitivity and decreases dynamic range, shown in Fig. 50(b). An interesting comparison for the $t_c = 110$ nm PIT is the nearly flat Fano line shape ($t_i = 40$ nm and $t_c = 90$ nm for the same t_g) in Fig. 50(a). The PIT has a lower slope in phase and lower intensity than the nearly flat Fano resonance.

An initial motivation we had for this research was an increased output intensity with a great change in phase motivated by EIT and the large change in phase across the transparency. We compare the two PIT curves from Fig. 50 with two SPR with the same intensity minimum as the PIT maximum in Fig. 51. Note that in both cases, for the same intensity on resonance/transparency the SPR has a greater phase slope. In normal discussion of EIT, phase comparisons are made between the phase of the unmodified broad resonance and the phase of the EIT. In my review of the
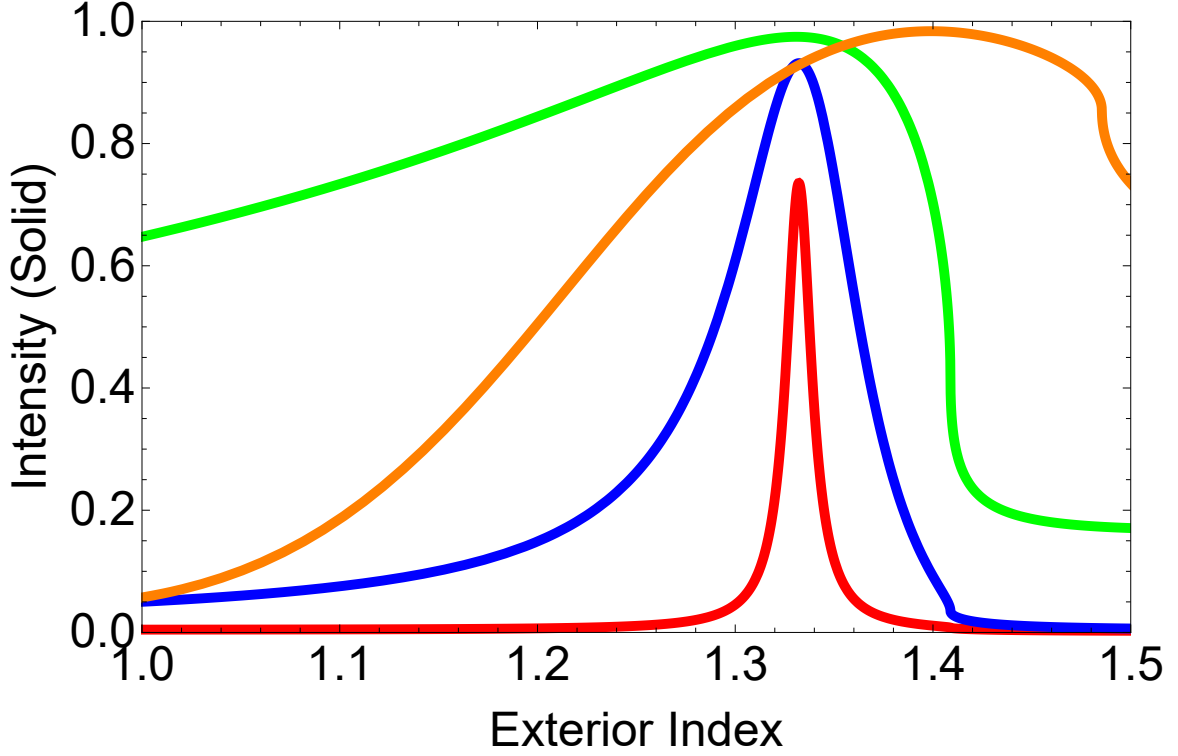
FIGURE 52. Increasing dynamic range

PMIMI with $t_i = 55$ nm, $t_g = 83.5$ and several values of t_c: 90 nm (red), 70 nm (blue), 50 nm (green/orange). All plots excluding orange are at $\theta = 69.92^o$, the orange curve is at $\theta = 82.0^o$.

literature, I have not found a comparison of the discrete resonance phase with the EIT phase. I believe that if the phase of the discrete resonance was compared with the EIT phase, the EIT would not have an increased phase sensitivity compared to the discrete resonance, as I have seen here.

Increasing Dynamic Range

We can broaden the GFR and increase the dynamic range by decreasing the coupling thickness. The large overlap of the fields makes for a large avoided crossing as discussed in chapter V, and this broadens the resonance greatly, increasing dynamic range. At $n = 1.41$, 69.92^o is the critical angle for TIR, and for indexes above that,

	S_R	S_ϕ	R dynamic range
SPR	150	830	0.0018
WCSPR	180	1000	0.0016
Fano	75	290	0.0036
PIT	23	50	0.0093
PIT-Broad	1.6	N/A	0.24

TABLE 1. Intensity and phase sensitivity, and dynamic range for all systems

the SPP mode does not interact with the MIM mode. We can extend the large region of dynamic range by increasing the incident angle, increasing the permittivity before leaving TIR, shown in Fig. 52. For 82°, there is a monotonic increase in reflectance from 0.06 to 0.98 over the range of 1 to 1.38 RIU. This allows for this one sensor to be able to identify a large variety of materials, from vacuum to water. It is not as sensitive to small changes, due to the broad nature of the resonance.

Summary

In Tab. 1 we have collected the sensitivities and dynamic ranges all in one location. For our system, the more the minimum is the dominating feature in the resonance, the higher the sensitivity is for both the intensity and phase. In the transition through the asymmetric GFR to the PIT, the sensitivities decrease and the dynamic range increases. The maximal dynamic range occurs when the peak of the GFR is the dominate feature.

It is unfortunate that we are only able to gain a minimal increase of the sensitivity over the standard SPR. We have learned that by combining a narrow resonance into a Fano resonance, you will not be able to achieve a large increase in sensitivities. Even in cases of a transparency peak, the phase is comparable to a resonance with the same intensity. In order to use a Fano analog to improve sensitivities over the SPR, one would use the SPR as the broad resonance. This has already been done

combining the SPP mode with a dielectric waveguide mode[119, 129]. With the work done in this dissertation, one can quickly understand and explore the tunability of the dielectric waveguide presented in that research, which has not been presented at this time. Other ways to improve upon the SPR sensitivity via mode coupling are being explored, such as study of long range surface plasmons and coupled plasmon-waveguide structures[121].

CHAPTER VIII

CONCLUSION

In this dissertation we have demonstrated coupling between a metallic waveguide mode and a surface plasmon mode that is analogous to Fano interference in atomic systems. Our system is a TiO_2 finite thin film sandwich by two finite Ag films. This finite metal-insulator-metal (MIM) sandwich has semi-infinite thickness exterior insulator on one side and a fused silica prism on the other. We called this a prism-metal-insulator-metal-insulator (PMIMI) stack. We used computation analysis of the mode structure of the SP, metallic waveguide (MIM) and our PMIMI thin film stack. A detailed analytical approach was taken to the modes, allowing for the modes for any number of thin film layers to be explored. Additionally, we calculated the reflected field from the systems to analyse the reflected intensity and phase of the field. Our initial motivation was to explore the sensing capabilities of the PMIMI stack exhibiting a Fano resonance. While our system does not exceed the sensing capabilities of SPR, we have built a well of knowledge of the tunable characteristics of a Fano system.

In chapter II, we reviewed the background information on Fano interference. We discussed the idea of indistinguishable quantum pathways in atomic systems and the interference that leads to the asymmetric Fano resonance. The two pathways excite an electron to continuum mode, one directly, the other via a discrete state. In doing so, we discussed the difference of the pathways in autoionization and electromagnetically induced transparency. The idea of looking at the mode diagrams for an avoided crossing helped understand a signature of Fano interference to look for. Additionally we looked at the Fano resonance equation to be able to identify

when Fano interference is occurring. As part of this, the asymmetry reversal, called q-reversal, was discussed. Finally we discussed the idea of geometric Fano resonances that occur from geometrical modes and their relevant overlap.

Chapter III covered the relevant nature of surface plasmons relevant to the discussion of this thesis. We began with the dielectric properties of metal and how they relate to surface plasmons and why we use silver for this dissertation. This set the region of explorable wavelengths to the visible and infrared portion of the EM spectrum. We then showed the theory for calculating the SPP modes for a single infinite planar interface and the resulting SP frequency. In this it is shown that the SP frequency decreases for increasing permittivity and an overall lowering of the SP mode occurs. From the mode diagrams we are able to see there is a momentum mismatch from the freely propagating light in the insulator and the SPP. This is overcome using the Kretschmann configuration in which a higher index prism is added opposite the insulator creating a finite thickness metal film. The chapter was finished by discussing the SPPs as a form of Fano interference arising from two indistinguishable quantum pathways.

In chapter IV we began analysing systems with higher number of thin films. First explored was a single finite planar film between two semi-infinite thickness films. Both a metal-insulator-metal and an insulator-metal-insulator were discussed, before the focus was made on the MIM system to be used later. The leaky nature of the MIM mode used allows for observation of the MIM resonance with the need for an excitation prism. By making one of the metal layers finite, we added a semi-infinite insulator to look at a metal-insulator-metal-insulator system. We observed the avoided crossing indicative of Fano interference in the mode diagrams in this system. When observing the EM fields of the system, a different symmetry of the modes was observed for

each branch. We added a prism akin to the Kretschmann configuration to access the region of the avoided crossing with input light. The fields in the systems were discussed and explored with a large emphasis of the reflected field of the system. The reflected intensity exhibited the Fano Resonance in the angular domain. We briefly discussed the resonance in the frequency domain and showed that is was not a Fano resonance making this system distinctly have a GFR.

We explored changes to the GFR with parameter variations of our PMIMI stack at length in chapter V. First, we looked at the variations in the angular domain. We showed that the permittivity of the exterior semi-infinite insulator layer shifts the location of the GFR. The thickness and permittivity of the waveguide insulator layer were shown to affect the non-interacting MIM mode and modifying the GFR. The input metal layer was shown to greatly modify the GFR changing both resonance depth and shape. The q-reversal was observed in all of the variations above. The metallic film between the insulators was shown to control the coupling strength. Increasing the prism permittivity was shown to narrow the resonance, as would be expected. We showed that for a given angle, variations in the waveguide permittivity do not exhibit a resonance due to the interference of the system. We were able to observe GFR while with variations to the exterior permittivity. The same effects were seen for parameter variations while varying the exterior permittivity as in the angular domain.

In chapter VI we shifted the focus to the phase of the GFR and explored changes to the material parameters. We used polar plots of the reflected field to gain insight into the phase behavior of resonances. Each resonance appeared as a loop in the polar plot, and knowledge of the size and location of this loop would guide us to the phase behavior and sensitivity. The SPR was first explored and the transition from

monotonic to non-monotonic phase was observed as the resonance crossed the origin. This happened in both the angular domain and as the exterior permittivity was varied. The MIM phase was shown in the angular domain and the same transition was seen for the phase. We moved to the PMIMI stack and the variations of the material parameters and how they affected the phase. The PMIMI in the angular domain consisted of two separate loops, each corresponding to the SP and MIM modes. A decreasing input metal film thickness was shown to expand the MIM loop, and in effect increase the SPR loop. The coupling metal film generally only affected the SPR loop, increasing loop size as the thickness decreased. Below 50 nm, the MIM mode begins to be unsupported and the resonance loops begin to be highly modified. As done for the intensity, we then explored the resonances as the exterior permittivity was varied. In this case, the MIM mode and the angle set the start location of a loop created by the SP mode. The same trends for changes to the metal film thicknesses were seen here as in the angular domain. The general trend that was observed was a decrease of the input thickness and increase of the coupling thickness increased the phase shift through the resonance, as long as the modes still existed and could interact.

Chapter VII used the knowledge gained from chapters V and VI to maximize the intensity and phase sensitivities of the PMIMI stack and explored three different waveguide thicknesses. We began by getting a baseline sensitivity of the SPR. The first waveguide thickness was 115 nm, offsetting the noninteracting SP and MIM modes. In this case both the intensity and phase sensitivity were able to outperform the SPR, but not by much. When we decreased the waveguide thickness to 82.5 nm, to observe a prototypical Fano resonance, the sensitivities went down as the line with increased for a greater dynamic range. As the waveguide thickness was then

adjusted to 83.5 nm to observe a plasmon-assisted transparency, the sensitivities decreased further as the dynamic range increased further. We showed that, for the same intensity maximum and minimum for the PIT and SPR respectively, the SPR had a higher phase sensitivity, proving that this PIT would not be able to out perform SPR in phase detection schemes. We were able to adjust the material parameters such that we had a dynamic range of nearly 0.25 RIU, enough to be able to detect if it were vacuum or water.

Future Work

While this particular system has not been able to out perform SPR, there is still a lot of potential in coupling thin film systems. Mentioned briefly in chapter VII, other groups have been working on systems that involve SP and dielectric waveguide modes exhibiting Fano interference[119, 129]. The reduced losses of the dielectric waveguide mode[1] make it narrower than the SPR. Further exploration of the dielectric waveguide mode and its interactions with the SP mode would be quite easy with the knowledge gained from our system. This is not the only potential interacting system that could be explored. Long range surface plasmon resonances, from the interactions of two surface plasmon modes, have been shown to have a higher sensitivity than SPR as well. It would be possible to combine the LRSPR with the dielectric waveguide mode to observe the interference of the two modes. Another interesting possibility is the interference between my PMIMI modes and the dielectric waveguide modes. At this point I have no explored the interactions of more than two modes, and three mode interactions could prove interesting.

---

[1]if losses are completely neglected, the resonance width of the dielectric waveguide resonance is zero

A more theoretical aspect I have observed and would be interested in exploring would be comparisons of different geometries. In previous work done by our lab, we explored PIT the modes and scattering in MIM microspheres. In comparison to my work here, there become quite a few similarities. Specifically discussing the modes of the system, the mathematical basis behind the two is quite similar. Once the basis of the geometrical boundaries is worked out, is it possible to explore the modes of that basis and the frequency domain. Specifically, in planar systems the basis that we have used has exponentials as the eigenbasis and the wave vector as the eigenvalues, where the microspheres use the spherical Bessel and Hankel functions for the basis and the angular mode number for the eigenvalues. The idea of this could be expanded to other geometries, such as cylindrical, hyperbolic, toroidal and others. I believe that the modes of these systems can be worked out for arbitrary numbers of interfaces in these geometries, as I have done in the dissertation.

Closing Remarks

Throughout the work towards this dissertation, I have come to build a vast knowledge of Fano interference, surface plasmons and thin film systems. It is only with conversations with my fellow lab mates in which I was able to realize the true depth of knowledge I carry with me now. I struggle with adequately expressing this knowledge in type, and continue to endeavor to make my writing more understandable. Knowledge gained is nothing without the ability to pass it on to others.

It has not been an easy path for me to overcome some of the barriers that I have come across throughout my time here at the University of Oregon. When I first did the sensitivity analysis of my system in comparison to SPR and found it lacking, I

could not let that stop me, there was still much work to be done. During this time I also found the papers by Hayashi et al of the dielectric WCSPR, another strong blow landed deterring me from my path. But without barriers to overcome, one can not grow beyond their current self. Often you gain more knowledge by being wrong in your hypothesis than being correct from the beginning, as long as you can admit you were wrong. I hope that future students reading this dissertation understand that more than anything else.

All that is gold does not glitter, not all those who wander are lost.

J.R.R. Tolkien, The Fellowship of the Ring

APPENDIX A

MULTILAYER PLANAR SYSTEMS MODE FORMALISM

This appendix covers the formalism for calculating the modes for a thin film stack of any number of layers. There are several ways to approach calculating the mode equation for multilayer systems, but we take the approach of extending the formalism used for the SP modes given in chapter III. We start the discussion with a two interface system, and then move into higher layer thin films.

Two Interfaces

The solution assumed is of the same form as Eq. (3.4), where we now have terms that decay away from both interfaces.

$$
\boldsymbol{E} = \begin{cases}
(\hat{\boldsymbol{x}}E_{+1x} + \hat{\boldsymbol{z}}E_{+1z}) \cdot e^{ik_\parallel z + k_1 x - i\omega t} & x < 0 \\
(\hat{\boldsymbol{x}}E_{+2x} + \hat{\boldsymbol{z}}E_{+2z}) \cdot e^{ik_\parallel z + k_2 x - i\omega t} + (\hat{\boldsymbol{x}}E_{-2x} + \hat{\boldsymbol{z}}E_{-2z}) \cdot e^{ik_\parallel z - k_2 x - i\omega t} & 0 < x < t_2 \\
(\hat{\boldsymbol{x}}E_{-3x} + \hat{\boldsymbol{z}}E_{-3z}) \cdot e^{ik_\parallel z - k_3 x - i\omega t} & t_2 < x
\end{cases}
$$
$$(A.1)$$

where $E_{+/-,n,x/z}$ are the electric field components for a term decay in the negative/positive (+/-) directions in the nth layer for the x/z component. $k_\parallel$ is the wave vector along the direction of propagation and k_n are the decay terms into each respective layer (assumed to be positive). The thickness of the film is taken to be t_2 (always positive).
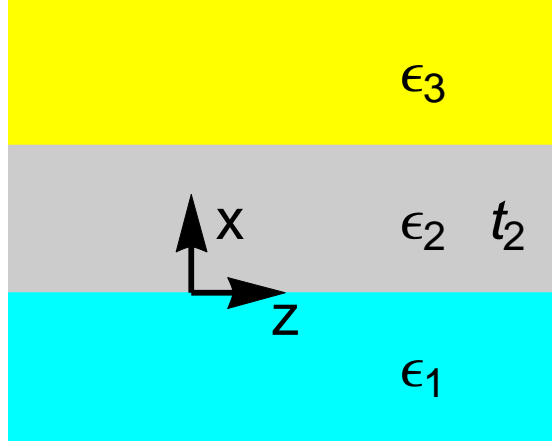
94

FIGURE 53. Two interface/three layer system diagram
Schematic diagram of a three layer system, with coordinates used for equations
(A.1) and (A.2).

Again the magnetic field is TM in nature and is given by

$$
\boldsymbol{H} = \begin{cases} (\hat{\boldsymbol{y}} H_{+1}) \cdot e^{ik_\parallel z + k_1 x - i\omega t} & x < 0 \\ (\hat{\boldsymbol{y}} H_{+2}) \cdot e^{ik_\parallel z + k_2 x - i\omega t} + (\hat{\boldsymbol{y}} H_{-2}) \cdot e^{ik_\parallel z - k_2 x - i\omega t} & 0 < x < t_2 \\ (\hat{\boldsymbol{y}} H_{-3}) \cdot e^{ik_\parallel z - k_3 x - i\omega t} & t_2 < x \end{cases} \qquad (A.2)
$$

We relate the electric and magnetic fields the same as before using Eq. (3.6). This time we can match the x/z components as before, but additionally the $+/-$ terms can be matched by the exponential. This gives us the relations:

$$
\begin{aligned}
H_{+1} &= +\tfrac{\epsilon_1}{k_1} i \tfrac{\omega}{c} E_{+1z} \\
H_{+2} &= +\tfrac{\epsilon_2}{k_2} i \tfrac{\omega}{c} E_{+2z} \\
H_{-2} &= -\tfrac{\epsilon_2}{k_2} i \tfrac{\omega}{c} E_{-2z} \\
H_{-3} &= -\tfrac{\epsilon_3}{k_3} i \tfrac{\omega}{c} E_{-3z}
\end{aligned} \qquad (A.3)
$$

$$H_{+1} = \frac{\epsilon_1}{k_\parallel} \frac{\omega}{c} E_{+1x}$$

$$H_{+2} = \frac{\epsilon_2}{k_\parallel} \frac{\omega}{c} E_{+2x}$$

$$H_{-2} = \frac{\epsilon_2}{k_\parallel} \frac{\omega}{c} E_{-2x}$$

$$H_{-3} = \frac{\epsilon_3}{k_\parallel} \frac{\omega}{c} E_{-3x}$$

(A.4)

and equating Eq. (A.3) and Eq. (A.4), we get

$$E_{+1x} = +\frac{k_\parallel}{k_1} i E_{+1z}$$

$$E_{+2x} = +\frac{k_\parallel}{k_2} i E_{+2z}$$

$$E_{-2x} = -\frac{k_\parallel}{k_2} i E_{-2z}$$

$$E_{-3x} = -\frac{k_\parallel}{k_3} i E_{-3z}$$

(A.5)

We now apply the standard boundary conditions at each interface to get

$$E_{+1\parallel} = E_{+2\parallel} + E_{-2\parallel} \quad \text{at } x = 0$$

$$E_{+2\parallel} + E_{-2\parallel} = E_{-3\parallel} \quad \text{at } x = t_2$$

(A.6)

$$H_{+1\parallel} = H_{+2\parallel} + H_{-2\parallel} \quad \text{at } x = 0$$

$$H_{+2\parallel} + H_{-2\parallel} = H_{-3\parallel} \quad \text{at } x = t_2$$

(A.7)

Using Eq. (A.3) for H in Eq. (A.7) we get

$$E_{+1z} = E_{+2z} + E_{-2z}$$

$$E_{+2z} \cdot e^{k_2 t_2} + E_{-2z} \cdot e^{-k_2 t_2} = E_{-3z} \cdot e^{-k_3 t_2}$$

$$\frac{\epsilon_1}{k_1} E_{+1z} = \frac{\epsilon_2}{k_2} E_{+2z} - \frac{\epsilon_2}{k_2} E_{-2z}$$

$$\frac{\epsilon_2}{k_2} E_{+2z} \cdot e^{k_2 t_2} - \frac{\epsilon_2}{k_2} E_{-2z} \cdot e^{-k_2 t_2} = -\frac{\epsilon_3}{k_3} E_{-3z} \cdot e^{-k_3 t_2}$$

(A.8)

To solve this system of equation, we use linear algebra techniques, specifically Cramer's Rule[130]. We start by bringing all the terms to one side of the equation in

Eq. (A.8) and changing the order such that the first two equations deal with the first interface and the last two are the second interface terms.

$$E_{+1z} - E_{-2z} - E_{+2z} = 0$$

$$\tfrac{\epsilon_1}{k_1} E_{+1z} + \tfrac{\epsilon_2}{k_2} E_{-2z} - \tfrac{\epsilon_2}{k_2} E_{+2z} = 0$$

$$E_{-2z} \cdot e^{-k_2 t_2} + E_{+2z} \cdot e^{k_2 t_2} - E_{-3z} \cdot e^{-k_3 t_2} = 0 \tag{A.9}$$

$$-\tfrac{\epsilon_2}{k_2} E_{-2z} \cdot e^{-k_2 t_2} + \tfrac{\epsilon_2}{k_2} E_{+2z} \cdot e^{k_2 t_2} + \tfrac{\epsilon_3}{k_3} E_{-3z} \cdot e^{-k_3 t_2} = 0$$

In matrix formalism this is

$$
\begin{pmatrix}
1 & -1 & -1 & 0 \\
\tfrac{\epsilon_1}{k_1} & \tfrac{\epsilon_2}{k_2} & -\tfrac{\epsilon_2}{k_2} & 0 \\
0 & e^{-k_2 t_2} & e^{k_2 t_2} & -e^{-k_3 t_2} \\
0 & -\tfrac{\epsilon_2}{k_2} e^{-k_2 t_2} & \tfrac{\epsilon_2}{k_2} e^{k_2 t_2} & \tfrac{\epsilon_3}{k_3} e^{-k_3 t_2}
\end{pmatrix}
\begin{pmatrix}
E_{+1z} \\
E_{-2z} \\
E_{+2z} \\
E_{-3z}
\end{pmatrix}
=
\begin{pmatrix}
0 \\
0 \\
0 \\
0
\end{pmatrix}
\tag{A.10}
$$

To illuminate the Cramer's rule and its application to determining the resonance condition for this matrix, we revisit the single interface system. Eq. (3.12) rewritten:

$$E_{1z} - E_{2z} = 0$$

$$\tfrac{\epsilon_1}{k_1} E_{1z} + \tfrac{\epsilon_2}{k_2} E_{2z} = 0 \tag{A.11}$$

then into matrix form

$$
\begin{pmatrix}
1 & -1 \\
\tfrac{\epsilon_1}{k_1} & \tfrac{\epsilon_2}{k_2}
\end{pmatrix}
\begin{pmatrix}
E_{1z} \\
E_{2z}
\end{pmatrix}
=
\begin{pmatrix}
0 \\
0
\end{pmatrix}
\tag{A.12}
$$

Which can be interpreted as

$$\boldsymbol{M} \cdot \boldsymbol{E} = \boldsymbol{0} \tag{A.13}$$

Taking the determinate of $\mathbf{M}$ and setting it equal to zero gives us

$$\frac{\epsilon_1}{k_1} + \frac{\epsilon_2}{k_2} = 0 \tag{A.14}$$

or Eq. (3.13) in another form. In Cramer's rule, the determine of the matrix gives the denominator of the solution for the coefficients. As is standard in resonance theory, when the denominator goes to zero, this gives us a resonance condition.

Returning to Eq. (A.10), we define $\xi_n \equiv \frac{\epsilon_n}{k_n}$ and take the determinate of the matrix.

$$\begin{vmatrix} 1 & -1 & -1 & 0 \\ \xi_1 & \xi_2 & -\xi_2 & 0 \\ 0 & e^{-k_2 t_2} & e^{k_2 t_2} & -e^{-k_3 t_2} \\ 0 & -\xi_2 e^{-k_2 t_2} & \xi_2 e^{k_2 t_2} & \xi_3 e^{-k_3 t_2} \end{vmatrix} = ((\xi_1 - \xi_2)(-\xi_2 + \xi_3) - (\xi_1 + \xi_2)(\xi_2 + \xi_3) \cdot e^{2k_2 t_2}) \cdot e^{-t_2(k_2 + k_3)} \tag{A.15}$$

and setting this equal to zero for resonance, the external exponentials drop out and we are left with

$$(\xi_1 - \xi_2)(-\xi_2 + \xi_3) - (\xi_1 + \xi_2)(\xi_2 + \xi_3) \cdot e^{2k_2 t_2} = 0 \tag{A.16}$$

which is the two interface mode equation.

The wave equation (Eq. (3.14)) still gives us the relation

$$k_i^2 = k_\parallel^2 - \epsilon_i \left(\frac{\omega}{c}\right)^2 \tag{A.17}$$

where i indicates the layer in which it occurs. Due to continuity, $k_\parallel$ is the same for all layers. Combining Eq. (A.16) with Eq. (A.17) and remembering $\xi_n = \frac{\epsilon_n}{k_n}$, the only

unknowns are $k_\parallel$ and ω. The solutions to this equation are multi-valued and are not algebraically solvable. In practice, computers can calculate the determinate and find zeroes of the two interface mode equation or the plot the dispersion in a density plot.

We continue with some algebraic manipulation to find a general trend in a system of any number of layers. First the terms are expanded, and we divide by $e^{k_2 t_2}$ to get

$$(-\xi_1\xi_2 + \xi_1\xi_3 + \xi_2^2 - \xi_2\xi_3) \cdot e^{-k_2 t_2} - (\xi_1\xi_2 + \xi_1\xi_3 + \xi_2^2 + \xi_2\xi_3) \cdot e^{k_2 t_2} = 0 \qquad (A.18)$$

noticing that the four terms $\xi_1\xi_2, \xi_1\xi_3, \xi_2^2, \xi_2\xi_3$ appear before both exponents. Each is matched to create either a hyperbolic sine or cosine pair.

$$(\xi_1\xi_2 + \xi_2\xi_3) \cdot \cosh k_2 t_2 + (\xi_1\xi_3 + \xi_2^2) \cdot \sinh k_2 t_2 = 0 \qquad (A.19)$$

The last manipulations are to pull out ξ_2, a common factor, and divide by the hyperbolic cosine to get

$$\xi_2(\xi_1 + \xi_3) + (\xi_1\xi_3 + \xi_2^2) \cdot \tanh k_2 t_2 = 0 \qquad (A.20)$$

Looking at the first term, we notice this is similar to Eq. (A.14), if we removed the film layer from the system. We refer to this as the single interface term. The second term, multiplied by $\tanh k_2 t_2$ is referred to as a two interface term. This first part contains ξ for the first and final layer, while the second part is the ξ for the film.

Eq. (A.20) with Eq. (A.17) can be used to find the solutions of ω for a given $k_\parallel$ or vis versa. As stated previously, this needs to be done numerically as no direct solution is possible.
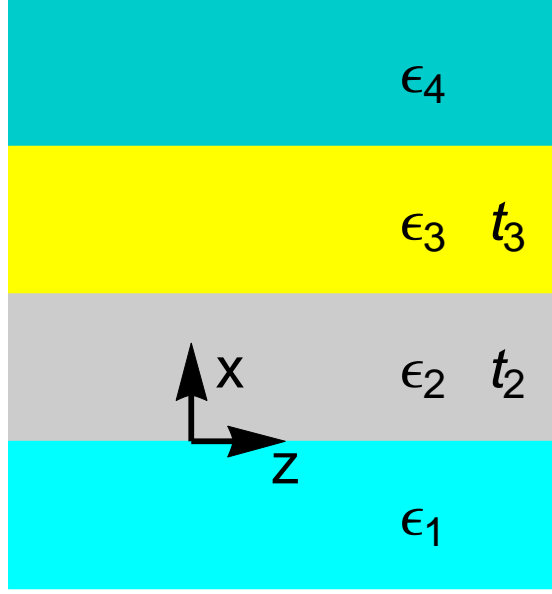
FIGURE 54. Three interface/four layer system diagram
Schematic diagram of a four layer system, with coordinates used for Eq. (A.21).

Three Interfaces and Beyond

We now discuss four layers, expedited as the steps follow the same as for the three layer system. The solution assumed is of the same form where we now have decay terms away from both interfaces.

$$
\boldsymbol{E} = \begin{cases} (\hat{\boldsymbol{x}}E_{+1x} + \hat{\boldsymbol{z}}E_{+1z}) \cdot e^{ik_{\parallel}z + k_1x - i\omega t} & x < 0 \\ (\hat{\boldsymbol{x}}E_{+2x} + \hat{\boldsymbol{z}}E_{+2z}) \cdot e^{ik_{\parallel}z + k_2x - i\omega t} + (\hat{\boldsymbol{x}}E_{-2x} + \hat{\boldsymbol{z}}E_{-2z}) \cdot e^{ik_{\parallel}z - k_2x - i\omega t} & 0 < x < t_2 \\ (\hat{\boldsymbol{x}}E_{+3x} + \hat{\boldsymbol{z}}E_{+3z}) \cdot e^{ik_{\parallel}z + k_3x - i\omega t} + (\hat{\boldsymbol{x}}E_{-3x} + \hat{\boldsymbol{z}}E_{-3z}) \cdot e^{ik_{\parallel}z - k_3x - i\omega t} & t_2 < x < t_2 + t_3 \\ (\hat{\boldsymbol{x}}E_{-4x} + \hat{\boldsymbol{z}}E_{-4z}) \cdot e^{ik_{\parallel}z - k_4x - i\omega t} & t_2 + t_3 < x \end{cases}
$$

(A.21)

Again, $E_{+/-,n,x/z}$ are the electric field components for a term decay in the negative/positive (+/-) directions in the nth layer for the x/z component. $k_{\parallel}$ is the wave vector along the direction of propagation and k_n are the decay terms into

each respective layer (assumed to be positive). The thickness of the films are taken positive.

Maxwell's equations are used for matching of the field amplitudes, boundary conditions are imposed at each interface and we get

$$
\begin{pmatrix}
1 & -1 & -1 & 0 & 0 & 0 \\
\xi_1 & \xi_2 & -\xi_2 & 0 & 0 & 0 \\
0 & e^{-k_2 t_2} & e^{k_2 t_2} & -e^{-k_3 t_2} & -e^{k_3 t_2} & 0 \\
0 & -\xi_2 e^{-k_2 t_2} & \xi_2 e^{k_2 t_2} & \xi_3 e^{-k_3 t_2} & -\xi_3 e^{k_3 t_2} & 0 \\
0 & 0 & 0 & e^{-k_3(t_2+t_3)} & e^{k_3(t_2+t_3)} & -e^{-k_4(t_2+t_3)} \\
0 & 0 & 0 & -\xi_3 e^{-k_3(t_2+t_3)} & \xi_3 e^{k_3(t_2+t_3)} & \xi_4 e^{k_4(t_2+t_3)}
\end{pmatrix}
\begin{pmatrix}
E_{+1z} \\ E_{-2z} \\ E_{+2z} \\ E_{-3z} \\ E_{+3z} \\ E_{-4z}
\end{pmatrix}
=
\begin{pmatrix}
0 \\ 0 \\ 0 \\ 0 \\ 0 \\ 0
\end{pmatrix}
\tag{A.22}
$$

Note that as an interface is added, the matrix expands its dimensions by 2. The new columns represent the two new fields, and the new rows represent the boundary condition equations for the interface. To illuminate this, in Eq. (A.22), Eq. (A.12) and Eq. (A.10) exist as the upper left 2x2 and 4x4 sub-matrices, respectively.

Taking the determinate of the matrix in Eq. (A.22) and setting it equal to zero, we get

$$
\begin{aligned}
&(1 - e^{2k_2 t_2})(\xi_2^2(\xi_3 - \xi_4 + e^{2k_3 t_3}(\xi_3 + \xi_4)) + \xi_3\xi_4(-\xi_3 + \xi_4 + e^{2k_3 t_3}(\xi_3 + \xi_4))) + \\
&(1 + e^{2k_2 t_2})\xi_2((\xi_1 - \xi_3)(-\xi3 + \xi_4) - e^{2k_3 t_3}(\xi_1 + \xi_3)(\xi3 + \xi_4)) = 0
\end{aligned}
\tag{A.23}
$$

Performing similar manipulations as was discussed in the two interface system, we get

$$
\begin{aligned}
&\xi_2\xi_3(\xi_1 + \xi_4) + \\
&\xi_3 \tanh k_2 t_2(\xi_1\xi_4 + \xi_2^2) + \xi_2 \tanh k_3 t_3(\xi_1\xi_4 + \xi_3^2) + \\
&\tanh k_2 t_2 \tanh k_3 t_3(\xi_1\xi_3^2 + \xi_2^2\xi_4) = 0
\end{aligned}
\tag{A.24}
$$

101

The first term in Eq. (A.24) is the one-interface term, where the 2nd and 3rd layers have been removed. The second two terms are two-interface terms, one for each internal layer. The layer that remains is multiplied by a tanh term containing the decay term of that layer and the thickness of that layer. The last term is a three-interface term; note that it is multiplied by both $\tanh k_2 t_2$ and $\tanh k_3 t_3$ since both films are being considered.

The same process can be repeated for four interfaces and we get[1]

$$\xi_2\xi_3\xi_4(\xi_1+\xi_5)+$$
$$\xi_3\xi_4\tanh k_2 t_2(\xi_1\xi_5+\xi_2^2) + \xi_2\xi_4\tanh k_3 t_3(\xi_1\xi_5+\xi_3^2) + \xi_2\xi_3\tanh k_4 t_4(\xi_1\xi_5+\xi_4^2)+$$
$$\xi_4\tanh k_2 t_2\tanh k_3 t_3(\xi_1\xi_3^2+\xi_2^2\xi_5) + \xi_3\tanh k_2 t_2\tanh k_4 t_4(\xi_1\xi_4^2+\xi_2^2\xi_5)+$$
$$\xi_2\tanh k_3 t_3\tanh k_4 t_4(\xi_1\xi_4^2+\xi_3^2\xi_5) + \tanh k_2 t_2\tanh k_3 t_3\tanh k_4 t_4(\xi_1\xi_3^2\xi_5+\xi_2^2\xi_4^2) = 0$$
$$(A.25)$$

Again, we have one one-interface term. We have three two-interface terms, one for each individual layer. We also have three three-interface terms, one for each time a single layer is removed. Lastly, we have a new term for the four-interface term, in which all layers are included and none are neglected.

The emergent pattern is shown in Tables 2 and 3. In Tab. 2, we show the progression of the interface terms, and include a general formula for an nth layer term (odd or even). As a new interface is added, the first part of the lower interface term is multiplied by the highest order odd layer and the second part is multiplied by the highest order even layer.

Tab. 3 shows the pattern for the number of interface terms. The number of terms follows the principles of counting[130] and combinatorics To help understand this, I'll discuss the 5 interface systems to understand the counting for the number

---

[1]After some EXTREME algebra

102

# of Interfaces	term
One	$\xi_1 + \xi_2$
Two	$\xi_1\xi_3 + \xi_2^2$
Three	$\xi_1\xi_3^2 + \xi_2^2\xi_4$
Four	$\xi_1\xi_3^2\xi_5 + \xi_2^2\xi_4^2$
$\vdots$	
n interfaces (n Odd)	$\xi_1\left(\displaystyle\prod_{i=3,\ i\ \text{odd}}^{n}\xi_i^2\right) + \left(\displaystyle\prod_{i=2,\ i\ \text{even}}^{n-1}\xi_i^2\right)\xi_{n+1}$
n interfaces (n Even)	$\xi_1\left(\displaystyle\prod_{i=3,\ i\ \text{odd}}^{n-1}\xi_i^2\right)\xi_{n+1} + \left(\displaystyle\prod_{i=2,\ i\ \text{even}}^{n}\xi_i^2\right)$

TABLE 2. Mode equation terms
Shows the term for each number of interfaces. A pattern is observed and new terms for more interfaces can be added.

# of Interfaces	1 terms	2 terms	3 terms	4 terms	5 terms	m terms
One	1					$\binom{0}{m-1}$
Two	1	1				$\binom{1}{m-1}$
Three	1	2	1			$\binom{2}{m-1}$
Four	1	3	3	1		$\binom{3}{m-1}$
Five	1	4	6	4	1	$\binom{4}{m-1}$
n interfaces	$\binom{n-1}{0}$	$\binom{n-1}{1}$	$\binom{n-1}{2}$	$\binom{n-1}{3}$	$\binom{n-1}{4}$	$\binom{n-1}{m-1}$

TABLE 3. Number of mode equation terms
Shows the number of terms for each number of interfaces. A pattern is observed and we are able to find the number of terms akin to the binomial expansion.

of terms. When considering the five-interface term for a five-interface system, all films must be considered, so there is only one five-interface term. Moving to the four-interface term, one film must be removed, and there are four ways to do this, thus four four-interface terms. The three-interface term, has two films removed. So from the four films, we must choose two films to be removed; The number of countable ways to do this is six. The two-interface term, we must remove three films, leaving one film: four two-interface terms. Lastly, with all the films removed, we have one one-interface term. In a less intuitive approach, we could have added layers as we increased the number of interfaces. This train of thought leads to easier mathematical considerations. Specifically, for an n interface system when considering the m interface term, we use n-1 choose m-1, or

$$\binom{n-1}{m-1} = \frac{(n-1)!}{(m-1)!(n-m)!} \tag{A.26}$$

When creating the full mode equation for a n interface system, combinatorics can be used to assemble the proper system. As an example consider the four interface system shown in Fig. 55. It has been broken down into the $2^3 = 8$ sub-systems that need to be considering. For each of the sub-systems, there is an associated term in the total mode equation, as evidenced in Eq. (A.25).

Using this knowledge and procedure, an analytical expression for any number of interfaces can be created, and while this expression becomes increasingly cumbersome, there could be potential applications of this exact analytical formula in the future.
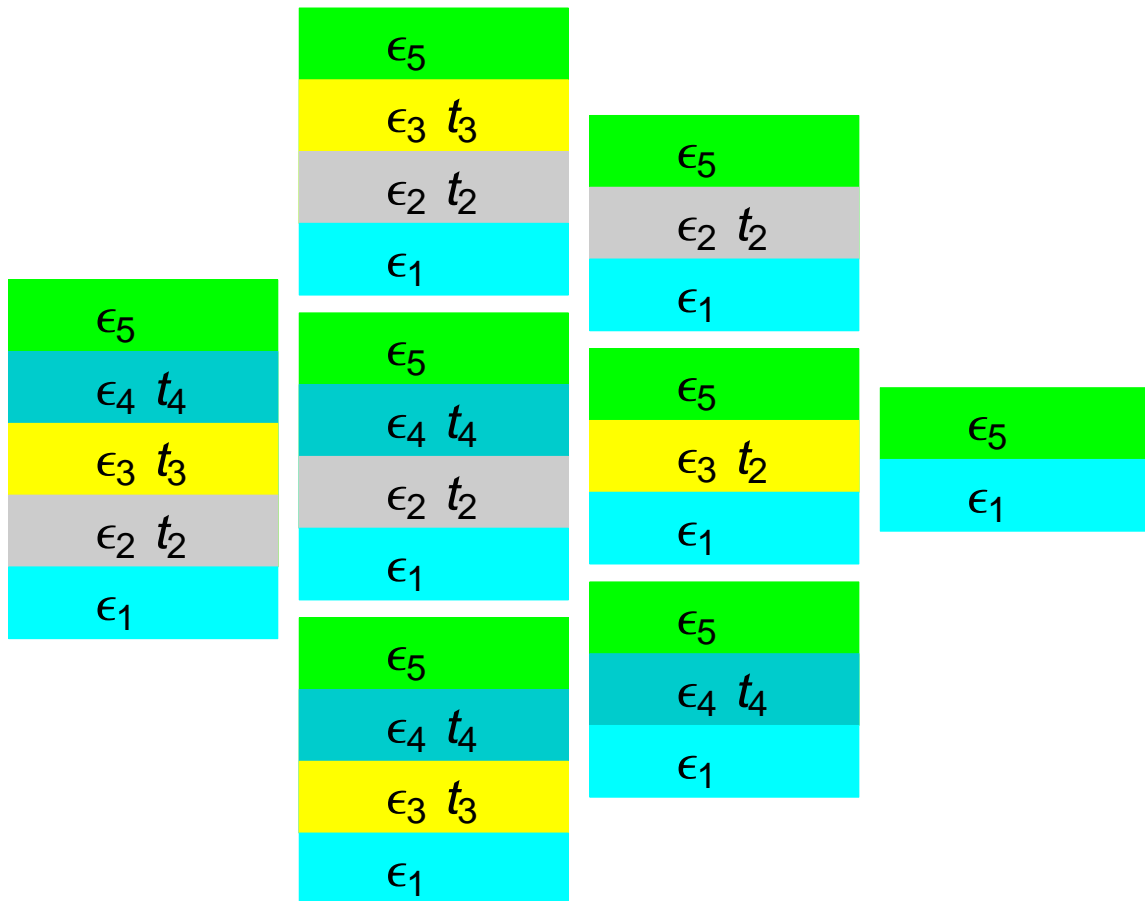
FIGURE 55. Four interface system diagram with layers broken down
Schematic diagram of a five layer system (three films) and all subsystems.

APPENDIX B

FORMALISM FOR REFLECTIVITY AND TRANSMISSIVITY

We now discuss light incident into the layered system from the first interface. The material covered in this section is mostly textbook[109] and included here for quick reference. We first discuss the Fresnel formulation and its similarities to the mode derivation. While there is a good intuition built from Fresnel formulation for many interfaces, it is not optimal for the quickest computational basis. So we also discuss the matrix formulation of reflectivity and transmissivity which is computationally much quicker. We end with discussing a technique to get the field amplitudes in all of the layers.

Fresnel Formulation of Reflectivity and Transmissivity

Similar to finding the mode distribution of the planar systems, we start with one interface and move up in the number of interfaces. We discuss the TM fields here. Having one interface, we have an incident EM wave from the negative x direction, with a reflected and transmitted wave, see Fig. 56. The fields are given as

$$\boldsymbol{E} = \begin{cases} (\boldsymbol{E_{+2}} \cdot e^{-i\boldsymbol{k_{+2}} \cdot \boldsymbol{r}}) \cdot e^{i\omega t} & x > 0 \\ (\boldsymbol{E_{+1}} \cdot e^{-i\boldsymbol{k_{+1}} \cdot \boldsymbol{r}} + \boldsymbol{E_{-1}} \cdot e^{-i\boldsymbol{k_{-1}} \cdot \boldsymbol{r}}) \cdot e^{i\omega t} & x < 0 \end{cases} \tag{B.1}$$

where $\boldsymbol{E_{+/-,n}}$ are the complex electric fields propagating in the positive/negative (+/-) directions in the nth layer; $\boldsymbol{k_{+1}}$, $\boldsymbol{k_{-1}}$ and $\boldsymbol{k_{+2}}$ are the incident, reflected and transmitted wave vectors, respectively. $\boldsymbol{k_{+1}}$ and $\boldsymbol{k_{-1}}$ has the same z component, but opposite x components. $\boldsymbol{k_{+2}}$ is refracted by defined by Snell's law. We can get the magnetic field from Maxwell's equations (Eq. (3.6)) and use the boundary conditions

106
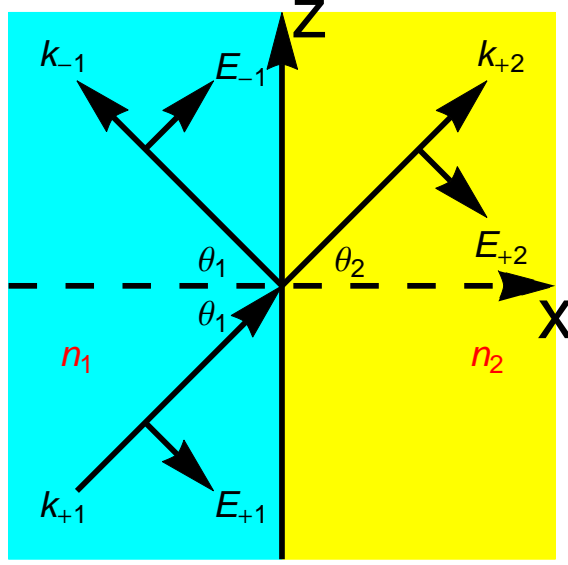
FIGURE 56. Reflected and transmitted waves at a single interface
Schematic diagram of reflected and transmitted waves at a single interface between
two semi infinite layers of index n_1 and n_2. The k-vectors point along the direction
of propagation and the electric fields are defined positive for each. Upon reflection,
the z component of the electric field switches sign while the transmitted electric field
continues to have the same signs as the input field. The magnetic fields are not
shown, but would be poitning into the page for all three fields.

to find the field amplitudes. We use the z component of the electric field and the y

component of the magnetic field for the boundary conditions to get

$$(|\boldsymbol{E}_{+1}| - |\boldsymbol{E}_{-1}|)\cos\theta_1 = |\boldsymbol{E}_{+2}|\cos\theta_2$$
$$\frac{\epsilon_1}{k_1}(|\boldsymbol{E}_{+1}| + |\boldsymbol{E}_{-1}|) = \frac{\epsilon_2}{k_2}|\boldsymbol{E}_{+2}|$$

(B.2)

noting that $k_i = n_i(\omega/c)$, we can solve for the reflectivity and transmissivity:

$$r_{12,TM} = \frac{|\boldsymbol{E}_{-1}|}{|\boldsymbol{E}_{+1}|} = \frac{n_1\cos\theta_2 - n_2\cos\theta_1}{n_1\cos\theta_2 + n_2\cos\theta_1}$$

(B.3)

$$t_{12,TM} = \frac{|\boldsymbol{E}_{+2}|}{|\boldsymbol{E}_{+1}|} = \frac{2n_1\cos\theta_2}{n_1\cos\theta_2 + n_2\cos\theta_1}$$

(B.4)

which relate the reflected and transmitted amplitudes, but not intensities. A similar derivation for Transverse Electric (TE) fields grants

$$r_{12,TE} = \frac{|\boldsymbol{E}_{-1,TE}|}{|\boldsymbol{E}_{+1,TE}|} = \frac{n_1 \cos\theta_1 - n_2 \cos\theta_2}{n_1 \cos\theta_1 + n_2 \cos\theta_2} \tag{B.5}$$

$$t_{12,TE} = \frac{|\boldsymbol{E}_{+2,TE}|}{|\boldsymbol{E}_{+1,TE}|} = \frac{2n_1 \cos\theta_1}{n_1 \cos\theta_1 + n_2 \cos\theta_2} \tag{B.6}$$

For intensities, the Poynting vector must be used and we get the following for the reflectance and transmittance:

$$R = |r|^2 \tag{B.7}$$

$$T = \frac{n_2 \cos\theta_2}{n_1 \cos\theta_1} |t|^2 \tag{B.8}$$

for both TM and TE waves for a single interface.

Moving to two interfaces, there are multiple derivations. Yeh[109] covers three such derivations: Extending the formalism show above, a modification of the formalism in which r and t are presumed from the beginning and Airy's formula, which sums an infinite series of reflections and transmissions. All derivations lead to the following equations for the reflectivity and transmissivity for two interfaces:

$$r_{123} = \frac{r_{12} + r_{23}e^{-2i\phi_2}}{1 + r_{12}r_{23}e^{-2i\phi_2}} \tag{B.9}$$

$$t_{123} = \frac{t_{12}t_{23}e^{-2i\phi_2}}{1 + r_{12}r_{23}e^{-2i\phi_2}} \tag{B.10}$$

where r_{nm} and t_{nm} are the reflectivity and transmissivity at the interface of the nth and mth layers and

$$\phi_i = k_{xi} t_i = \frac{2\pi t_i}{\lambda} n_i \cos \theta_i \qquad \text{(B.11)}$$

These equations hold for both TM and TE waves, as long as the proper r and t are used for each case. For reflection and transmission, we have the similar form, but now it is given by

$$R = |r_{123}|^2 \qquad \text{(B.12)}$$

$$T = \frac{n_3 \cos \theta_3}{n_1 \cos \theta_1} |t_{123}|^2 \qquad \text{(B.13)}$$

Where we have now used the Poynting's vectors for the first and final layers.

Just as there are different derivations for two interfaces, there are different derivations for any number of interfaces. We present three different methods and explain the advantage and disadvantage of each.

Recursive collapsing into effective reflection and transmission coefficients

The first derivation we discuss is deals with effective reflection and transmission coefficients of the individual layers. As an example, we consider the three-interface system and then move to the general formalism using a recursive definition. As equations (B.9) and (B.10) have shown us, we can treat two interfaces as an effective r and t. Looking at the four layer system, the reflection and transmission about the 3rd layer can be combined to and effective r_{234} and t_{234}. We consider these effective coefficients as part of a three layer system, with modified r and t for the 2nd interface. At this point we use equations (B.9) and (B.10) to turn it into an effective two layer system, giving us the reflectivity and transmissivity of the entire system. Mathematically, we would have (for TM waves)
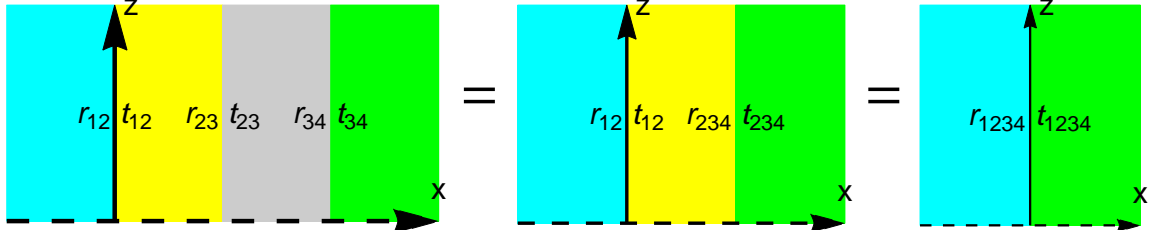
FIGURE 57. Diagrams from three interfaces to one effective interface
The four layer system can be made a three layer by effective coefficients of the last terms. Then equations (B.9) and (B.10) make the effective single interface picture.

$$r_{34} = \frac{n_3 \cos\theta_4 - n_4 \cos\theta_3}{n_3 \cos\theta_4 + n_4 \cos\theta_3}$$
$$t_{34} = \frac{2n_4 \cos\theta_3}{n_3 \cos\theta_4 + n_4 \cos\theta_3}$$

(B.14)

$$r_{234} = \frac{r_{23} + r_{34}e^{-2i\phi_3}}{1 + r_{23}r_{34}e^{-2i\phi_3}}$$
$$t_{234} = \frac{t_{23}t_{34}e^{-2i\phi_3}}{1 + r_{23}r_{34}e^{-2i\phi_3}}$$

(B.15)

$$r_{1234} = \frac{r_{12} + r_{234}e^{-2i\phi_2}}{1 + r_{12}r_{234}e^{-2i\phi_2}}$$
$$t_{1234} = \frac{t_{12}t_{234}e^{-2i\phi_2}}{1 + r_{12}r_{234}e^{-2i\phi_2}}$$

(B.16)

From this idea and formalism, this allows a recursive program to be built, which calls upon equations (B.9) and (B.10), using the lower level effective coefficients in the equation. Once the program calls upon the last single interface, the recursion is stopped. The standard Fresnel coefficients (equations (B.3) and (B.4)) are calculated and begins calculating each effective interface back outwards.

It is important to note that the reflected and transmitted intensities are still given by

$$R = |r_{total}|^2$$

(B.17)

$$T = \frac{n_{final} \cos\theta_{final}}{n_1 \cos\theta_1} |t_{total}|^2$$

(B.18)

Where we have now used the Poynting's vectors for the first and final layers.
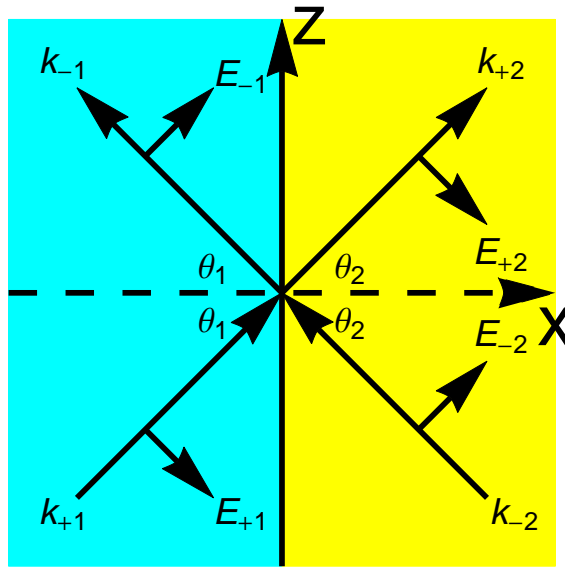
FIGURE 58. Waves at a single interface incident from both sides
Schematic diagram of reflected and transmitted waves at a single interface including
a counter-propagating wave in the second medium.

This method is useful for thought analysis of effective layers and being able to
treat complex systems as effective r and t. Recursive functions are not known for the
efficiency of calculations, and fall behind the other methods we discuss. Additionally,
this method does not give amplitudes in the inside layers. We move to discuss the
fastest and easiest method of calculating the reflectivity and transmissivity.

Matrix formalism for quick computations

Matrix formalism is easy to implement and quite quick for computational work.
Also covered by Yeh[109], the basics are given here. We being by first considering a
single interface to see how the method works compared to Fresnel formulation. We
first consider a similar picture as before, but now include a wave propagating the the
negative direction in the 2nd layer, Fig.58.

The same process for the boundary system holds as Eq. (B.2) (TM) with an additional term for the new directional wave.

$$(|\boldsymbol{E}_{+1}| - |\boldsymbol{E}_{-1}|)\cos\theta_1 = (|\boldsymbol{E}_{+2}| - |\boldsymbol{E}_{-2}|)\cos\theta_2$$
$$n_1(|\boldsymbol{E}_{+1}| + |\boldsymbol{E}_{-1}|) = n_2(|\boldsymbol{E}_{+2}| + |\boldsymbol{E}_{-2}|)$$

(B.19)

Which can be written in Matrix form as

$$\begin{pmatrix} \cos\theta_1 & -\cos\theta_1 \\ n_1 & n_1 \end{pmatrix} \begin{pmatrix} E_{+1} \\ E_{-1} \end{pmatrix} = \begin{pmatrix} \cos\theta_2 & -\cos\theta_2 \\ n_2 & n_2 \end{pmatrix} \begin{pmatrix} E_{+2} \\ E_{-2} \end{pmatrix}$$

(B.20)

or

$$\boldsymbol{D}_1 \begin{pmatrix} E_{+1} \\ E_{-1} \end{pmatrix} = \boldsymbol{D}_2 \begin{pmatrix} E_{+2} \\ E_{-2} \end{pmatrix}$$

(B.21)

which we multiply by the inverse of $\boldsymbol{D}_1$ to get

$$\begin{pmatrix} E_{+1} \\ E_{-1} \end{pmatrix} = \boldsymbol{D}_1^{-1}\boldsymbol{D}_2 \begin{pmatrix} E_{+2} \\ E_{-2} \end{pmatrix}$$

(B.22)

defining the transmission matrix, $\boldsymbol{D}_{12}$, as

$$\boldsymbol{D}_{12} = \begin{pmatrix} D_{11} & D_{12} \\ D_{21} & D_{22} \end{pmatrix} = \boldsymbol{D}_1^{-1}\boldsymbol{D}_2$$

(B.23)

and it can be shown, for no wave incident from the right, that

$$r = \frac{D_{21}}{D_{11}}$$
$$t = \frac{1}{D_{11}}$$

(B.24)

Moving to two-interfaces, we now have to consider the finite thickness of the film layer. This is done using a propagation matrix which relates the phase of the wave from one interface to the next given by

$$
\boldsymbol{P}_i = \begin{pmatrix} e^{i\phi_i} & 0 \\ 0 & e^{-i\phi_i} \end{pmatrix}
\tag{B.25}
$$

where ϕ_i is the phase gained during propagation and is given by Eq. (B.11). For this two-interface system, we have several matrices that act upon the system

$$
\begin{pmatrix} E_{+1} \\ E_{-1} \end{pmatrix} = \boldsymbol{D}_1^{-1} \boldsymbol{D}_2 \boldsymbol{P}_2 \boldsymbol{D}_2^{-1} \boldsymbol{D}_3 \begin{pmatrix} E_{+3} \\ E_{-3} \end{pmatrix}
\tag{B.26}
$$

We can treat this to be of the form

$$
\begin{pmatrix} E_{+1} \\ E_{-1} \end{pmatrix} = \boldsymbol{M} \begin{pmatrix} E_{+3} \\ E_{-3} \end{pmatrix}
\tag{B.27}
$$

with $\mathbf{M}$ is given by

$$
\boldsymbol{M} = \begin{pmatrix} M_{11} & M_{12} \\ M_{21} & M_{22} \end{pmatrix} = \boldsymbol{D}_1^{-1} \boldsymbol{D}_2 \boldsymbol{P}_2 \boldsymbol{D}_2^{-1} \boldsymbol{D}_3
\tag{B.28}
$$

This matrix is the effective transmission matrix and in corollary to Eq. (B.24) we can get the reflectivity and transmissivity by

$$
\begin{aligned}
r &= \frac{M_{21}}{M_{11}} \\
t &= \frac{1}{M_{11}}
\end{aligned}
\tag{B.29}
$$

At this point, it is not too hard to see extension to N number of layers is given by

$$\begin{pmatrix} E_{+1} \\ E_{-1} \end{pmatrix} = \boldsymbol{M} \begin{pmatrix} E_{+N} \\ E_{-N} \end{pmatrix} \tag{B.30}$$

where $\boldsymbol{M}$ is given by

$$\boldsymbol{M} = \begin{pmatrix} M_{11} & M_{12} \\ M_{23} & M_{22} \end{pmatrix} = \boldsymbol{D}_1^{-1} \left(\prod_{i=2}^{N-1} \boldsymbol{D}_i \boldsymbol{P}_i \boldsymbol{D}_i^{-1} \right) \boldsymbol{D}_N \tag{B.31}$$

in this case, we have that reflectivity and transmissivity are going to be given by

$$\begin{aligned} r &= \left. \frac{E_{-1}}{E_{+1}} \right|_{E_{-N}=0} = \frac{M_{21}}{M_{11}} \\ t &= \left. \frac{E_{+N}}{E_{+1}} \right|_{E_{-N}=0} = \frac{1}{M_{11}} \end{aligned} \tag{B.32}$$

The transmittance and reflectance are then given by

$$R = |r|^2 \tag{B.33}$$

$$T = \frac{n_N \cos \theta_N}{n_1 \cos \theta_1} |t|^2 \tag{B.34}$$

While this method lends itself to easy computation and implementation, it does not calculate the field amplitudes inside of each of the layers. In order to do so, we must consider the full treatment of all the amplitudes and boundary conditions and solve for each individually. This is done in the follow section.

Field formalism to get amplitudes in all layers

To be able to solve for the field amplitudes in all the layers, we must use the boundary conditions at each interface, and solve for the individual amplitudes in all layers. This approach is very similar to the approach taken in the mode formalism for higher interfaces, with different linear algebra techniques to solve for the amplitudes instead of the resonance condition. Again, we start with the one-interface system to start the trend, and start with Eq. (B.2) changed slightly:

$$|\boldsymbol{E}_{-1}|\cos\theta_1 + |\boldsymbol{E}_{+2}|\cos\theta_2 = |\boldsymbol{E}_{+1}|\cos\theta_1$$
$$-n_1|\boldsymbol{E}_{-1}| + n_2|\boldsymbol{E}_{+2}| = n_1|\boldsymbol{E}_{+1}|$$

(B.35)

written in matrix form

$$\begin{pmatrix} \cos\theta_1 & \cos\theta_2 \\ -n_1 & n_2 \end{pmatrix} \begin{pmatrix} E_{-1} \\ E_{+2} \end{pmatrix} = \begin{pmatrix} \cos\theta_1 \\ n_1 \end{pmatrix} E_{+1}$$

(B.36)

We can solve this system of equations to get the reflected E_{-1} and transmitted E_{-2} amplitude in terms on the input amplitude E_{+1}. This is done with the standard formalism of solving a system of equations using an augmented matrix and reduced row echelon form (rref) [131]. The augmented matrix is given adding the solution vector as a column to the matrix in Eq.(B.36).

$$\begin{pmatrix} -\cos\theta_1 & -\cos\theta_2 & -\cos\theta_1 \\ n_1 & -n_2 & -n_1 \end{pmatrix}$$

(B.37)

Using any form of technique to get the augmented matrix in rref results in

$$\begin{pmatrix} 1 & 0 & \frac{n_1 \cos\theta_2 - n_2 \cos\theta_1}{n_1 \cos\theta_2 + n_2 \cos\theta_1} \\ 0 & 1 & \frac{2n_1 \cos\theta_2}{n_1 \cos\theta_2 + n_2 \cos\theta_1} \end{pmatrix} \tag{B.38}$$

Returning it to the full equation we get

$$\begin{pmatrix} 1 & 0 \\ 0 & 1 \end{pmatrix} \begin{pmatrix} E_{-1} \\ E_{+2} \end{pmatrix} = \begin{pmatrix} \frac{n_1 \cos\theta_2 - n_2 \cos\theta_1}{n_1 \cos\theta_2 + n_2 \cos\theta_1} \\ \frac{2n_1 \cos\theta_2}{n_1 \cos\theta_2 + n_2 \cos\theta_1} \end{pmatrix} E_{+1} \tag{B.39}$$

showing us that

$$E_{-1} = \frac{n_1 \cos\theta_2 - n_2 \cos\theta_1}{n_1 \cos\theta_2 + n_2 \cos\theta_1} E_{+1} = r_{12} E_{+1}$$
$$E_{+2} = \frac{2n_1 \cos\theta_2}{n_1 \cos\theta_2 + n_2 \cos\theta_1} E_{+1} = t_{12} E_{+1} \tag{B.40}$$

confirming the validity of this approach.

Increasing to two interfaces, we now have four boundary conditions.

$$|\boldsymbol{E}_{-1}| \cos\theta_1 + |\boldsymbol{E}_{+2}| \cos\theta_2 - |\boldsymbol{E}_{-2}| \cos\theta_2 = |\boldsymbol{E}_{+1}| \cos\theta_1$$

$$-n_1|\boldsymbol{E}_{-1}| + n_2|\boldsymbol{E}_{+2}| + n_2|\boldsymbol{E}_{-2}| = n_1|\boldsymbol{E}_{+1}|$$

$$|\boldsymbol{E}_{+2}|e^{\Phi_{2,2}} \cos\theta_2 - |\boldsymbol{E}_{-2}|e^{-\Phi_{2,2}} \cos\theta_2 - |\boldsymbol{E}_{+3}|e^{\Phi_{3,2}} \cos\theta_3 = 0 \tag{B.41}$$

$$n_2|\boldsymbol{E}_{+2}|e^{\Phi_{2,2}} + n_2|\boldsymbol{E}_{-2}|e^{-\Phi_{2,2}} - n_3|\boldsymbol{E}_{+3}|e^{\Phi_{3,2}} = 0$$

where

$$\Phi_{a,b} = ik_{xa}d_b = i\frac{2\pi n_a \cos\theta_a}{\lambda} d_b \tag{B.42}$$

with d_b being the distance from zero. Here $d_2 = t_2$, later this becomes more important as the number of interfaces increases. Written in matrix form this becomes

$$
\begin{pmatrix}
\cos\theta_1 & \cos\theta_2 & -\cos\theta_2 & 0 \\
-n_1 & n_2 & n_2 & 0 \\
0 & e^{\Phi_{2,2}}\cos\theta_2 & -e^{-\Phi_{2,2}}\cos\theta_2 & -e^{\Phi_{3,2}}\cos\theta_3 \\
0 & n_2 e^{\Phi_{2,2}} & n_2 e^{-\Phi_{2,2}} & -n_3 e^{\Phi_{3,2}}
\end{pmatrix}
\begin{pmatrix}
E_{-1} \\
E_{+2} \\
E_{-2} \\
E_{+3}
\end{pmatrix}
=
\begin{pmatrix}
\cos\theta_1 \\
n_1 \\
0 \\
0
\end{pmatrix}
E_{+1}
$$
(B.43)

The matrix on the left hand side of Eq. (B.43), builds upon the matrix in Eq. (B.36). The upper left 2x2 sub-matrix is Eq. (B.36), and the entirety of the matrix can be considered by the additional two rows and columns. Each new column represents a new field in the system: one propagating in the new final layer and one counter-propagating in the previously final layer. The new rows represent the two boundary equations at the new interface and involve the previously transmitted field and the two new fields of the system. Since E_{+1} does not occur in the boundary conditions for the interface at t_2, the solution vector on the right side of Eq. (B.36) is extended by two rows of zeros. This technique of adding the new rows and columns for each interface can be continued for as many interfaces as needed. We would now be able to use the augmented matrix to calculate all the field amplitudes in terms of the input field.

117

As a final example, here is the matrix for three interfaces:

$$
\begin{pmatrix}
\cos\theta_1 & \cos\theta_2 & -\cos\theta_2 & 0 & 0 & 0 \\
-n_1 & n_2 & n_2 & 0 & 0 & 0 \\
0 & e^{\Phi_{2,2}}\cos\theta_2 & -e^{-\Phi_{2,2}}\cos\theta_2 & -e^{\Phi_{3,2}}\cos\theta_3 & e^{-\Phi_{3,2}}\cos\theta_3 & 0 \\
0 & n_2 e^{\Phi_{2,2}} & n_2 e^{-\Phi_{2,2}} & -n_3 e^{\Phi_{3,2}} & -n_3 e^{-\Phi_{3,2}} & 0 \\
0 & 0 & 0 & e^{\Phi_{3,3}}\cos\theta_3 & -e^{-\Phi_{3,3}}\cos\theta_3 & -e^{\Phi_{4,3}}\cos\theta_4 \\
0 & 0 & 0 & n_3 e^{\Phi_{3,3}} & n_3 e^{-\Phi_{3,3}} & -n_4 e^{\Phi_{4,3}}
\end{pmatrix}
$$

$$\text{(B.44)}$$

in this case it is important to note that in Eq. (B.42), $d_3 = t_2 + t_3$ is the distance to the last interface, which is the sum of the two thicknesses.

In Appendix B, code is included that creates the required matrix and calculates the electric and magnetic fields, as well as the energy density, for all regions of space.

APPENDIX C

MATHEMATICA PACKAGE

This appendix contains the Mathematica package used for this dissertation. The Mathematica version at the time of this dissertation was 10. First is the introduction text with the version information and how to use the mathematica package. The first section of code contains miscellaneous useful constants and functions, as well as a few functions used throughout the package. The next section covers the dispersion of the modes and is capable of calculating and plotting the mode dispersions for an arbitrary number of interfaces, relevant to Appendix A.

Also in this section is code for plotting the electric and magnetic fields of the eigen solutions. The next section calculates the reflectivity and transmissivity for an arbitrary number of interfaces, relevant to Appendix B. We use the recursive formulism to show its implementation, and for many plotting functions of the TM reflectivity it is only called once. Additionally, there is code for plotting the the electric and magnetic fields, and the energy density for an input field.

```mathematica
BeginPackage["HerbGFunctionsv5`",{"ErrorBarPlots`"}]
(*
Created by Herbert Grotewohl, hgrotewo@uoregon.edu or hgrotewohl@gmail.com for questions.
created 08/2013
v2      08/2014
v3      never "published"
v4      never "published"
v5      in progress

To "install" put .m file in "C:\ProgramData\Mathematica\Applications\     (Windows 7 and 10)
This is a hidden folder, you will need to reveal hidden files.
    There are otherways to do it, this is just the way I do it, but it is easy enough!
    Main thing is that there are many different folders which mathematica can look for, including adding your
 own file path.

To access use command Needs["HerbGFunctionsv5`"] at beginning of file. I suggest making it an initialization
cell.

Mode functions are for unitless k, ω and t.   ω=ω/ωp,k=k/kp,t=t/λp
    This makes the values for each on the order of 1, instead of very awkward values.

For mode dispersion plots and arrays, the permittivities must have dielectrics entered as a function of
frequency.
Ex:
εone[ω_]:=1
ModePlot[Agωp,{εone,AgDrude},{},.1,.7,1000,.1,Frame->True]                Using drude model silver from
permittivies.m

All versions of course have had changes to comments and new comments reflecting the changes made during each
version.

v2
Added functions for plotting modes without error bars, by appending Line to function
Reflectivity & transmitivity
    -made functions recursive
    -removed derivatives and phase stitching
v3
Changes mode equations to be error regions for default usage.  Previous error bar plots are now referenced
with an EB at the end.
More comments.
Added PhaseStich and AD (array derivative)

v4
modes made to be for any layer system and added field of modes

v5
defined temp equation to not calculate mode equation for every data point, much faster run time!
added plotting functions for rp, Rp and Rphasep, so that recursive not done everytime, quicker calculations!
added plotting functions for the r/t fields, such that matrices not created everytime, faster creation of plot
fixed a sign error in p reflectivity that shifted phase by π.
```

Constants and misc equations

```
c:=2.998*10^8  (* m/s *)
ωλ[x_]:= 2*π*c/(x*10^-9)
Fano[ω_,ω0_,F_,γ_]:=( F γ + ω -ω0)^2/((ω-ω0)^2 +γ^2)


PhaseStitch[array_]:=(
(* can not be done with Table[], since need last point to have been adjusted already *)
tarray=Table[0,{i,Length[array]-1}];
(*  This Table will run through the array stiching it, lose last data point for ease of making *)
Do[
If[i==1,tarray[[1]]=array[[1]],
(* First spot is same as array *)
tarray[[i]]=If[Abs[array[[i+1]]-array[[i]]]<π,
(* Check to see if jump is greater than π *)
tarray[[i-1]]+array[[i+1]]-array[[i]],
(* If < π, add difference to previous point *)
tarray[[i-1]]+array[[i+1]]-array[[i]]+If[array[[i+1]]-array[[i]]<0,2π,-2π]]
(* If > π, add either 2π or -2π, depending on if slope is positive or negative *)
],
{i,Length[array]-1}];
tarray
)


AD[array_,{xmin_,xmax_}]:=(
(* xmin and xmax of independant variable (x in y[x]) needed to know how large each step is for derivative *)
step=(xmax-xmin)/Length[array];
(* here the step difference for the array is calculated *)
Table[(array[[i+1]]-array[[i]])/step,{i,Length[array]-1}]
(* basic (y[x]-y[x-step])/step numerical derivative of an array of points *)
)


ksp[ε1_,ε2_,ω_]:=ω Sqrt[(ε1 ε2)/(ε1+ε2)]
```

Mode Dispersion with imaginary ω as error zone

Mode functions require unitless input for k, ω and t.

$\omega=\omega/\omega$p, k =k/kp, t=t/λp

both dispersions in ω vs k

and E/M fields for given k/ω

```
ke[e_,k_,w_]:=Sqrt[k^2-e*(w)^2]
xi[e_,k_,w_]:=e/ke[e,k,w]
```

⌄ Matrix of boundary conditions- create then row reduce numerically
adding a layer to the system adds the same boundary conditions everytime,
thus same diagonal/offdiagonal elements, with index updated.
thickness array is converted to a distance array for each interface, starting at
d=0
An initial matrix for one interface is created
For loop creates a new layer step by step as defined by the following seven
steps:
1. Matrix is first transposed, as mathematica does not have easy way to add
columns
2. First column added introduces additional field to previous final boundary
3. 2nd column added is for new field in new layer at the existing boundaries (all
zeroes)
4. Transpose matrix back into normal form
5. First row for one BC at new interface
6. 2nd row for 2nd BC at new interface
7. Redefine the matrix, to be used in next step of loop
new function makes all numbers then determinent, numbers is for faster
calculation.

Plots

Line

```
ModePlotLine[△p_,εarray_,tarray_,krmin_,krmax_,Length_,△guess_,option___]:=(
If[Length[εarray]-2!=Length[tarray],
Text["ERROR, ERROR. ERROR!!!!! Arrays incompatible, please check manual"],
step=(krmax-krmin)/Length;
ωarray=Table[0,{i,krmin,krmax,step}];
karray=Table[k,{k,krmin,krmax,step}];
localmodeeq[k_,ω_]=modeeq[k,ω,Table[εarray[[s]][Re[ω+△p]],{s,Length[εarray]}],tarray];
Do[
ωarray[[j]]=ω/.FindRoot[localmodeeq[karray[[j]],ω]==0,{ω,If[j==1,△guess,ωarray[[j-1]]]}],
{j,Length+1}];
ebωarray=Table[{karray[[i]],Re[ωarray[[i]]]},{i,Length+1}];
ListPlot[ebωarray,option,Joined->True]]
)

ModePlotLineDown[△p_,εarray_,tarray_,krmin_,krmax_,Length_,△guess_,option___]:=(
If[Length[εarray]-2!=Length[tarray],
Text["ERROR, ERROR. ERROR!!!!! Arrays incompatible, please check manual"],
step=(krmax-krmin)/Length;
ωarray=Table[0,{i,krmin,krmax,step}];
karray=Table[k,{k,krmin,krmax,step}];
localmodeeq[k_,ω_]=modeeq[k,ω,Table[εarray[[s]][Re[ω+△p]],{s,Length[εarray]}],tarray];
Do[
ωarray[[j]]=ω/.FindRoot[localmodeeq[karray[[Length+2-j]],ω]==0,{ω,If[j==1,△guess,ωarray[[j-1]]]}],
{j,Length+1}];
ωarray=Reverse[ωarray];
ebωarray=Table[{karray[[i]],Re[ωarray[[i]]]},
{i,Length+1}];
ListPlot[ebωarray,option,Joined->True]]
)
```

Error Bar

```
ModePlotEB[△p_,εarray_,tarray_,krmin_,krmax_,Length_,△guess_,option___]:=(
If[Length[εarray]-2!=Length[tarray],
Text["ERROR, ERROR. ERROR!!!!! Arrays incompatible, please check manual"],
step=(krmax-krmin)/Length;
ωarray=Table[0,{i,krmin,krmax,step}];
karray=Table[k,{k,krmin,krmax,step}];
localmodeeq[k_,ω_]=modeeq[k,ω,Table[εarray[[s]][Re[ω+△p]],{s,Length[εarray]}],tarray];
Do[
ωarray[[j]]=ω/.FindRoot[localmodeeq[karray[[j]],ω]==0,{ω,If[j==1,△guess,ωarray[[j-1]]]}],
{j,Length+1}];
ebωarray=Table[{{karray[[i]],Re[ωarray[[i]]]},ErrorBar[2*Abs[Im[ωarray[[i]]]]]},{i,Length+1}];
ErrorListPlot[ebωarray,option]]
)
```

```
ModePlotEBDown[Δp_,εarray_,tarray_,krmin_,krmax_,Length_,Δguess_,option___]:=(
If[Length[εarray]-2!=Length[tarray],
Text["ERROR, ERROR. ERROR!!!!! Arrays incompatible, please check manual"],
step=(krmax-krmin)/Length;
ωarray=Table[0,{i,krmin,krmax,step}];
karray=Table[k,{k,krmin,krmax,step}];
localmodeeq[k_,ω_]=modeeq[k,ω,Table[εarray[[s]][Re[ω+Δp]],{s,Length[εarray]}],tarray];
Do[
ωarray[[j]]=ω/.FindRoot[localmodeeq[karray[[Length+2-j]],ω]==0,{ω,If[j==1,Δguess,ωarray[[j-1]]]}],
{j,Length+1}];
ωarray=Reverse[ωarray];
ebωarray=Table[{{karray[[i]],Re[ωarray[[i]]]},ErrorBar[2*Abs[Im[ωarray[[i]]]]]},{i,Length+1}];
ErrorListPlot[ebωarray,option]]
)
```

Zone

```
ModePlot[Δp_,εarray_,tarray_,krmin_,krmax_,Length_,Δguess_,color_,option___]:=(
If[Length[εarray]-2!=Length[tarray],
Text["ERROR, ERROR. ERROR!!!!! Arrays incompatible, please check manual"],
step=(krmax-krmin)/Length;
ωarray=Table[0,{i,krmin,krmax,step}];
karray=Table[k,{k,krmin,krmax,step}];
localmodeeq[k_,ω_]=modeeq[k,ω,Table[εarray[[s]][Re[ω+Δp]],{s,Length[εarray]}],tarray];
Do[
ωarray[[j]]=ω/.FindRoot[localmodeeq[karray[[j]],ω]==0,{ω,If[j==1,Δguess,ωarray[[j-1]]]}],
{j,Length+1}];
arrayRe=Table[{karray[[i]],Re[ωarray[[i]]]},{i,Length+1}];
arrayU=Table[{karray[[i]],Re[ωarray[[i]]]+2*Abs[Im[ωarray[[i]]]]},{i,Length+1}];
arrayD=Table[{karray[[i]],Re[ωarray[[i]]]-2*Abs[Im[ωarray[[i]]]]},{i,Length+1}];
ListPlot[{arrayRe,arrayU,arrayD},Filling->{2->{3}},Joined->{True,True,True},
PlotStyle->{{Thick,color},Opacity[0],Opacity[0]},FillingStyle->Directive[Opacity[.2],color],option]
)
ModePlotDown[Δp_,εarray_,tarray_,krmin_,krmax_,Length_,Δguess_,color_,option___]:=(
If[Length[εarray]-2!=Length[tarray],
Text["ERROR, ERROR. ERROR!!!!! Arrays incompatible, please check manual"],
step=(krmax-krmin)/Length;
ωarray=Table[0,{i,krmin,krmax,step}];
karray=Table[k,{k,krmin,krmax,step}];
localmodeeq[k_,ω_]=modeeq[k,ω,Table[εarray[[s]][Re[ω+Δp]],{s,Length[εarray]}],tarray];
Do[
ωarray[[j]]=ω/.FindRoot[localmodeeq[karray[[Length+2-j]],ω]==0,{ω,If[j==1,Δguess,ωarray[[j-1]]]}],
{j,Length+1}];
ωarray=Reverse[ωarray];
arrayRe=Table[{karray[[i]],Re[ωarray[[i]]]},{i,Length+1}];
arrayU=Table[{karray[[i]],Re[ωarray[[i]]]+2*Abs[Im[ωarray[[i]]]]},{i,Length+1}];
arrayD=Table[{karray[[i]],Re[ωarray[[i]]]-2*Abs[Im[ωarray[[i]]]]},{i,Length+1}];
ListPlot[{arrayRe,arrayU,arrayD},Filling->{2->{3}},Joined->{True,True,True},
PlotStyle->{{Thick,color},Opacity[0],Opacity[0]},FillingStyle->Directive[Opacity[.2],color],option]
)
```

Mode Field Plots

```
augmodematrix[k_,ω_,εarray_,tarray_]:=(
temp=Drop[modematrix[k,ω,εarray,tarray],-1,0];  (* Remove first row- overdetermined system otherwise *)
temp1=-Drop[temp,0,-(2*Length[tarray]+1)];
(* Take the first column, negative because moved to other side of eq *)
temp2=Drop[temp,0,1];
(* Take all columns except last column *)
Transpose[Append[Transpose[temp2],Transpose[temp1][[1]]]]
(* Add first column to the end of the other columns, everything in terms of magnitude at first interface
(that will always be 1) *)
)
rrefaugmodematrix[k_,ω_,εarray_,tarray_]:=RowReduce[N[augmodematrix[k,ω,εarray,tarray]]]
```

E Field

```
Efieldmode[kk_,ω_,earray_,tarray_,{x_,z_}]:=(
If[Length[earray]-2!=Length[tarray],
Text["ERROR, ERROR. ERROR!!!!! Arrays incompatible, please check manual"],
d2array=Table[Sum[tarray[[i]],{i,j}],{j,0,Length[tarray]}];
mtemp=rrefaugmodematrix[kk,ω,earray,tarray];
Piecewise[
Table[{If[j==1,{1,-I kk/kε[earray[[1]],kk,ω]}Exp[2π(I kk z + kε[earray[[1]],kk,ω]x)],
(* First Layer will be only decaying in negative direction *)
If[j==Length[earray],mtemp[[2j-3,Length[mtemp[[1]]]]]{1,I kk/kε[earray[[j]],kk,ω]}
Exp[2π(I kk z - kε[earray[[j]],kk,ω]x)],  (* Last Layer will be only decaying in positive direction *)
(mtemp[[2j-2,Length[mtemp[[1]]]]]{1,-I kk/kε[earray[[j]],kk,ω]}
Exp[2π(I kk z + kε[earray[[j]],kk,ω]x)]+  (*decaying in negative direction*)
mtemp[[2j-3,Length[mtemp[[1]]]]]{1,I kk/kε[earray[[j]],kk,ω]}
Exp[2π(I kk z - kε[earray[[j]],kk,ω]x)]  )(*decaying in positive direction*)
]], (* middle layers that contain both terms*)
If[j==1,x<0, (* first layer is always x<0 *)
If[j!=Length[earray],d2array[[j-1]]<x<d2array[[j]],
d2array[[j-1]]<x]]
(* d2array has one less element than earray, thus j-1 as table is going through length of earray *)
},
{j,Length[earray]}]]])

EfieldmodeStreamPlot[kk_,ω_,earray_,tarray_,{xmin_,xmax_},{zmin_,zmax_},options___]:=(
If[Length[earray]-2!=Length[tarray],
Text["ERROR, ERROR. ERROR!!!!! Arrays incompatible, please check manual"],
etemp[x_,z_]=Efieldmode[kk,ω,earray,tarray,{x,z}]; (* values stuck in for fast computation *)
StreamPlot[Re[etemp[x,z]],{z,zmin,zmax},{x,xmin,xmax},options]])

EfieldmodeVectorPlot[kk_,ω_,earray_,tarray_,{xmin_,xmax_},{zmin_,zmax_},options___]:=(
If[Length[earray]-2!=Length[tarray],
Text["ERROR, ERROR. ERROR!!!!! Arrays incompatible, please check manual"],
etemp[x_,z_]=Efieldmode[kk,ω,earray,tarray,{x,z}]; (* values stuck in for fast computation *)
VectorPlot[Re[etemp[x,z]],{z,zmin,zmax},{x,xmin,xmax},options]])
```

⌃ H field

```
Hfieldmode[kk_,ω_,earray_,tarray_,{x_,z_}]:=(
If[Length[earray]-2!=Length[tarray],
Text["ERROR, ERROR. ERROR!!!!! Arrays incompatible, please check manual"],
d2array=Table[Sum[tarray[[i]],{i,j}],{j,0,Length[tarray]}];
mtemp=rrefaugmodematrix[kk,ω,earray,tarray];
Piecewise[
Table[{If[j==1,ω I earray[[1]]/kϵ[earray[[1]],kk,ω]Exp[2π(I kk z + kϵ[earray[[1]],kk,ω]x)],
(* First Layer will be only decaying in negative direction *)
If[j==Length[earray],mtemp[[2j-3,Length[mtemp[[1]]]]]ω(-I earray[[j]]/kϵ[earray[[j]],kk,ω])
Exp[2π(I kk z - kϵ[Last[earray],kk,ω]x)],  (* Last Layer will be only decaying in positive direction *)
mtemp[[2j-2,Length[mtemp[[1]]]]]ω I earray[[j]]/kϵ[earray[[j]],kk,ω]
Exp[2π(I kk z + kϵ[earray[[j]],kk,ω]x)]+  (*decaying in negative direction*)
mtemp[[2j-3,Length[mtemp[[1]]]]]ω(-I earray[[j]]/kϵ[earray[[j]],kk,ω])
Exp[2π(I kk z - kϵ[earray[[j]],kk,ω]x)]  (*decaying in positive direction*)
]], (* middle layers that contain both terms*)
If[j==1,x<0, (* first layer is always x<0 *)
If[j!=Length[earray],d2array[[j-1]]<x<d2array[[j]],
d2array[[j-1]]<x]] (* d2array has one less element than earray, thus j-1 as table is going through length
},
{j,Length[earray]}]
]]
)


HfieldmodeDensityPlot[kk_,ω_,earray_,tarray_,{xmin_,xmax_},{zmin_,zmax_},options___]:=(
If[Length[earray]-2!=Length[tarray],
htemp[x_,z_]=Hfieldmode[kk,ω,earray,tarray,{x,z}]  (* values stuck in for fast computation *)
DensityPlot[Re[htemp[x,z]],{z,zmin,zmax},{x,xmin,xmax},options]]
)
```

Reflectance and Reflectivity and associated with those.
angles should be in degrees, thickness in nm

⌃ Needed functions

```
θl[θ1_,ε1_,εlayer_]:=ArcSin[(Sqrt[ε1/εlayer])*Sin[θ1]];
ωλmeters[λ_]:= 2*π*c/(λ);
kz[θ1_,λ_,ε1_,ε2_]:=(ωλmeters[λ]/c)*Sqrt[(ε2-ε1*(Sin[θ1])^2)];
```

Reflection

Fresnel Coefficients-
Assumes input dielectric for calculating a n/mith layer- non-accessible functions, only used in package

```
rnm[ϵi_,ϵi_,ϵn_,ϵm_]:=-(Sqrt[ϵm]Cos[θl[ϵi,ϵi,ϵn]]-Sqrt[ϵn]Cos[θl[ϵi,ϵi,ϵm]])/
(Sqrt[ϵm]Cos[θl[ϵi,ϵi,ϵn]]+Sqrt[ϵn]Cos[θl[ϵi,ϵi,ϵm]])

srnm[ϵi_,ϵi_,ϵn_,ϵm_]:=(Sqrt[ϵn]Cos[θl[ϵi,ϵi,ϵn]]-Sqrt[ϵm]Cos[θl[ϵi,ϵi,ϵm]])/
(Sqrt[ϵn]Cos[θl[ϵi,ϵi,ϵn]]+Sqrt[ϵm]Cos[θl[ϵi,ϵi,ϵm]])
```

recursive reflectivity-
uses a "helper" function r to keep track of first layer permittivity.
checks to make sure ϵarray and tarray are compatible for use.
For function see Yeh pg 89, and think of multilayer as collapsing furthest end to a single interface with an effective r and t

```
rP[ϵi_,λ_,earray_,tarray_]:=(
If[Length[earray]-2!=Length[tarray],
Text["ERROR, ERROR. ERROR!!!!! Arrays incompatible, please check manual"],
recP[ϵi,λ,earray[[1]],earray,tarray]]
)
recP[ϵi_,λ_,ei_,earray_,tarray_]:=(
If[Length[earray]==2,rnm[ϵi,ei,earray[[1]],earray[[2]]],
(rnm[ϵi,ei,earray[[1]],earray[[2]]]+recP[ϵi,λ,ei,Drop[earray,1],Drop[tarray,1]]*
Exp[I*2*kz[ϵi,λ,ei,earray[[2]]]*tarray[[1]]])/(1+rnm[ϵi,ei,earray[[1]],earray[[2]]]*
recP[ϵi,λ,ei,Drop[earray,1],Drop[tarray,1]]*Exp[I*2*kz[ϵi,λ,ei,earray[[2]]]*tarray[[1]]])]
)

rS[ϵi_,λ_,earray_,tarray_]:=(
If[Length[earray]-2!=Length[tarray],
Text["ERROR, ERROR. ERROR!!!!! Arrays incompatible, please check manual"],
recS[ϵi,λ,earray[[1]],earray,tarray]]
)
recS[ϵi_,λ_,ei_,earray_,tarray_]:=(
If[Length[earray]==2,srnm[ϵi,ei,earray[[1]],earray[[2]]],
(srnm[ϵi,ei,earray[[1]],earray[[2]]]+recS[ϵi,λ,ei,Drop[earray,1],Drop[tarray,1]]*
Exp[I*2*kz[ϵi,λ,ei,earray[[2]]]*tarray[[1]]])/(1+srnm[ϵi,ei,earray[[1]],earray[[2]]]*
recS[ϵi,λ,ei,Drop[earray,1],Drop[tarray,1]]*Exp[I*2*kz[ϵi,λ,ei,earray[[2]]]*tarray[[1]]])]
)
```

used functions- in degrees and nm

```mathematica
ReflectivityP[ϑi_,λ_,earray_,tarray_]:=rP[ϑi*π/180,λ*10^-9,earray,tarray*10^-9]
ReflectanceP[ϑi_,λ_,earray_,tarray_]:=ReflectivityP[ϑi,λ,earray,tarray]*
Conjugate[ReflectivityP[ϑi,λ,earray,tarray]]
RPhaseP[ϑi_,λ_,earray_,tarray_]:=Arg[ReflectivityP[ϑi,λ,earray,tarray]]

ReflectivityS[ϑi_,λ_,earray_,tarray_]:=rS[ϑi*π/180,λ*10^-9,earray,tarray*10^-9]
ReflectanceS[ϑi_,λ_,earray_,tarray_]:=ReflectivityS[ϑi,λ,earray,tarray]*
Conjugate[ReflectivityS[ϑi,λ,earray,tarray]]
RPhaseS[ϑi_,λ_,earray_,tarray_]:=Arg[ReflectivityS[ϑi,λ,earray,tarray]]

plotrep[{ϑmin_,ϑmax_},λ_,earray_,tarray_,options___]:=(
tempr[ϑ_]=Re[ReflectivityP[ϑ,λ,earray,tarray]];
Plot[tempr[ϑ],{ϑ,ϑmin,ϑmax},Axes->False,Frame->True,options]
)
plotimp[{ϑmin_,ϑmax_},λ_,earray_,tarray_,options___]:=(
tempr[ϑ_]=Im[ReflectivityP[ϑ,λ,earray,tarray]];
Plot[tempr[ϑ],{ϑ,ϑmin,ϑmax},Axes->False,Frame->True,options]
)


plotpararp[{ϑmin_,ϑmax_},λ_,earray_,tarray_,options___]:=(
tempr[ϑ_]=ReflectivityP[ϑ,λ,earray,tarray];
ParametricPlot[{Re[tempr[ϑ]],Im[tempr[ϑ]]},{ϑ,ϑmin,ϑmax},Frame->True,options]
)

plotpararpee[ϑ_,λ_,earray_,tarray_,{emin_,emax_},options___]:=(
tempr[e_]=ReflectivityP[ϑ,λ,Append[Delete[earray,-1],e],tarray];
ParametricPlot[{Re[tempr[e]],Im[tempr[e]]},{e,emin,emax},Frame->True,options]
)

plotpararpn[ϑ_,λ_,earray_,tarray_,{nmin_,nmax_},options___]:=(
tempr[n_]=ReflectivityP[ϑ,λ,Append[Delete[earray,-1],n^2],tarray];
ParametricPlot[{Re[tempr[n]],Im[tempr[n]]},{n,nmin,nmax},Frame->True,options]
)

plotRp[{ϑmin_,ϑmax_},λ_,earray_,tarray_,options___]:=(
tempr[ϑ_]=ReflectanceP[ϑ,λ,earray,tarray];
Plot[tempr[ϑ],{ϑ,ϑmin,ϑmax},Axes->False,Frame->True,options]
)

plotRpee[ϑ_,λ_,earray_,tarray_,{emin_,emax_},options___]:=(
tempr[e_]=ReflectanceP[ϑ,λ,Append[Delete[earray,-1],e],tarray];
Plot[tempr[e],{e,emin,emax},Axes->False,Frame->True,options]
)

plotRpn[ϑ_,λ_,earray_,tarray_,{nmin_,nmax_},options___]:=(
tempr[e_]=ReflectanceP[ϑ,λ,Append[Delete[earray,-1],e^2],tarray];
Plot[tempr[e],{e,nmin,nmax},Axes->False,Frame->True,options]
)
```

```
plotphasep[{emin_,emax_},λ_,earray_,tarray_,{length_,scale_,shift_},options___]:=(
temppp[e_]=RPhaseP[e,λ,earray,tarray];
step=(emax-emin)/length;
earray=Table[e,{e,emin,emax,step}];
temparr=Table[temppp[earray[[i]]],{i,length}];
temparr2=scale*PhaseStitch[temparr]+shift;
ListPlot[temparr2,DataRange->{emin,emax},Axes->False,Frame->True,options]
)

plotphasepee[e_,λ_,earray_,tarray_,{emin_,emax_},{length_,scale_,shift_},options___]:=(
temppp[e_]=RPhaseP[e,λ,Append[Delete[earray,-1],e],tarray];
step=(emax-emin)/length;
e2array=Table[e,{e,emin,emax,step}];
temparr=Table[temppp[e2array[[i]]],{i,length}];
temparr2=scale*PhaseStitch[temparr]+shift;
ListPlot[temparr2,DataRange->{emin,emax},Axes->False,Frame->True,options]
)

plotphasepn[e_,λ_,earray_,tarray_,{nmin_,nmax_},{length_,scale_,shift_},options___]:=(
temppp[n_]=RPhaseP[e,λ,Append[Delete[earray,-1],n^2],tarray];
step=(nmax-nmin)/length;
e2array=Table[e,{e,nmin,nmax,step}];
temparr=Table[temppp[e2array[[i]]],{i,length}];
temparr2=scale*PhaseStitch[temparr]+shift;
ListPlot[temparr2,DataRange->{nmin,nmax},Axes->False,Frame->True,options]
)
```

Transmission

Fresnel Coefficients

```
tnm[e1_,e1_,en_,em_]:=(2Sqrt[en]Cos[el[e1,e1,en]])/
(Sqrt[em]Cos[el[e1,e1,en]]+Sqrt[en]Cos[el[e1,e1,em]])

stnm[e1_,e1_,en_,em_]:=(2Sqrt[en]Cos[el[e1,e1,en]])/
(Sqrt[en]Cos[el[e1,e1,en]]+Sqrt[em]Cos[el[e1,e1,em]])
```

recursive transmitivity-

uses a "helper" function r to keep track of first layer permittivity.

checks to make sure ℰarray and tarray are compatible for use.

For function see Yeh pg 90, and think of multilayer as collapsing furthest end to a single interface with an effective r and t

```
tP[ℰi_,λ_,earray_,tarray_]:=(
If[Length[earray]-2!=Length[tarray],
Text["ERROR, ERROR. ERROR!!!!! Arrays incompatible, please check manual"],
rectP[ℰi,λ,earray[[1]],earray,tarray]]
)
rectP[ℰi_,λ_,ei_,earray_,tarray_]:=(
If[Length[earray]==2,tnm[ℰi,ei,earray[[1]],earray[[2]]],
(tnm[ℰi,ei,earray[[1]],earray[[2]]]*rectP[ℰi,λ,ei,Drop[earray,1],Drop[tarray,1]]*
Exp[I*kz[ℰi,λ,ei,earray[[2]]]*tarray[[1]]])/(1+rnm[ℰi,ei,earray[[1]],earray[[2]]]*
recP[ℰi,λ,ei,Drop[earray,1],Drop[tarray,1]]*Exp[I*2*kz[ℰi,λ,ei,earray[[2]]]*tarray[[1]]]))
)

tS[ℰi_,λ_,earray_,tarray_]:=(
If[Length[earray]-2!=Length[tarray],
Text["ERROR, ERROR. ERROR!!!!! Arrays incompatible, please check manual"],
rectS[ℰi,λ,earray[[1]],earray,tarray]]
)
rectS[ℰi_,λ_,ei_,earray_,tarray_]:=(
If[Length[earray]==2,stnm[ℰi,ei,earray[[1]],earray[[2]]],
(stnm[ℰi,ei,earray[[1]],earray[[2]]]*rectS[ℰi,λ,ei,Drop[earray,1],Drop[tarray,1]]*
Exp[I*kz[ℰi,λ,ei,earray[[2]]]*tarray[[1]]])/(1+srnm[ℰi,ei,earray[[1]],earray[[2]]]*
recS[ℰi,λ,ei,Drop[earray,1],Drop[tarray,1]]*Exp[I*2*kz[ℰi,λ,ei,earray[[2]]]*tarray[[1]]]))
)
```

Used functions- in degrees and nanometers.

```
TransmitivityP[ℰi_,λ_,earray_,tarray_]:=tP[ℰi*π/180,λ*10^-9,earray,tarray*10^-9]
TransmittanceP[ℰi_,λ_,earray_,tarray_]:=TransmitivityP[ℰi,λ,earray,tarray]*Conjugate[TransmitivityP[ℰi,⌐
TPhaseP[ℰi_,λ_,earray_,tarray_]:=Arg[TransmitivityP[ℰi,λ,earray,tarray]]

TransmitivityS[ℰi_,λ_,earray_,tarray_]:=tS[ℰi*π/180,λ*10^-9,earray,tarray*10^-9]
TransmittanceS[ℰi_,λ_,earray_,tarray_]:=TransmitivityS[ℰi,λ,earray,tarray]*Conjugate[TransmitivityS[ℰi,⌐
TPhaseS[ℰi_,λ_,earray_,tarray_]:=Arg[TransmitivityS[ℰi,λ,earray,tarray]]
```

130

R/T Field and Energy Density Plots- Builds up to whatever layer system needed- TM only

▲ used functions

```
earray2[λ_,earray_]:=Table[earray[[i]][ωλ[λ]],{i,Length[earray]}]; (* used for energy densities *)
Costhn[th_,e1_,en_]:=1/Sqrt[en] Sqrt[en-e1 Sin[th]^2] (* cosine of the angle in the nth dielectric *)
Sinthn[th_,e1_,en_]:=Sqrt[(e1/en)]Sin[th] (* sine of the angle in the nth dielectric *)
```

⌄ Matrix of boundary conditions- create then row reduce numerically
adding a layer to the system adds the same boundary conditions everytime,
thus same diagonal/offdiagonal elements, with index updated.
thickness array is converted to a distance array for each interface, starting at
d=0
An initial matrix for one interface is created
For loop creates a new layer step by step as defined by the following seven
steps:
1. Matrix is first transposed, as mathematica does not have easy way to add
columns
2. First column added introduces backwards propagating field to previous final
boundary
3. 2nd column added is for new forward propagating field in new layer at the
existing boundary (all zeroes)
4. Transpose matrix back into normal form
5. First row for one BC at new interface
6. 2nd row for 2nd BC at new interface
7. Redefine the matrix, to be used in next step of loop
Add column of input field for rref solutions

new function makes all numbers then rref, numbers is for faster calculation.

131

```
allmatrix[θ_,λ_,εarray_,tarray_]:=(
darray=Table[Sum[tarray[[i]],{i,j}],{j,0,Length[tarray]}];
(* array to change thicknesses to distances from origin *)
matrix={{-Cos[θ],-Costhn[θ,εarray[[1]],εarray[[2]]]},{Sqrt[εarray[[1]]],-Sqrt[εarray[[2]]]}};
(* starting matrix for 1 interface *)
For[i=1,i<=Length[tarray],i++,
(* Counts up to number of boundaries to create a 2*(= of interfaces) square matrix*)
matrix=Append[Append[    (*5,6,7*)
    Transpose[   (*4*)
        Append[Append[ (*2,3*)
            Transpose[matrix], (*1*)
        Join[Table[0,{2*(i-1)}], {Costhn[θ,εarray[[1]],εarray[[i+1]]]*Exp[-I Sqrt[εarray[[i+1]]]
(2*π)/λ Costhn[θ,εarray[[1]],εarray[[i+1]]]*darray[[i]]],-Sqrt[εarray[[i+1]]]*
Exp[-I Sqrt[εarray[[i+1]]]  (2*π)/λ Costhn[θ,εarray[[1]],εarray[[i+1]]]*darray[[i]]]}],(*2*)
        Table[0,{2*i}]] (*3*)
    ], (*4*)
    Join[Table[0,{2*i-1}],{Costhn[θ,εarray[[1]],εarray[[i+1]]]*Exp[I Sqrt[εarray[[i+1]]]
(2*π)/λ Costhn[θ,εarray[[1]],εarray[[i+1]]]*darray[[i-1]]],-Costhn[θ,εarray[[1]],εarray[[i+1]]]*
Exp[-I Sqrt[εarray[[i+1]]]  (2*π)/λ
Costhn[θ,εarray[[1]],εarray[[i+1]]]*darray[[i+1]]],-Costhn[θ,εarray[[1]],εarray[[i+2]]]*
Exp[I Sqrt[εarray[[i+2]]]  (2*π)/λ Costhn[θ,εarray[[1]],εarray[[i+2]]]*darray[[i+1]]]}],(*5*)
    Join[Table[0,{2*i-1}],{Sqrt[εarray[[i+1]]]*Exp[I Sqrt[εarray[[i+1]]]
(2*π)/λ Costhn[θ,εarray[[1]],εarray[[i+1]]]*darray[[i+1]]],Sqrt[εarray[[i+1]]]*
Exp[-I Sqrt[εarray[[i+1]]]  (2*π)/λ
Costhn[θ,εarray[[1]],εarray[[i+1]]]*darray[[i+1]]],-Sqrt[εarray[[i+2]]]*
Exp[I Sqrt[εarray[[i+2]]]  (2*π)/λ Costhn[θ,εarray[[1]],εarray[[i+2]]]*darray[[i+1]]]}]] (*6*)
];
Transpose[Append[Transpose[matrix],Join[{-Cos[θ],-Sqrt[εarray[[1]]]},Table[0,{2*Length[tarray]}]]]]]
(* add last column of normalized magnitude of input (forward) Efield*)
)


nummatrix[θ_,λ_,εarray_,tarray_]:=RowReduce[N[allmatrix[θ,λ,εarray,tarray]]]   (*make matrix full of numb
```

⌃ Efield

thickness to distance array is created, as the function calls the matrix, must have a different name

Piecewise function is created using Table with two elements, {field,location}

```
Efieldtemp[θ_,λ_,earray_,tarray_,{x_,z_}]:=(
d2array=Table[Sum[tarray[[i]],{i,j}],{j,0,Length[tarray]}];
nummatrixtemp=nummatrix[θ,λ,earray,tarray];
Piecewise[
Table[{If[k==1,0,nummatrixtemp[[2*(k-1),2*Length[earray]-1]]]
{Sinthn[θ,earray[[1]],earray[[k]]],-Costhn[θ,earray[[1]],earray[[k]]]}
Exp[I Sqrt[earray[[k]]] (2*π)/λ
(x Costhn[θ,earray[[1]],earray[[k]]]+z Sinthn[θ,earray[[1]],earray[[k]]])]]+
(* forward propagating fields, If[] is used to negate incident field in first layer*)
If[k==Length[earray],0,nummatrixtemp[[2*k-1,2*Length[earray]-1]]]
{Sinthn[θ,earray[[1]],earray[[k]]],Costhn[θ,earray[[1]],earray[[k]]]}
Exp[I Sqrt[earray[[k]]] (2*π)/λ (- x Costhn[θ,earray[[1]],earray[[k]]]+
z Sinthn[θ,earray[[1]],earray[[k]]])]]},
(* backward propagating field, If[] is used as there is no reflected field in final layer*)
If[k==1,x<0, (* first layer is always x<0 *)
If[k!=Length[earray],d2array[[k-1]]<x<d2array[[k]],
d2array[[k-1]]<x]]
(* d2array has one less element than earray, thus k-1 as table is going through length of earray *)
},
{k,Length[earray]}]])


Efield[θ_,λ_,earray_,tarray_,{x_,z_}]:=(
If[Length[earray]-2!=Length[tarray],
Text["ERROR, ERROR. ERROR!!!!! Arrays incompatible, please check manual"],
Efieldtemp[θ*π/180,λ,earray,tarray,{x,z}]]
)


EfieldStreamPlot[θ_,λ_,earray_,tarray_,{xmin_,xmax_},{zmin_,zmax_},options___]:=(
If[Length[earray]-2!=Length[tarray],
Text["ERROR, ERROR. ERROR!!!!! Arrays incompatible, please check manual"],
eftemp[x_,z_]=Efieldtemp[θ*π/180,λ,earray,tarray,{x,z}];
StreamPlot[Re[eftemp[x,z]],{z,zmin,zmax},{x,xmin,xmax},options]]
)


EfieldVectorPlot[θ_,λ_,earray_,tarray_,{xmin_,xmax_},{zmin_,zmax_},options___]:=(
If[Length[earray]-2!=Length[tarray],
Text["ERROR, ERROR. ERROR!!!!! Arrays incompatible, please check manual"],
eftemp[x_,z_]=Efieldtemp[θ*π/180,λ,earray,tarray,{x,z}];
VectorPlot[Re[eftemp[x,z]],{z,zmin,zmax},{x,xmin,xmax},options]]
)
```

⌃ Hfield

Curl of a 3D E array is used to find H, then the single array element of H is the output piecewise function

For curl 3D array is required, as well as the derivative variables to not be the same as the values to be input into the function

derivatives are taken using XYZ then values are input into equation using /.X->x/.Z->z

```
Hfieldtemp[θ_,λ_,earray_,tarray_,{x_,z_}]:=(
d2array=Table[Sum[tarray[[i]],{i,j}],{j,0,Length[tarray]}];
nummatrixtemp=nummatrix[θ,λ,earray,tarray];
Piecewise[
Table[{(I λ)/(2*π) (Curl[If[k==1,0,nummatrixtemp[[2*(k-1),2*Length[earray]-1]]
{Sinthn[θ,earray[[1]],earray[[k]]],0,-Costhn[θ,earray[[1]],earray[[k]]]}
Exp[I Sqrt[earray[[k]]] (2*π)/λ
(X Costhn[θ,earray[[1]],earray[[k]]]+Z Sinthn[θ,earray[[1]],earray[[k]]])]]+
(* forward propagating fields, If is used to negate incident field in first layer*)
If[k==Length[earray],0,nummatrixtemp[[2*k-1,2*Length[earray]-1]]]
{Sinthn[θ,earray[[1]],earray[[k]]],0,Costhn[θ,earray[[1]],earray[[k]]]}
Exp[I Sqrt[earray[[k]]] (2*π)/λ (- X Costhn[θ,earray[[1]],earray[[k]]]+
Z Sinthn[θ,earray[[1]],earray[[k]]])]]],{X,Y,Z}]/.X->x/.Z->z)[[2]],
(* backward propagating field, If is used as there is no reflected field in final layer*)
If[k==1,x<0,
If[k!=Length[earray],d2array[[k-1]]<x<d2array[[k]],
d2array[[k-1]]<x]]
},
{k,Length[earray]}]
]
)

Hfield[θ_,λ_,earray_,tarray_,{x_,z_}]:=(
If[Length[earray]-2!=Length[tarray],
Text["ERROR, ERROR. ERROR!!!!! Arrays incompatible, please check manual"],
Hfieldtemp[θ*π/180,λ,earray,tarray,{x,z}]]
)

HfieldDensityPlot[θ_,λ_,earray_,tarray_,{xmin_,xmax_},{zmin_,zmax_},options___]:=(
If[Length[earray]-2!=Length[tarray],
Text["ERROR, ERROR. ERROR!!!!! Arrays incompatible, please check manual"],
hftemp[x_,z_]=Hfieldtemp[θ*π/180,λ,earray,tarray,{x,z}];
DensityPlot[Re[hftemp[x,z]],{z,zmin,zmax},{x,xmin,xmax},options]]
)
```

⌃ Energy Density

Uses the Efield and Hfield functions to get energy density

```
EnergyD[ε_,λ_,earray_,tarray_,{x_,z_}]:=(
d2array=Table[Sum[tarray[[i]],{i,j}],{j,0,Length[tarray]}];
dselect=Piecewise[Table[{earray[[k]],If[k==1,x<0,
If[k!=Length[earray],d2array[[k-1]]<x<d2array[[k]],d2array[[k-1]]<x]]},{k,Length[earray]}]];
If[Length[earray]-2!=Length[tarray],
Text["ERROR, ERROR. ERROR!!!!! Arrays incompatible, please check manual"],
.5((Re[D[w dselect[w],w]/.w->ωλ[λ]])
Conjugate[Efield[ε,λ,earray2[λ,earray],tarray,{x,z}]].Efield[ε,λ,earray2[λ,earray],tarray,{x,z}]+
Hfield[ε,λ,earray2[λ,earray],tarray,{x,z}]*.Hfield[ε,λ,earray2[λ,earray],tarray,{x,z}])]
)

EnergyDPlot[ε_,λ_,earray_,tarray_,{xmin_,xmax_},options___]:=(
d2array=Table[Sum[tarray[[i]],{i,j}],{j,0,Length[tarray]}];
dselect=Piecewise[Table[{earray[[k]],If[k==1,x<0,
If[k!=Length[earray],d2array[[k-1]]<x<d2array[[k]],d2array[[k-1]]<x]]},{k,Length[earray]}]];
If[Length[earray]-2!=Length[tarray],
Text["ERROR, ERROR. ERROR!!!!! Arrays incompatible, please check manual"],
edtemp[x_,z_]=.5((Re[D[w dselect[w],w]/.w->ωλ[λ]])
Conjugate[Efield[ε,λ,earray2[λ,earray],tarray,{x,z}]].Efield[ε,λ,earray2[λ,earray],tarray,{x,z}]+
Hfield[ε,λ,earray2[λ,earray],tarray,{x,z}]*.Hfield[ε,λ,earray2[λ,earray],tarray,{x,z}]);
Plot[Re[edtemp[x,0]],{x,xmin,xmax},options]]
)

EnergyDDensityPlot[ε_,λ_,earray_,tarray_,{xmin_,xmax_},{zmin_,zmax_},options___]:=(
d2array=Table[Sum[tarray[[i]],{i,j}],{j,0,Length[tarray]}];
dselect=Piecewise[Table[{earray[[k]],If[k==1,x<0,
If[k!=Length[earray],d2array[[k-1]]<x<d2array[[k]],d2array[[k-1]]<x]]},{k,Length[earray]}]];
If[Length[earray]-2!=Length[tarray],
Text["ERROR, ERROR. ERROR!!!!! Arrays incompatible, please check manual"],
edtemp[x_,z_]=.5((Re[D[w dselect[w],w]/.w->ωλ[λ]])
Conjugate[Efield[ε,λ,earray2[λ,earray],tarray,{x,z}]].Efield[ε,λ,earray2[λ,earray],tarray,{x,z}]+
Hfield[ε,λ,earray2[λ,earray],tarray,{x,z}]*.Hfield[ε,λ,earray2[λ,earray],tarray,{x,z}]);
DensityPlot[Re[edtemp[x,z]],{z,zmin,zmax},{x,xmin,xmax},options]]
)
```

```
EnergyDE[𝜀_,λ_,earray_,tarray_,{x_,z_}]:=(
d2array=Table[Sum[tarray[[i]],{i,j}],{j,0,Length[tarray]}];
dselect=Piecewise[Table[{earray[[k]],If[k==1,x<0,
If[k!=Length[earray],d2array[[k-1]]<x<d2array[[k]],d2array[[k-1]]<x]]},{k,Length[earray]}]];
If[Length[earray]-2!=Length[tarray],
Text["ERROR, ERROR. ERROR!!!!! Arrays incompatible, please check manual"],
.5((Re[D[w dselect[w],w]/.w->ωλ[λ]])
Conjugate[Efield[𝜀,λ,earray2[λ,earray],tarray,{x,z}]].Efield[𝜀,λ,earray2[λ,earray],tarray,{x,z}])]
)

EnergyDH[𝜀_,λ_,earray_,tarray_,{x_,z_}]:=(
If[Length[earray]-2!=Length[tarray],
Text["ERROR, ERROR. ERROR!!!!! Arrays incompatible, please check manual"],
.5(Hfield[𝜀,λ,earray2[λ,earray],tarray,{x,z}]*.Hfield[𝜀,λ,earray2[λ,earray],tarray,{x,z}])]
)
```

End

```
End[]

EndPackage[]
```

REFERENCES CITED

[1] S. A. Maier, *Plasmonics: fundamentals and applications* (Springer, New York, 2007), ISBN 978-0-387-37825-1.

[2] M. Faraday, Philosophical Transactions of the Royal Society of London **147**, 145 (1857), URL
http://rstl.royalsocietypublishing.org/content/147/145.short.

[3] A. Sommerfeld, Weid. Annalen **67**, 233 (1899).

[4] J. Zenneck, Ann. Phys. **23**, 846 (1907).

[5] G. Mie, Ann. Phys. **25**, 377 (1908).

[6] U. Fano, Journal of the Optical Society of America **31**, 213 (1941), URL
http://www.osapublishing.org/abstract.cfm?URI=josa-31-3-213.

[7] G. Moore, Electronics **38** (1965).

[8] W. L. Barnes, A. Dereux, and T. W. Ebbesen, Nature **424**, 824 (2003), ISSN 0028-0836, URL http://www.nature.com/doifinder/10.1038/nature01937.

[9] S. I. Bozhevolnyi, V. S. Volkov, E. Devaux, J.-Y. Laluet, and T. W. Ebbesen, Nature **440**, 508 (2006), ISSN 0028-0836, URL
http://www.nature.com/doifinder/10.1038/nature04594.

[10] V. Coello, T. Søndergaard, and S. I. Bozhevolnyi, Optics Communications **240**, 345 (2004), ISSN 00304018.

[11] H. Ditlbacher, J. R. Krenn, G. Schider, A. Leitner, and F. R. Aussenegg, Applied Physics Letters **81**, 1762 (2002), ISSN 00036951, URL
http://scitation.aip.org/content/aip/journal/apl/81/10/10.1063/1.1506018.

[12] J. R. Krenn, H. Ditlbacher, G. Schider, A. Hohenau, A. Leitner, and F. R. Aussenegg, Journal of Microscopy **209**, 167 (2003), ISSN 00222720, URL
http://doi.wiley.com/10.1046/j.1365-2818.2003.01088.x.

[13] T. Nikolajsen, K. Leosson, and
S. I. Bozhevolnyi, Applied Physics Letters **85**, 5833 (2004), ISSN 00036951, URL
http://scitation.aip.org/content/aip/journal/apl/85/24/10.1063/1.1835997.

[14] S. I. Bozhevolnyi and F. A. Pudonin, Physical Review Letters **78**, 2823 (1997), ISSN 0031-9007, URL
http://link.aps.org/doi/10.1103/PhysRevLett.78.2823.

[15] J. B. Pendry, Physical Review Letters **85**, 3966 (2000), ISSN 0031-9007, URL
http://link.aps.org/doi/10.1103/PhysRevLett.85.3966.

[16] A. Grbic and G. V. Eleftheriades, Physical Review Letters **92**, 117403 (2004),
ISSN 0031-9007, URL
http://link.aps.org/doi/10.1103/PhysRevLett.92.117403.

[17] R. A. Shelby, D. R. Smith, S. Schultz, V. G. Veselago, J. B. Pendry, D. R.
Smith, W. J. Padilla, D. C. Vier, S. C. Nemat-Nasser, S. Schultz, et al., Science
(New York, N.Y.) **292**, 77 (2001), ISSN 0036-8075, URL
http://www.ncbi.nlm.nih.gov/pubmed/11292865.

[18] T. J. Yen, W. J. Padilla, N. Fang, D. C. Vier, D. R. Smith, J. B. Pendry, D. N.
Basov, and X. Zhang, Science (New York, N.Y.) **303**, 1494 (2004), ISSN
1095-9203, URL http://www.ncbi.nlm.nih.gov/pubmed/15001772.

[19] J. Homola, S. S. Yee, and G. Gauglitz, Sensors and Actuators B: Chemical **54**, 3
(1999), ISSN 09254005, URL
http://www.sciencedirect.com/science/article/pii/S0925400598003219.

[20] R. Karlsson, A. Michaelsson, and L. Mattsson, Journal of Immunological
Methods **145**, 229 (1991), ISSN 00221759, URL
http://linkinghub.elsevier.com/retrieve/pii/0022175991903319.

[21] S. Löfås, B. Johnsson, B. Liedberg, C. Nylander, I. Lundström, D. C. Cullen,
R. G. W. Brown, C. R. Lowe, P. B. Daniels, J. K. Deacon, et al., J. Chem.
Soc., Chem. Commun. **4**, 1526 (1990), ISSN 0022-4936, URL
http://xlink.rsc.org/?DOI=C39900001526.

[22] R. Karlsson and R. Stahlberg, Analytical Biochemistry **228**, 274 (1995), ISSN
00032697, URL
http://linkinghub.elsevier.com/retrieve/pii/S0003269785713504.

[23] A. V. Kabashin, S. Patskovsky, and A. N. Grigorenko, Optics Express **17**, 21191
(2009), ISSN 1094-4087, URL
http://www.opticsexpress.org/abstract.cfm?URI=oe-17-23-21191.

[24] C. Nylander, B. Liedberg, and T. Lind, Sensors and Actuators **3**, 79 (1982),
ISSN 02506874, URL
http://www.sciencedirect.com/science/article/pii/0250687482800085.

[25] B. Liedberg, C. Nylander, and I. Lunström, Sensors and Actuators **4**, 299
(1983), URL
http://www.sciencedirect.com/science/article/pii/0250687483850367.

[26] G. Martínez-López, D. Luna-Moreno, D. Monzón-Hernández, and R. Valdivia-Hernández, Optics and Lasers in Engineering **49**, 675 (2011), ISSN 01438166, URL http://www.sciencedirect.com/science/article/pii/S0143816610002903.

[27] L. J. Davis and M. Deutsch, The Review of scientific instruments **81**, 114905 (2010), ISSN 1089-7623, URL http://www.ncbi.nlm.nih.gov/pubmed/21133494.

[28] A. Szabo, L. Stolz, and R. Granzow, Current Opinion in Structural Biology **5**, 699 (1995), ISSN 0959440X, URL http://www.sciencedirect.com/science/article/pii/0959440X95800646.

[29] J. Homola, *Surface plasmon resonance sensors for detection of chemical and biological species* (2008), URL http://dx.doi.org/10.1021/cr068107d.

[30] A. J. Haes and R. P. Van Duyne, Analytical and Bioanalytical Chemistry **379**, 920 (2004), ISSN 1618-2642, URL http://link.springer.com/10.1007/s00216-004-2708-9.

[31] A. J. Haes and R. P. Van Duyne, Journal of the American Chemical Society **124**, 10596 (2002), ISSN 0002-7863, URL http://pubs.acs.org/doi/abs/10.1021/ja020393x.

[32] N. Nath and A. Chilkoti, Analytical Chemistry **76**, 5370 (2004), ISSN 0003-2700, URL http://pubs.acs.org/doi/abs/10.1021/ac049741z.

[33] N. Nath and A. Chilkoti, Analytical Chemistry **74**, 504 (2002), ISSN 0003-2700, URL http://pubs.acs.org/doi/abs/10.1021/ac015657x.

[34] E. Fontana, IEEE Transactions on Microwave Theory and Techniques **50**, 82 (2002), ISSN 00189480, URL http://ieeexplore.ieee.org/lpdocs/epic03/wrapper.htm?arnumber=981251.

[35] J. B. Jackson, S. L. Westcott, L. R. Hirsch, J. L. West, and N. J. Halas, Applied Physics Letters **82**, 257 (2003), ISSN 00036951, URL http://scitation.aip.org/content/aip/journal/apl/82/2/10.1063/1.1534916.

[36] L. Hirsch, R. J. Stafford, J. A. Bankson, S. R. Sershen, B. Rivera, R. E. Price, J. D. Hazle, N. J. Halas, and J. L. West, Proceedings of the National Academy of Sciences **100**, 13549 (2003), ISSN 0027-8424.

[37] C. Loo, A. Lin, L. Hirsch, M.-H. Lee, J. Barton, N. Halas, J. West, and R. Drezek, Technology in Cancer Research & Treatment **3**, 33 (2004), ISSN 1533-0346, URL http://tct.sagepub.com/lookup/doi/10.1177/153303460400300104.

[38] S. R. Sershen, S. L. Westcott, N. J. Halas, and J. L. West, Journal of Biomedical Materials Research **51**, 293 (2000), ISSN 00219304, URL http://doi.wiley.com/10.1002/1097-4636%2820000905%2951%3A3%3C293%3A%3AAID-JBM1%

[39] S. Pillai, K. R. Catchpole, T. Trupke, and M. A. Green, Journal of Applied Physics **101**, 093105 (2007), ISSN 00218979, URL http://scitation.aip.org/content/aip/journal/jap/101/9/10.1063/1.2734885.

[40] X. Luo and T. Ishihara, Applied Physics Letters **84**, 4780 (2004), ISSN 00036951, URL http://scitation.aip.org/content/aip/journal/apl/84/23/10.1063/1.1760221.

[41] E. Altewischer, M. P. van Exter, and J. P. Woerdman, Nature **418**, 304 (2002), ISSN 0028-0836, URL http://www.nature.com/doifinder/10.1038/nature00869.

[42] D. J. Bergman and M. I. Stockman, Physical Review Letters **90**, 027402 (2003), ISSN 0031-9007, URL http://link.aps.org/doi/10.1103/PhysRevLett.90.027402.

[43] M. I. Rau and A. R. P, Physica Scripta **68**, C96 (2003), ISSN 1402-4896, URL http://stacks.iop.org/1402-4896/68/i=5/a=N01.

[44] U. Fano, Physical Review **124**, 1866 (1961), ISSN 0031-899X, URL http://link.aps.org/doi/10.1103/PhysRev.124.1866.

[45] U. Fano, Physical Review **124**, 1866 (1961), ISSN 0031-899X, URL http://link.aps.org/doi/10.1103/PhysRev.124.1866.

[46] U. Fano, Physical Review **72**, 26 (1947), ISSN 0031-899X, URL http://link.aps.org/doi/10.1103/PhysRev.72.26.

[47] U. Fano and W. Lichten, Physical Review Letters **14**, 627 (1965), ISSN 0031-9007, URL http://link.aps.org/doi/10.1103/PhysRevLett.14.627.

[48] K.-J. Boller, A. Imamoglu, and S. Harris, Physical Review Letters **66**, 2593 (1991), ISSN 0031-9007, URL http://link.aps.org/doi/10.1103/PhysRevLett.66.2593.

[49] J. Gea-Banacloche, Y.-q. Li, S.-z. Jin, and M. Xiao, Physical Review A **51**, 576 (1995), ISSN 1050-2947, URL http://link.aps.org/doi/10.1103/PhysRevA.51.576.

[50] M. Xiao, Y.-q. Li, S.-z. Jin, and J. Gea-Banacloche, Physical Review Letters **74**, 666 (1995), ISSN 0031-9007, URL http://link.aps.org/doi/10.1103/PhysRevLett.74.666.

[51] S. E. Harris, Physics Today **50**, 36 (1997), ISSN 00319228, URL
http://scitation.aip.org/content/aip/magazine/physicstoday/article/50/7/10.106

[52] J. P. Marangos, Journal of Modern Optics **45**, 471 (1998), ISSN 0950-0340, URL
http://www.tandfonline.com/doi/abs/10.1080/09500349808231909.

[53] D. E. Nikonov, A. Imamolu, and M. O. Scully, Physical Review B **59**, 12212
(1999), ISSN 0163-1829, URL
http://link.aps.org/doi/10.1103/PhysRevB.59.12212.

[54] J. Mompart, R. Corbalán, A. E, S. M. O. S, Z. M, A. S, K. O, S. M. O, M. P,
G. W, et al., Journal of
Optics B: Quantum and Semiclassical Optics **2**, R7 (2000), ISSN 1464-4266, URL
http://stacks.iop.org/1464-4266/2/i=3/a=201?key=crossref.a66b213bd80214b4e8752

[55] V. Arkhipkin and Y. Heller, Physics Letters A **98**, 12 (1983), ISSN 03759601,
URL http://linkinghub.elsevier.com/retrieve/pii/0375960183905339.

[56] K. Kobayashi, H. Aikawa, S. Katsumoto, and Y. Iye, Physical Review Letters
88, 256806 (2002), ISSN 0031-9007, URL
http://link.aps.org/doi/10.1103/PhysRevLett.88.256806.

[57] K. Kobayashi, H. Aikawa, A. Sano, S. Katsumoto, and Y. Iye, Physical Review
B **70**, 035319 (2004), ISSN 1098-0121, URL
http://link.aps.org/doi/10.1103/PhysRevB.70.035319.

[58] S. Fan, Applied Physics Letters **80**, 908 (2002), ISSN 00036951, URL
http://scitation.aip.org/content/aip/journal/apl/80/6/10.1063/1.1448174.

[59] D. Smith, H. Chang, K. Fuller, A. Rosenberger, and R. Boyd, Physical Review
A **69**, 063804 (2004), ISSN 1050-2947, URL
http://link.aps.org/doi/10.1103/PhysRevA.69.063804.

[60] Q. Xu, S. Sandhu, M. Povinelli, J. Shakya, S. Fan, and M. Lipson, Physical
Review Letters **96**, 123901 (2006), ISSN 0031-9007, URL
http://link.aps.org/doi/10.1103/PhysRevLett.96.123901.

[61] M. Tomita, K. Totsuka, R. Hanamura, and T. Matsumoto, Journal of the
Optical Society of America B **26**, 813 (2009), ISSN 0740-3224, URL
http://www.osapublishing.org/viewmedia.cfm?uri=josab-26-4-813&seq=0&html=true.

[62] L. Babić and M. J. A. de Dood, Optics express **18**, 26569 (2010), ISSN
1094-4087, URL
http://www.osapublishing.org/viewmedia.cfm?uri=oe-18-25-26569&seq=0&html=true.

[63] S. N. Sheikholeslami, A. García-Etxarri, and J. A. Dionne, Nano letters **11**, 3927
(2011), ISSN 1530-6992, URL http://dx.doi.org/10.1021/nl202143j.

[64] A. E. Miroshnichenko and Y. S. Kivshar, Nano letters **12**, 6459 (2012), ISSN 1530-6992, URL http://dx.doi.org/10.1021/nl303927q.

[65] C. E. Campanella, F. De Leonardis, L. Mastronardi, P. Malara, G. Gagliardi, and V. M. N. Passaro, Optics express **23**, 14301 (2015), ISSN 1094-4087, URL http://www.osapublishing.org/viewmedia.cfm?uri=oe-23-11-14301&seq=0&html=true.

[66] S. Klaiman, N. Moiseyev, and H. Sadeghpour, Physical Review B **75**, 113305 (2007), ISSN 1098-0121, URL http://link.aps.org/doi/10.1103/PhysRevB.75.113305.

[67] A. Lovera, B. Gallinet, P. Nordlander, and O. J. F. Martin, ACS nano **7**, 4527 (2013), ISSN 1936-086X, URL http://dx.doi.org/10.1021/nn401175j.

[68] J. B. Lassiter, H. Sobhani, J. A. Fan, J. Kundu, F. Capasso, P. Nordlander, and N. J. Halas, Nano Letters **10**, 3184 (2010), ISSN 15306984, URL http://dx.doi.org/10.1021/nl102108u.

[69] B. Luk'yanchuk, N. I. Zheludev, S. A. Maier, N. J. Halas, P. Nordlander, H. Giessen, and C. T. Chong, Nature materials **9**, 707 (2010), ISSN 1476-1122, URL http://dx.doi.org/10.1038/nmat2810.

[70] A. E. Miroshnichenko, S. Flach, and Y. S. Kivshar, Reviews of Modern Physics **82**, 2257 (2010), ISSN 0034-6861, URL http://link.aps.org/doi/10.1103/RevModPhys.82.2257.

[71] K. Lodewijks, J. Ryken, W. Van Roy, G. Borghs, L. Lagae, and P. Van Dorpe, Plasmonics **8**, 1379 (2013), ISSN 1557-1955, URL http://link.springer.com/10.1007/s11468-013-9549-3.

[72] H. Grotewohl and M. Deutsch, Journal of Optics **17**, 085003 (2015), ISSN 2040-8978, URL http://stacks.iop.org/2040-8986/17/i=8/a=085003.

[73] S. Balci, E. Karademir, and C. Kocabas, Optics letters **40**, 3177 (2015), ISSN 1539-4794, URL http://www.osapublishing.org/viewmedia.cfm?uri=ol-40-13-3177&seq=0&html=true.

[74] S. Zhang, D. A. Genov, Y. Wang, M. Liu, and X. Zhang, Physical Review Letters **101**, 047401 (2008), ISSN 0031-9007, URL http://link.aps.org/doi/10.1103/PhysRevLett.101.047401.

[75] J. Gu, R. Singh, X. Liu, X. Zhang, Y. Ma, S. Zhang, S. A. Maier, Z. Tian, A. K. Azad, H.-T. Chen, et al., Nature communications **3**, 1151 (2012), ISSN 2041-1723, URL http://dx.doi.org/10.1038/ncomms2153.

[76] S. Weis, R. Rivière, S. Deléglise, E. Gavartin, O. Arcizet, A. Schliesser, and T. J. Kippenberg, Science (New York, N.Y.) **330**, 1520 (2010), ISSN 1095-9203, URL http://www.sciencemag.org/content/330/6010/1520.abstract.

[77] C. Rohde, K. Hasegawa, and M. Deutsch, Optics Letters **32**, 415 (2007), ISSN 0146-9592, 0609162, URL
http://www.opticsinfobase.org/abstract.cfm?id=125544
http://arxiv.org/abs/physics/0609162
http://www.opticsinfobase.org/abstract.cfm?URI=ol-32-4-415.

[78] N. Liu, L. Langguth, T. Weiss, J. Kästel, M. Fleischhauer, T. Pfau, and H. Giessen, Nature materials **8**, 758 (2009), ISSN 1476-1122, URL http://dx.doi.org/10.1038/nmat2495.

[79] P. Ding, C. Fan, Y. Cheng, E. Liang, and Q. Xue, Applied optics **51**, 1879 (2012), ISSN 1539-4522, URL
http://ao.osa.org/abstract.cfm?URI=ao-51-12-1879.

[80] C. L. Garrido Alzar, M. a. G. Martinez, and P. Nussenzveig, American Journal of Physics **70**, 37 (2002), ISSN 00029505, URL
http://link.aip.org/link/AJPIAS/v70/i1/p37/s1&Agg=doi.

[81] A. G. Litvak and M. D. Tokman, Physical Review Letters **88**, 095003 (2002), ISSN 0031-9007, URL
http://link.aps.org/doi/10.1103/PhysRevLett.88.095003.

[82] Y. S. Joe, A. M. Satanin, C. S. Kim, F. U, B. G. E, Wigner, B. C. K. Adair R K, P. R. E, R. A. R. P. Fano U,
F. T. A. Cerdeira F, et al., Physica Scripta **74**, 259 (2006), ISSN 0031-8949, URL
http://stacks.iop.org/1402-4896/74/i=2/a=020?key=crossref.424d32217ba158e775f4:

[83] L. Novotny, American Journal of Physics **78**, 1199 (2010), ISSN 00029505, URL http://link.aip.org/link/?AJPIAS/78/1199/1.

[84] S. Satpathy, A. Roy, and A. Mohapatra, European Journal of Physics **33**, 863 (2012), ISSN 0143-0807, URL
http://stacks.iop.org/0143-0807/33/i=4/a=863.

[85] S. Orrigo, H. Lenske, F. Cappuzzello, A. Cunsolo, A. Foti, A. Lazzaro, C. Nociforo, and J. Winfield (2006).

[86] X. Cao and H. Lenske (2014), 1410.1375, URL
http://arxiv.org/abs/1410.1375.

[87] S. HEIN, W. KOCH, and L. NANNEN, Journal of Fluid Mechanics **664**, 238 (2010), ISSN 0022-1120, URL
http://www.journals.cambridge.org/abstract_S0022112010003757.

[88] J. P. Connerade, A. M. Lanes, and M. A. Baig, Journal of Physics B: Atomic and Molecular Physics **18**, 3507 (1985), ISSN 0022-3700, URL http://stacks.iop.org/0022-3700/18/i=17/a=013.

[89] J. P. Connerade and A. M. Lane, Reports on Progress in Physics **51**, 1439 (1988), ISSN 0034-4885, URL http://stacks.iop.org/0034-4885/51/i=11/a=002.

[90] B. Kim and K. Yoshihara, The Journal of Chemical Physics **99**, 1433 (1993), ISSN 00219606, URL http://scitation.aip.org/content/aip/journal/jcp/99/2/10.1063/1.465336.

[91] S. Herminghaus, M. Klopfleisch, and H. J. Schmidt, Optics letters **19**, 293 (1994), ISSN 0146-9592, URL http://www.opticsinfobase.org/ol/abstract.cfm?uri=ol-19-4-293.

[92] N. Rotenberg, D. M. Beggs, J. E. Sipe, and L. Kuipers, Optics express **21**, 16504 (2013), ISSN 1094-4087, URL http://www.opticsexpress.org/abstract.cfm?URI=oe-21-14-16504.

[93] S. Pillai, K. R. Catchpole, T. Trupke, and M. A. Green, Journal of Applied Physics **101**, 093105 (2007), ISSN 00218979, URL http://scitation.aip.org/content/aip/journal/jap/101/9/10.1063/1.2734885.

[94] R. Slavk, J. Homola, J. Čtyroký, and E. Brynda, Sensors and Actuators B: Chemical **74**, 106 (2001), ISSN 09254005, URL http://www.sciencedirect.com/science/article/pii/S0925400500007188.

[95] M. Zayats, A. B. Kharitonov, S. P. Pogorelova, O. Lioubashevski, E. Katz, and I. Willner, Journal of the American Chemical Society **125**, 16006 (2003), ISSN 0002-7863, URL http://dx.doi.org/10.1021/ja0379215.

[96] R. Kooyman, H. Kolkman, J. Van Gent, and J. Greve, Analytica Chimica Acta **213**, 35 (1988), ISSN 00032670, URL http://www.sciencedirect.com/science/article/pii/S0003267000813379.

[97] I. H. El-Sayed, X. Huang, and M. A. El-Sayed, Nano letters **5**, 829 (2005), ISSN 1530-6984, URL http://dx.doi.org/10.1021/nl050074e.

[98] N. W. Ashcroft and N. D. Mermin, *Solid State Physics* (Saunders College, 1976), ISBN 978-0030839931.

[99] E. Palik, *Handbook of Optical Constants of Solids* (Academic Press, 1985), ISBN 978-0-12-544415-6.

[100] P. Gadenne, F. Brouers, V. M. Shalaev, and A. K. Sarychev, Journal of the Optical Society of America B **15**, 68 (1998), ISSN 0740-3224, URL http://josab.osa.org/abstract.cfm?URI=josab-15-1-68.

[101] Y. Wu, C. Zhang, N. M. Estakhri, Y. Zhao, J. Kim, M. Zhang, X.-X. Liu, G. K. Pribil, A. Alù, C.-K. Shih, et al., Advanced materials (Deerfield Beach, Fla.) **26**, 6106 (2014), ISSN 1521-4095, URL http://www.ncbi.nlm.nih.gov/pubmed/24923858.

[102] B. J. Wiley, S. H. Im, Z.-Y. Li, J. McLellan, A. Siekkinen, and Y. Xia, The journal of physical chemistry. B **110**, 15666 (2006), ISSN 1520-6106, URL http://dx.doi.org/10.1021/jp0608628.

[103] S. Zeng, X. Yu, W.-C. Law, Y. Zhang, R. Hu, X.-Q. Dinh, H.-P. Ho, and K.-T. Yong, Sensors and Actuators B: Chemical **176**, 1128 (2013), ISSN 09254005, URL http://www.sciencedirect.com/science/article/pii/S0925400512009860.

[104] D. Sarid and W. Challener, *Modern Introduction to Surface Plasmons* (Cambridge, 2010), ISBN 9780521767170.

[105] J. Renger, R. Quidant, N. van Hulst, S. Palomba, and L. Novotny, Physical Review Letters **103** (2009), ISSN 0031-9007, URL http://prl.aps.org/abstract/PRL/v103/i26/e266802.

[106] N. Rotenberg, M. Betz, and H. van Driel, Physical Review Letters **105** (2010), ISSN 0031-9007, URL http://prl.aps.org/abstract/PRL/v105/i1/e017402 http://link.aps.org/doi/10.1103/PhysRevLett.105.017402.

[107] H. Raether, *Surface Plasmons on Smooth and Rough Surfaces and on Gratings* (Springer-Verlag, 1988), ISBN 978-3-540-47441-8.

[108] M. Born and E. Wolf, *Principles of Optics* (Cambridge, 1999), 7th ed., ISBN 0521642221.

[109] P. Yeh, *Optical Waves in Layered Media* (Wiley-Interscience, 1988), ISBN 0-471-82866-1.

[110] J. Dionne, L. Sweatlock, H. Atwater, and A. Polman, Physical Review B **72**, 075405 (2005), ISSN 1098-0121, URL http://link.aps.org/doi/10.1103/PhysRevB.72.075405.

[111] J. Dionne, L. Sweatlock, H. Atwater, and A. Polman, Physical Review B **73**, 035407 (2006), ISSN 1098-0121, URL http://link.aps.org/doi/10.1103/PhysRevB.73.035407.

[112] E. Economou, Physical Review **182**, 539 (1969), ISSN 0031-899X, URL
http://prola.aps.org/abstract/PR/v182/i2/p539_1
http://link.aps.org/doi/10.1103/PhysRev.182.539.

[113] G. J. Kovacs and G. D. Scott, Applied optics **17**, 3627 (1978), ISSN 0003-6935,
URL
http://www.opticsinfobase.org/viewmedia.cfm?uri=ao-17-22-3627&seq=0&html=true.

[114] K. Welford and J. Sambles, Journal of Modern Optics **35**, 1467 (1988), ISSN
0950-0340, URL http://dx.doi.org/10.1080/09500348814551611.

[115] J. R. DeVore, Journal of the Optical Society of America **41**, 416 (1951), ISSN
0030-3941, URL
http://www.opticsinfobase.org/abstract.cfm?URI=josa-41-6-416.

[116] H. Shin, M. F. Yanik, S. Fan, R. Zia, and M. L. Brongersma, Applied Physics
Letters **84**, 4421 (2004), ISSN 00036951, URL
http://link.aip.org/link/APPLAB/v84/i22/p4421/s1&Agg=doi.

[117] T. Y. Abi-Salloum, Physical Review A **81**, 053836 (2010), ISSN 1050-2947,
URL http://link.aps.org/doi/10.1103/PhysRevA.81.053836.

[118] J. Qi, Z. Chen, J. Chen, Y. Li, W. Qiang, J. Xu, and Q. Sun, Optics express
22, 14688 (2014), ISSN 1094-4087, URL
http://www.opticsinfobase.org/viewmedia.cfm?uri=oe-22-12-14688&seq=0&html=true.

[119] S. Hayashi, D. V. Nesterenko, and Z. Sekkat, Journal of Physics D: Applied
Physics **48**, 325303 (2015), ISSN 0022-3727, URL
http://iopscience.iop.org/article/10.1088/0022-3727/48/32/325303.

[120] T. Reynolds, M. R. Henderson, A. François, N. Riesen, J. M. M. Hall, S. V.
Afshar, S. J. Nicholls, and T. M. Monro, Optics express **23**, 17067 (2015), ISSN
1094-4087, URL
http://www.osapublishing.org/viewmedia.cfm?uri=oe-23-13-17067&seq=0&html=true.

[121] F.-C. Chien and S.-J. Chen, Biosensors & bioelectronics **20**, 633 (2004), ISSN
0956-5663, URL
http://www.sciencedirect.com/science/article/pii/S0956566304001411.

[122] L. Song, Z. Wang, D. Zhou, A. Nand, S. Li, B. Guo, Y. Wang, Z. Cheng,
W. Zhou, Z. Zheng,
et al., Sensors and Actuators B: Chemical **181**, 652 (2013), ISSN 09254005, URL
http://www.sciencedirect.com/science/article/pii/S0925400513001317.

[123] A. V. Kabashin and P. I. Nikitin, Quantum Electronics **27**, 653 (1997), ISSN
1063-7818, URL http://iopscience.iop.org/1063-7818/27/7/A23.

[124] A. Kabashin and P. Nikitin, Optics Communications **150**, 5 (1998), URL
http://www.sciencedirect.com/science/article/pii/S0030401897007268.

[125] K. Lodewijks, W. Van Roy, G. Borghs, L. Lagae, and P. Van Dorpe, Nano
letters **12**, 1655 (2012), ISSN 1530-6992, URL
http://dx.doi.org/10.1021/nl300044a.

[126] A. K. Sheridan, R. D. Harris, P. N. Bartlett, and J. S. Wilkinson, Sensors and
Actuators B: Chemical **97**, 114 (2004), ISSN 09254005, URL
http://www.sciencedirect.com/science/article/pii/S0925400503006890.

[127] C.-M. Wu and M.-C. Pao, Optics Express **12**, 3509 (2004), ISSN 1094-4087,
URL http://www.opticsexpress.org/abstract.cfm?URI=oe-12-15-3509.

[128] S. Y. Wu, H. P. Ho, W. C. Law, C. Lin, and S. K. Kong, Optics Letters **29**,
2378 (2004), ISSN 0146-9592, URL
http://www.osapublishing.org/viewmedia.cfm?uri=ol-29-20-2378&seq=0&html=true.

[129] S. Hayashi, D. V. Nesterenko, and Z. Sekkat, Applied Physics Express **8**,
022201 (2015), ISSN 1882-0778, URL
http://iopscience.iop.org/article/10.7567/APEX.8.022201.

[130] M. L. Boas, *Mathematical Methods in the Physical Sciences* (John Wiley and
Sons, 2006), 3rd ed.

[131] D. C. Lay, *Linear Algebra and its Applications* (Pearson, 2006), 3rd ed., ISBN
0-321-28713-4.